ORNL/TM-9786

ornl

OAK RIDGE NATIONAL LABORATORY

MARTIN MARIETTA

A Feasibility Study for the Spherical Torus Experiment

E. A. Lazarus

S. E. Attenberger
L. R. Baylor
S. K. Borowski
R. L. Brown
B. A. Carreras
L. A. Charlton
K. K. Chipley
G. R. Dalton
R. H. Fowler
W. R. Hamilton
T. C. Hender
R. E. Hill
S. P. Hirshman
J. T. Hogan
J. A. Holmes
W. A. Houlberg
S. S. Kalsi
V. D. Lee
P. S. Litherland
D. C. Lousteau
J. N. Luton
J. A. Mayhall
T. J. McManamy
G. H. Neilson
Y-K. M. Peng
J. A. Rome
M. J. Saltmarsh
J. Sheffield
D. J. Strickler
P. B. Thompson
C. C. Tsai
W. L. Wright

OPERATED BY
MARTIN MARIETTA ENERGY SYSTEMS, INC.
FOR THE UNITED STATES
DEPARTMENT OF ENERGY

Printed in the United States of America. Available from
National Technical Information Service
U.S. Department of Commerce
5285 Port Royal Road, Springfield, Virginia 22161
NTIS price codes—Printed Copy: A09 Microfiche: A01

ORNL/TM-9786
Dist. Category UC-20

Fusion Energy Division

A Feasibility Study for the Spherical Torus Experiment

1. E. A. Lazarus

2. S. E. Attenberger
3. L. R. Baylor
4. S. K. Borowski
5. R. L. Brown
6. B. A. Carreras
7. L. A. Charlton
8. K. K. Chipley
9. G. R. Dalton
10. R. H. Fowler
11. W. R. Hamilton
12. T. C. Hender
13. R. E. Hill
14. S. P. Hirshman
15. J. T. Hogan
16. J. A. Holmes
17. W. A. Houlberg
18. S. S. Kalsi
19. V. D. Lee
20. P. S. Litherland
21. D. C. Lousteau
22. J. N. Luton
23. J. A. Mayhall
24. T. J. McManamy
25. G. H. Neilson
26. Y-K. M. Peng
27. J. A. Rome
28. M. J. Saltmarsh
29. J. Sheffield
30. D. J. Strickler
31. P. B. Thompson
32. C. C. Tsai
33. W. L. Wright

Date Published–October 1985

Prepared by the
OAK RIDGE NATIONAL LABORATORY
Oak Ridge, Tennessee 37831
operated by
MARTIN MARIETTA ENERGY SYSTEMS, INC.
for the
U.S. DEPARTMENT OF ENERGY
under Contract No. DE-AC05-84OR21400

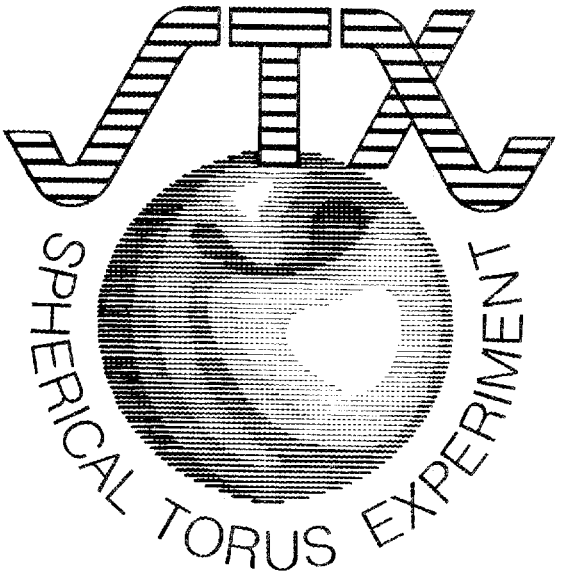
NSTX
SPHERICAL TORUS EXPERIMENT

CONTENTS

EXECUTIVE SUMMARY

INTRODUCTION

Oak Ridge National Laboratory (ORNL) proposes to build the Spherical Torus Experiment (STX), a very low aspect ratio toroidal confinement device. This proposal concentrates on tokamak operation of the experiment; however, it can in principle be operated as a pinch or reversed-field pinch as well. As a tokamak, the spherical torus confines a plasma that is characterized by high toroidal beta, low poloidal beta, large natural elongation, high plasma current for a given edge q, and strong paramagnetism. These features combine to offer the possibility of a compact, low-field fusion device. The figure below shows that when compared to a conventional tokamak the spherical torus represents a major change in geometry.

The primary goals of the experiment will be to demonstrate a capability for high beta (20%) in the first stability regime, to extend our knowledge of tokamak confinement scaling, and to test oscillating-field current drive. The experiment will operate in the high-beta, collisionless regime, which is achieved in STX at low temperatures because of the geometry.

ORNL-DWG 85-2498A3 FED

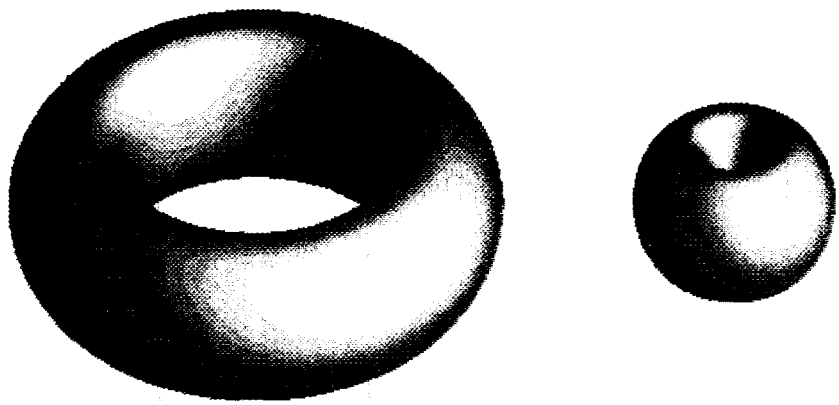

CONVENTIONAL TOKAMAK PLASMA

SPHERICAL TORUS PLASMA

At a minimum, operation of STX will help to resolve fundamental questions regarding the scaling of beta and confinement in tokamaks. Complete success in this program would have a significant impact on toroidal fusion research in that it would demonstrate solutions to the problems of beta and steady-state operation in the tokamak.

The proposed device has a major radius of 0.45 m, a toroidal field of 0.5 T, a plasma current of 900 kA, and heating by neutral beam injection. We estimate 30 months for design, construction, and assembly. The budget estimate, including contingency and escalation, is $6.8 million.

SPHERICAL TORUS CONCEPT

Over the past several years, stability at the beta values required to allow the tokamak to be an attractive reactor candidate has been established as an important issue in tokamak research. Along with the issue of stability is the associated problem of electron confinement. In the Princeton Beta Experiment (PBX), a tokamak experiment dedicated to the achievement of high beta, the approach is to access the second stability regime by bean shaping at large aspect ratio, which theoretically will provide ballooning stability, and to provide low-n stability by adding passive stabilization close to the plasma boundary.

The spherical torus has recently been proposed by Peng as an approach to toroidal fusion with the potential to overcome some weaknesses of the tokamak as a fusion reactor. The concept addresses the issues of beta, steady-state operation, and efficiency of field utilization. In the spherical torus, stability is achieved by virtue of very low aspect ratio where both high- and low-n stability are achieved in the first stability regime. Another distinction is that the spherical torus achieves high toroidal beta at much lower poloidal beta than the bean-shaped tokamak. Thus, the spherical torus is a complementary approach to the problem of stability at high beta.

So far, our MHD studies indicate that, at an edge $q \sim 3$, STX will be stable to high-n modes up to $\beta \approx 18\%$ and stable to low-n modes up to $\beta \approx 25\%$. The achievement of such high MHD stability limits at $q > 3$, particularly for low-n modes, is of importance because disruptivity increases as q is lowered. Thus, by operating STX away from the stability boundaries, we might hope to avoid the disruption limits to beta observed in many experiments.

An issue for all tokamaks is electron transport, which is anomalously large. To date, only empirical formulas exist to describe this transport. STX offers a unique capability to distinguish between the different proposed scaling laws.

The spherical torus lends itself very well to steady-state current maintenance by oscillating fields, because the toroidal flux is much lower than in a conventional tokamak. This approach to current drive is expected to be highly efficient since it is an inductive process. Another encouraging feature is that the amplitude and frequency of oscillation both decrease with increasing electron temperature. In future experiments nearer to reactor conditions, current drive by oscillating fields should become easier.

As a reactor, the spherical torus offers a substantial reduction in total coil weight relative to the conventional tokamak. Our analysis (Sect. 1.4) was made for reactors operating at the Troyon beta limit with neo-Alcator electron confinement. The fusion power and field strength at the toroidal coils were held constant.

STX PHYSICS PROGRAM

STX is a device that is truly rich in toroidal confinement physics. The major elements of the physics program will be:

1. High-beta stability. Initially STX will operate with 1.5 MW of neutral beam heating. Transport simulations using the most pessimistic electron confinement formula indicate

that the achievable volume-averaged beta will be 13% at this power level. While this is below the projected stability limits, we can investigate the limits by reducing the plasma current or by changing the plasma shape. In the future we will propose an upgrade to 2.3 MW of heating power, which will allow operation at beta values of about 20%. STX operates in a region of β, β_p space that is not accessible to the conventional tokamak; namely $\beta_p < A$, $<\beta> \sim \beta_p$. Studies will be undertaken in both limiter and divertor plasmas.

2. Electron confinement. Empirical scaling laws that differ by a factor of 2 in their projections for a conventional tokamak lead to projections that differ by more than an order of magnitude in STX. Thus, STX will provide a sensitive test of electron confinement scaling and should help to determine which scaling is correct.

3. Trapped particles. The trapped-particle fraction in STX is somewhat larger than in most tokamaks. Furthermore, because of its low aspect ratio and small major radius, STX will enter the collisionless regime at temperatures of only a few hundred electron volts. Thus, STX is expected to operate simultaneously at high beta and low ν_*. The neoclassical enhancement of plasma resistivity is calculated to be more than a factor of 2. STX should be able to test for any trapped-particle instabilities that may exist in high-beta, collisionless plasmas.

4. Ion confinement. STX will provide a test of neoclassical theory, including the finite-aspect-ratio correction, in the high-beta, collisionless regime.

5. Oscillating-field current drive. STX will attempt to demonstrate current maintenance by oscillating fields. This work will be done in both limiter and divertor plasmas. Experimentally, it will be necessary to oscillate the poloidal and toroidal fields with the proper phase, frequency, and amplitude. Then the oscillations of the radial velocity and poloidal field need to be measured in the plasma. An important issue will be inducing the necessary modification to the q profile without increasing the disruptivity. The experiments will also determinate the effects of field oscillation on confinement.

6. Study of nontokamak configurations. Operated as a pinch or RFP, STX affords the opportunity to study these configurations at low aspect ratio, with large elongation, and with neutral beam heating.

STX DESIGN, COST, AND SCHEDULE

The design details in this proposal represent a point design, the purposes of which are primarily to ensure that a device compatible with the experimental goals is realizable and to allow a cost estimate. A picture of the proposed device is shown below. A true concep-

ORNL–DWG 85-2618 FED

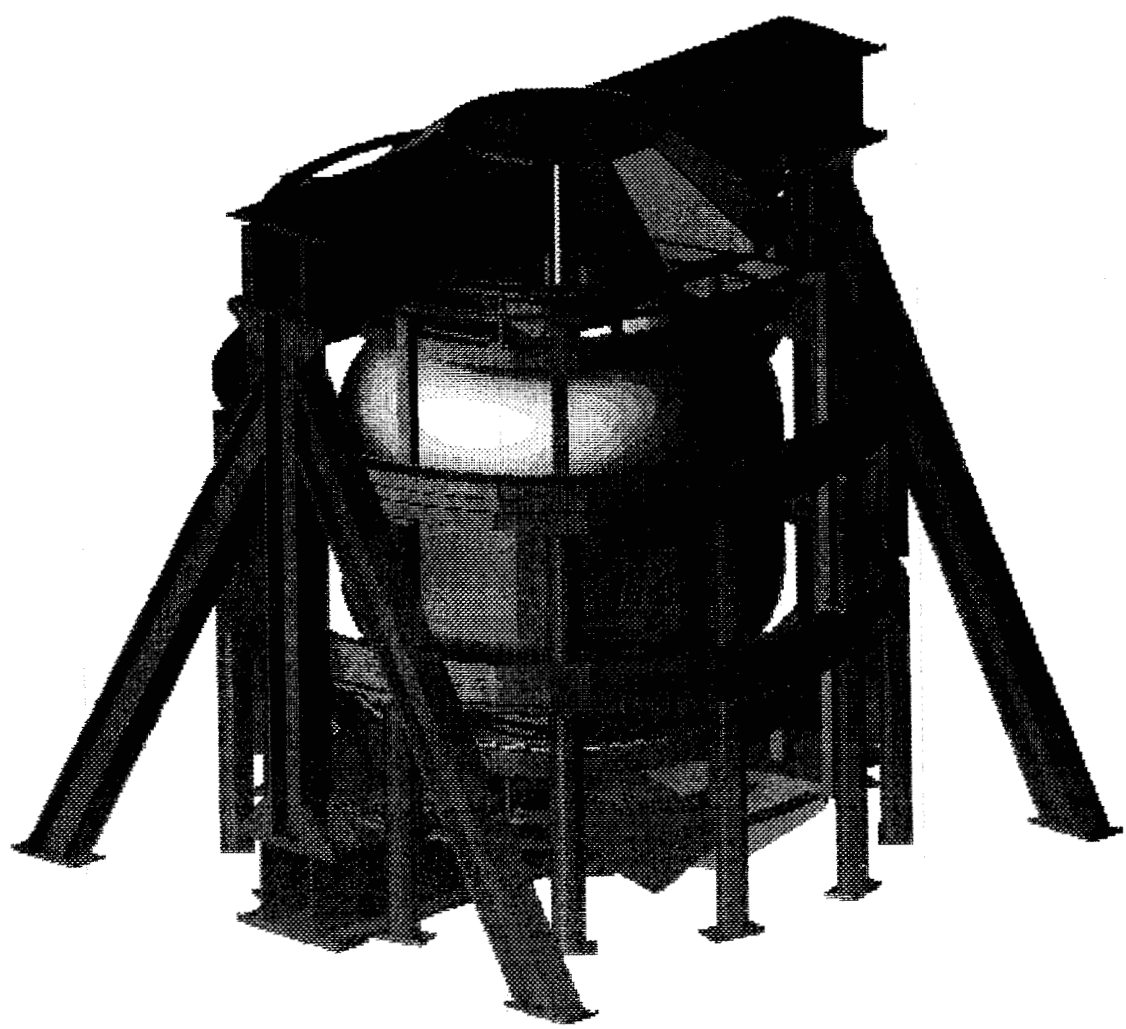

tual design is the next step to be undertaken. Nevertheless, critical design issues have been addressed. Although the solutions presented here may not be the final choices, the design work that has been accomplished allows a clear identification of the major problems and the components that have significant cost impact. Thus, the issues to focus upon during conceptual design have been clearly identified. We have attempted to minimize the cost of STX and the construction time. As a result, upgrades of the experiment will be required in order to realize all the experimental goals. These upgrades are restricted to the power supplies; the device itself is intended to have the capability of completing the mission defined above. In the initial operating phase the plasma current will be limited to 600 kA; a power supply upgrade will be required for 900-kA operation. Also, beta will be limited to 13% (assuming neo-Alcator scaling) and additional heating will be required to achieve 20%. Of course, if the confinement proves to be superior to that predicted from neo-Alcator scaling, the initial operating space will be enlarged. Power supply improvements will also be required for divertor operation, oscillating-field current drive, and reversed-field operation.

We plan to locate the device in the existing High Power Test Facility of the ORNL Fusion Energy Division; hence, the basic facility requirements for an experiment as well as the neutral beam line are already in place. The major components are the magnets, the mechanical structure, the vacuum vessel, and the power supplies. The toroidal field of 0.5 T is achieved with 12 single-turn coils that wedge together on the machine's vertical axis, eliminating the need for a bucking cylinder. The TF coil joint design incorporates a jog on the inside leg of the turns to provide the series connection and avoid TF buswork. A plasma current of 900 kA is driven by a double-swung ohmic heating (OH) solenoid surrounding the central TF leg. The required flux of 0.8 Wb is produced by a water-cooled solenoid with a uniform current density, made of high-strength copper alloy and operating at 10.5 T. A racetrack-shaped, thin-walled, Inconel vacuum vessel was chosen to minimize

the inner radius while maintaining adequate toroidal resistance without bellows or insulating breaks. The poloidal coil design includes vertical, shaping, and radial field coils as well as the OH return windings and coils for an expanded-boundary divertor. Major structural loads are bridged around the vacuum vessel to eliminate the need for support in the central region.

A cost estimate was prepared based on this design. For each element, the cost estimate includes material costs, engineering hours required, and labor hours for fabrication and assembly. The required time for design, procurement, fabrication, and assembly was also used to determine the schedule. The resulting cost is $4.8 million for the device with an additional $1.1 million contingency and $0.9 million escalation over the 30-month schedule. This includes design, fabrication, assembly, installation, and systems testing. It does not include the conceptual design, which is estimated to cost $0.2 million and require 4 to 6 months. A possible funding schedule is shown below.

Possible funding plan

	Funding (in millions of dollars)							
	FY86		FY87		FY88		Total	
	BA	BO	BA	BO	BA	BO	BA	BO
Base	1.4	0.8	2.4	2.7	1.0	1.3	4.8	4.8
Contingency	0.2	0.2	0.5	0.5	0.5	0.5	1.2	1.2
Subtotal	1.6	1.0	2.9	3.2	1.5	1.8	6.0	6.0
Escalation (1.06/year)	0.1	0.1	0.4	0.4	0.3	0.3	0.8	0.8
Total	1.7	1.1	3.3	3.6	1.8	2.1	6.8	6.8

1. INTRODUCTION

The Oak Ridge National Laboratory (ORNL) proposes to build the Spherical Torus Experiment (STX), a tokamak with a very low aspect ratio. The major aspects of the experimental program will be the demonstration of high beta at low collisionality, a test of confinement scaling in a new tokamak parameter regime, and the application of oscillating-field current drive (OFCD). In this introduction, we briefly discuss the dominant characteristics of a spherical torus plasma (Sect. 1.1), the design parameters of STX (Sect. 1.2), the expected contributions of STX to the toroidal confinement program (Sect. 1.3), the future potential of STX (Sect. 1.4), and the cost and proposed schedule (Sect. 1.5). The physics of the spherical torus is presented in Chap. 2. Chapter 3 contains the engineering analysis for STX and data on cost and schedule. Additional information is given in the appendixes.

1.1 ESSENTIAL CHARACTERISTICS OF A SPHERICAL TORUS

Figure 1.1.1 shows a typical tokamak with an aspect ratio (the ratio of the major radius to the minor radius, R/a) $A \simeq 3.3$ and a spherical torus[1] with $A \simeq 1.7$. Here we discuss, at a qualitative level, the two changes that distinguish low-aspect-ratio plasmas. (A detailed analysis is presented in Chap. 2.) The first change is that the variation in the toroidal field B_t over the plasma cross section is increased. At $A = 3.3$, the toroidal field varies by a factor of 2 over the plasma; at $A = 1.67$, it varies by a factor of 4. Second, the plasma shape "naturally" elongates at low aspect ratio. That is, the plasma becomes elliptical, with the field decay index retaining a small value that is typical of a circular plasma at larger A. The combination of these effects results in about a sixfold increase in plasma current I_p for a given toroidal field and value of safety factor q at the edge. (In this document, q without a subscript is the MHD value, $q = d\phi/d\psi$.) In the spherical torus, the

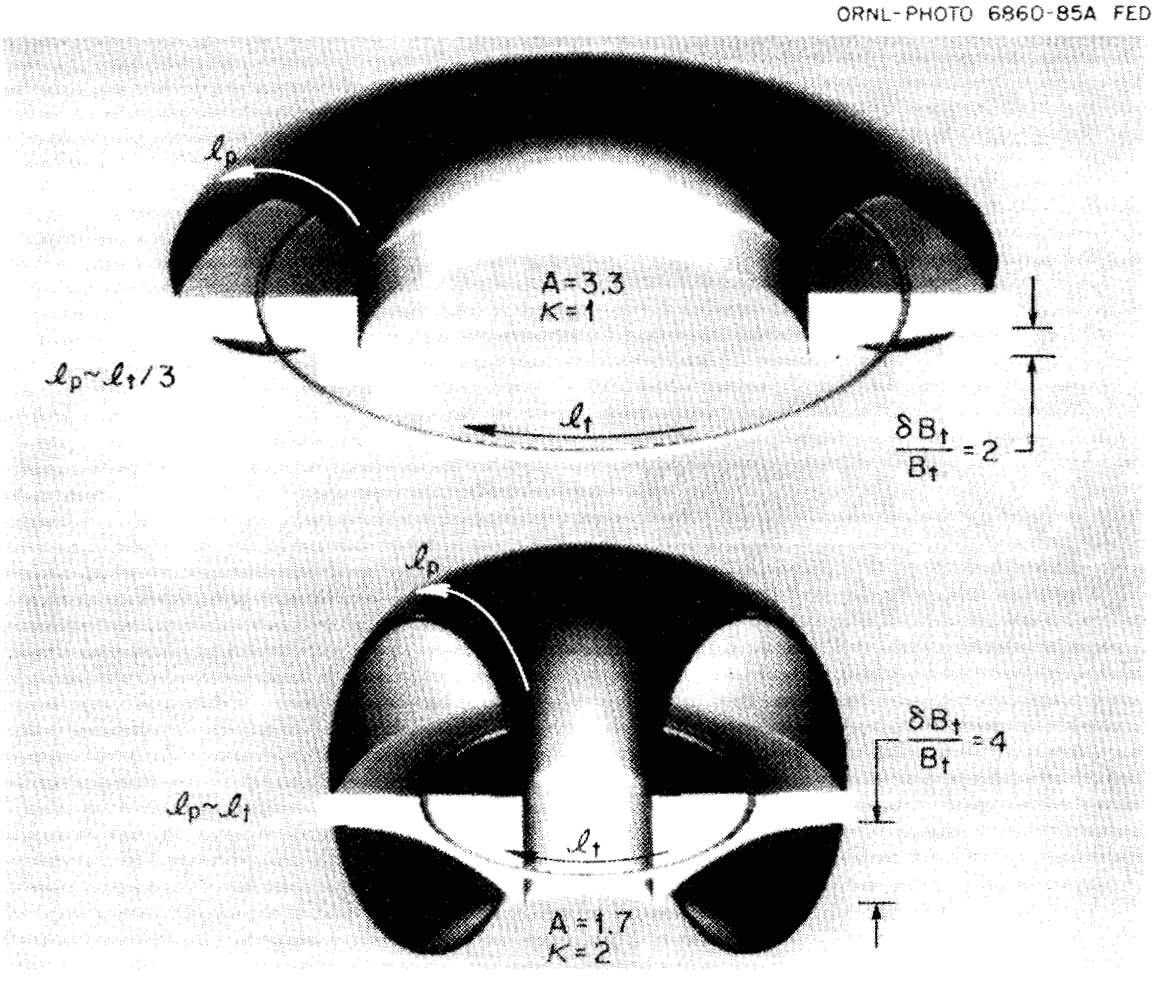

Fig. 1.1.1. Comparison of tokamak and spherical torus plasmas.

poloidal field strength is about equal to the toroidal field strength at the outer edge of the plasma, and as a result the poloidal beta, β_p, and the toroidal beta, β_t, are about equal. The low aspect ratio, high elongation, and low β_p of the spherical torus give rise to a large poloidal current, resulting in a strongly paramagnetic plasma ($B_0 \sim 1.5B_{0,vac}$). This strong paramagnetism is the principal feature that characterizes the spherical torus.

These changes in magnetic topology are expected to provide improved plasma stability. Figure 1.1.2 compares the field lines of a spherical torus and a conventional tokamak. In the outboard region of bad curvature, the field line in a spherical torus is strongly pitched, but on the inboard side the much larger toroidal field requires the field line to

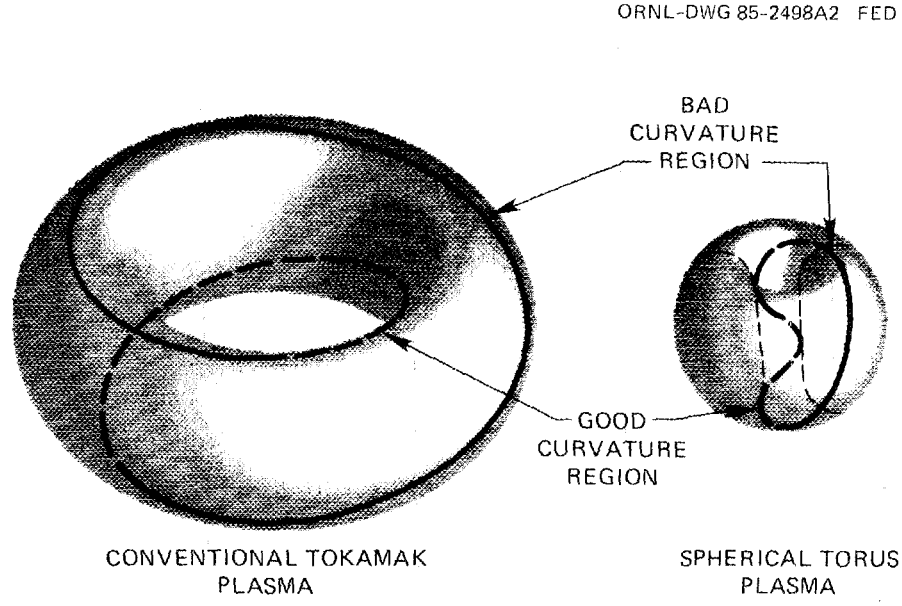

Fig. 1.1.2. Field lines in tokamak and spherical torus. More of the field line in the spherical torus is located in the good curvature region.

travel over a much greater extent. Based on Troyon scaling ($\beta_{max} \sim I/aB$), we expect ideal stability at $\beta > 20\%$. This creates the possibility of high beta without necessitating operation at low q, thus reducing the potential for disruptions at high beta that plagues present experiments. Parenthetically, this configuration retains a flux-surface-averaged magnetic well because of the high poloidal field strength.

The strong paramagnetism distorts the mod-B surfaces, which in a conventional tokamak are nearly vertical cylinders, so that they bulge radially outward at the plasma midplane and become nearly parallel to the flux surfaces in the outboard region. This change is expected to reduce neoclassical transport, since the $\mathbf{B} \times \nabla B$ drift experienced by a trapped particle is reduced. It also moves the turning points for trapped particles out of the bad-curvature region.

The strong paramagnetism may also make it possible to operate a spherical torus as an RFP. After the paramagnetic tokamak plasma is established, the externally applied

toroidal field can be reduced or reversed. Thus, the spherical torus could be operated with a variety of transform profiles, as shown in Fig. 1.1.3.

In considering the potential of the spherical torus as a reactor, we find that it suffers from its small bore and the resulting limitations on ohmic flux. One can consider operating a conventional tokamak as a reactor in a pulsed mode, but this is not possible in a spherical torus. Current drive will be necessary to make the spherical torus a viable reactor concept. Oscillating-field current drive (OFCD),[2] which we propose to test on STX, is particularly attractive at low aspect ratio, which results in a significant reduction in toroidal flux. Because OFCD is an inductive process, it is potentially very efficient in a tokamak. Because the magnitude and frequency of oscillating fields are increased at lower temperature, STX will provide a severe test of this process.

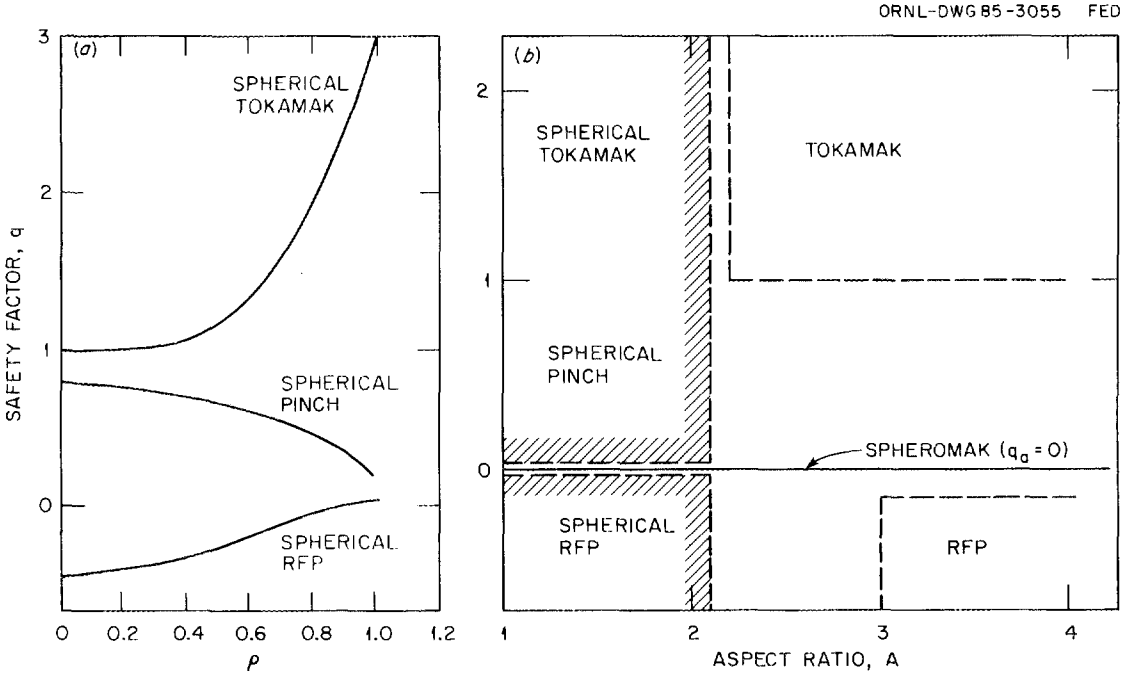

Fig. 1.1.3. (a) The q achievable in a spherical torus. (b) Schematic of toroidal magnetic configuration vs aspect ratio.

1.2 THE STX DEVICE

The device parameters of STX are listed in Table 1.2.1, and a cross section, including the magnet systems and vacuum vessel, is shown in Fig. 1.2.1. The aspect ratio, $A = 1.67$, is chosen so that the device will provide a clear test of the spherical torus concept. The major radius must be in the range between 0.45 and 0.5 m to minimize both the

Table 1.2.1. Parameters of STX

Aspect ratio A	1.67
R_0, m	0.45
a_0, m	0.27
B_t, T	0.5
I_p, MA	0.9 (0.6)[a]
P_b, MW	2.3 (1.5)[a]
Elongation	2
Duration, s (with NBI)	0.5
Divertor	Expanded boundary
Limiter	Top rail, TiC-coated carbon
$B_{solenoid}$, T	10.5
Vacuum vessel	Inconel, racetrack cross section
Shot rate, h^{-1}	20

[a]Values in parentheses are those expected for the initial operating phase.

cost and the heating requirements for demonstrating high beta without being too small to produce the required ohmic flux. This range is consistent with neutral beam heating at power levels that will produce significant beta values ($\beta > 8\%$ per megawatt). The toroidal field is then determined by the Murakami density limit, $n \sim B/R$. The plasma parameters expected, given these constraints, are:

$\tau_E \geq 5$ ms (neo-Alcator scaling at $n_e = 5 \times 10^{13}\,cm^{-3}$),

$\beta > 13\%$ with 1.5 MW of neutral beam injection (NBI),

$T_{i0} \sim T_{e0} \sim 1$ keV,

$\bar{n}_e \sim 5 \times 10^{13}\,cm^{-3}$, and

$\beta_p \sim 0.2$ at 900 kA and 0.45 at 600 kA.

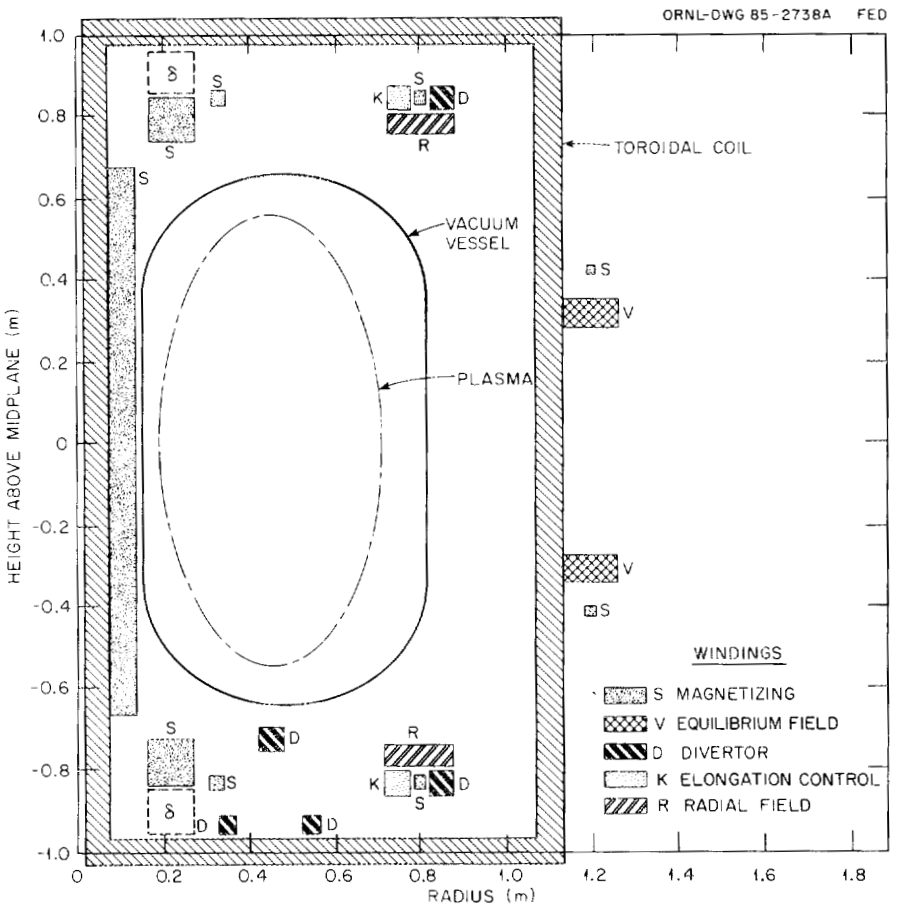

Fig. 1.2.1. Cross section of STX.

1.3 THE ROLE OF STX IN THE TOKAMAK PROGRAM

The critical issues in tokamak research—energy confinement, plasma beta, and steady-state operation—are crucial to the feasibility of an ignition experiment at reasonable cost and to the economy of future fusion reactors. Energy confinement and beta have been studied in the regime where auxiliary power dominates ohmic power in a number of tokamak experiments, including the Impurity Study Experiment (ISX), the Princeton Large Torus (PLT), the Poloidal Divertor Experiment (PDX), the Doublet III tokamak (DIII), and the ASDEX tokamak, and a reasonable consensus has been achieved on the characteristics of such plasmas. We summarize that consensus here.

Energy confinement in limiter plasmas with auxiliary heating is not as good as that obtained with ohmic heating. Although the energy confinement recovers toward the ohmic values with increasing plasma current, it decreases with increasing heating power and quite clearly lacks a density dependence. In diverted plasmas, the situation is more complex, but improved over that in limiter plasmas. At one extreme, the confinement scaling found in limiter plasmas remains and is simply enhanced by a factor that can be varied from about one to two by discharge programming. At the other extreme are plasmas in which careful control permits confinement as good as that in an ohmic plasma. Thus, a single device can have widely different confinement properties, at a fixed input power, depending on details of plasma operation. In all experiments, the degradation of confinement is observed to be primarily in the electron channel. The ISX-B experiments showed that the degradation in confinement was correlated with increased poloidal beta. Causality could not be established, and operating modes (Z-mode) could be found in which the degradation could be mitigated. It was experimentally determined in ISX-B that the cause of degradation was not specific to beam heating effects (such as plasma rotation) and was correlated with magnetic fluctuations. ASDEX experiments showed that H-mode confinement is degraded when operation is near the beta limit.

The achievable beta values have been limited by plasma disruption rather than by confinement. The limiting beta has been found to scale as I/aB, again with a general consensus among the experiments. Stability analysis[3] indicates that this limitation is the onset of an external kink mode that is reached before a ballooning mode limit.[4] The favorable confinement of the H-mode has not been achieved at $q < 3$, despite considerable effort (notably on DIII and more recently on ASDEX).

The STX device is a logical step in the exploration of these critical issues. Proposed confinement scalings that yield similar values for conventional tokamaks yield predictions

that differ by more than an order of magnitude for STX, as described in Sect. 2.4. The STX device has great potential for the resolution of these confinement scalings.

Because of the high plasma current in a spherical torus, the poloidal beta is always small. (More properly, β_p/A is much less than unity even at the highest beta values.) At the same time, high beta can be achieved even at moderate q. In a conventional tokamak, only moderate beta can be achieved at low q. Scenarios for ignition devices usually assume $q \sim 2$ to achieve acceptable beta values; however, in STX we expect $\beta \approx 20\%$ at $q > 3$. This means that operation at high beta without disruption and with a divertor for edge control is more likely in STX than in a conventional tokamak.

Because of its low aspect ratio and small major radius, STX should enter the collisionless regime at a temperature of a few hundred electron volts; with beam heating, STX is expected to produce a collisionless, high-beta plasma—an operating regime that could be reached by a conventional tokamak only under reactorlike conditions at temperatures exceeding 10 keV.

If OFCD pumping proves successful, allowing STX to demonstrate the physics of a steady-state tokamak, and if high beta is achieved, the major physics obstacles presented by the conventional tokamak will be surmounted. The spherical torus will then have demonstrated the feasibility of a compact, low-field device that can operate steady state with a collisionless, high-beta plasma.

1.4 FUTURE POTENTIAL

The spherical torus has several features that make it a potentially attractive reactor concept. First, based on very simple empirical scalings, the reduction in aspect ratio is favorable. The most pessimistic of any proposed confinement scaling is the neo-Alcator scaling, which does not bode well for a spherical torus because of the R^2a size dependence. Here we investigate the consequences of neo-Alcator scaling for a spherical torus reactor.

The quantity of interest is the product of pressure p and energy confinement time τ_E normalized to the externally applied toroidal field B at fixed edge q. We combine the neo-Alcator scaling, $\tau_E \simeq nR^2a$, and the Murakami density limit, $n \sim B/R$, and assume operation at critical beta as expressed by the Troyon limit, $\beta_{max} \sim I/aB$. The resulting scaling is

$$<p>\tau \sim IRB^2 \ ,$$

where we have interpreted B as the externally applied toroidal field. If we interpret B as the total field at the magnetic axis, then the limiting $<p>\tau$ improves by the square of the ratio of the total field to the vacuum field. Thus, provided the plasma current increases faster than the major radius decreases (at constant edge q, vacuum toroidal field, and minor radius), the scaling favors a low aspect ratio. Figure 1.4.1 shows that as A decreases from 3 to 1.5, the major radius decreases by a factor of 2, while the plasma current increases by a factor of more than 5. If total field is used, the gain from halving the aspect ratio increases, by an additional factor of 2 to 3. In this simple analysis the increased beta more than compensates for the poorer confinement.

Now we make a more sophisticated analysis, in which devices at constant fusion power are optimized in terms of minor radius, plasma shape, plasma current, and toroidal field. Operation at the Troyon beta limit with an edge q of 2.75 is assumed in all cases. The toroidal field is constrained to be $\leqslant$10 T at the coils, and space is allowed in the bore for 1 m of blanket and shielding. The fusion power for all cases is 2000 MW(t), as for a small power plant. The variation in tokamak parameters is shown in Fig. 1.4.2. The shaded region represents the uncertainty in the effect of paramagnetism on scaling, as discussed earlier. The increase in major radius for $A < 2$ is caused by the requirement for blanket and shielding space. Figure 1.4.3 shows the requirements for ampere-turn-meters

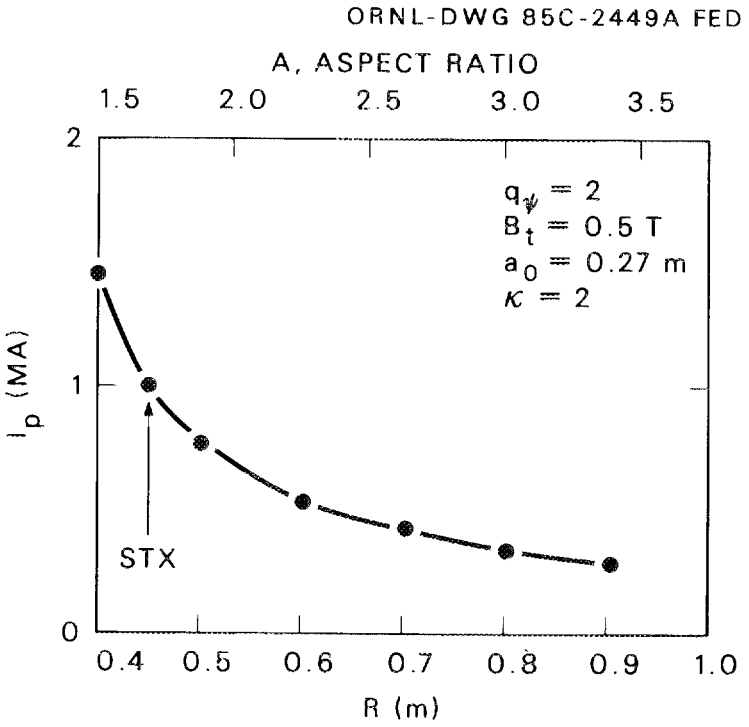

Fig. 1.4.1. I_p increases rapidly with decreasing aspect ratio for $A < 2$.

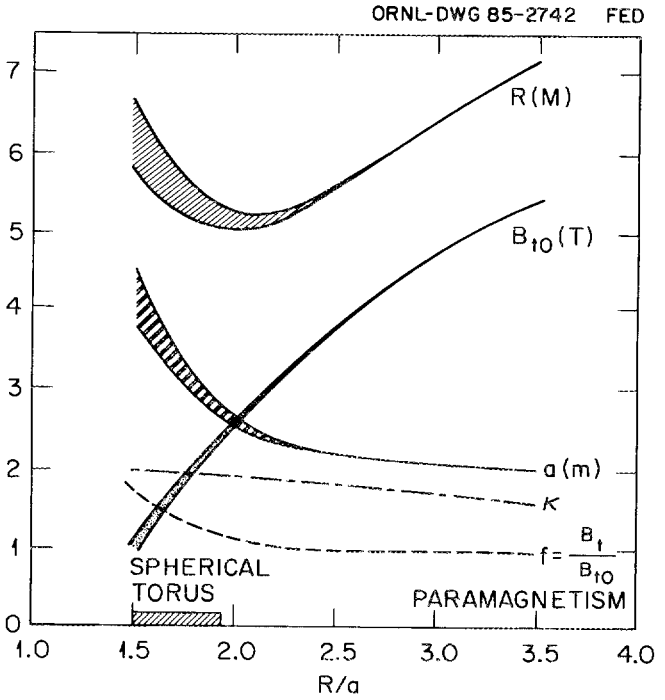

Fig. 1.4.2. Variations of R, a, κ, B_{tot}, and paramagnetism for 2000-MW(t) tokamak reactors restricted by Troyon limit.

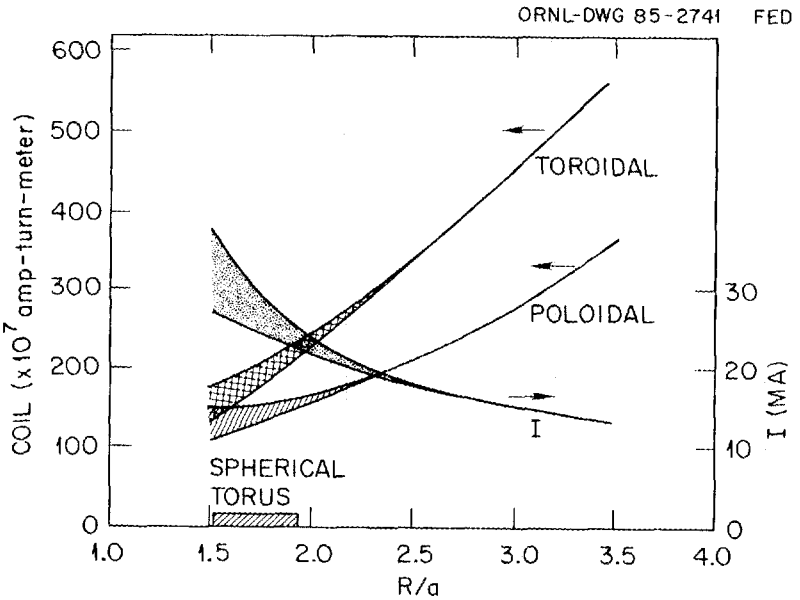

Fig. 1.4.3. Reduction in coil size for 2000-MW(t) tokamak reactor when $R/a = A$ is reduced from 3.5 to 1.7.

of the magnet systems and for plasma current. The mass of the coil system for a spherical torus is about one-third that of a conventional tokamak. The penalty is the increased plasma current, reinforcing the comments in Sect. 1.1 on the need for current drive. One component of the reduction in coil mass is simply the reduction in toroidal field, which reflects the increased beta. Another is the elimination of a requirement for shaping field coils, which constitute a large component of the poloidal coil set at higher aspect ratio. Along with the gain in $<p>\tau$, the device becomes smaller and the neutron flux to the first wall decreases. This can be seen in Fig. 1.4.2, which shows that with decreasing aspect ratio the factor $a(1 + \kappa^2)^{1/2}$ increases faster than R decreases, leading to an increase in the plasma surface area at fixed fusion power. More detailed investigations of the reactor potential of the spherical torus are in progress at Los Alamos National Laboratory for a device with copper coils and at Rensselaer Polytechnic Institute for a device with superconducting coils.

1.5 COST AND SCHEDULE

The anticipated cost of the STX device, based on the design established in support of the physics objectives, is $6.8 million, including contingency and escalation. The device could be built in 30 months on a minimum-slack, critical-path schedule. If the conceptual design is completed in December 1985 and the project begins in January 1986, the STX device will be ready for operation in July 1988. Cost and schedule projections are addressed in detail in Sect. 3.9.

REFERENCES FOR CHAP. 1

1. Y-K. M. Peng, *Spherical Torus, Compact Fusion at Low Field*, ORNL/FEDC-84/7, Oak Ridge Natl. Lab., January 1985; Y-K. M. Peng and D. J. Strickler, *Features of Spherical Torus Plasmas*, ORNL/FEDC-85/6, Oak Ridge Natl. Lab., in press.

2. P. M. Bellam, *Phys. Fluids* **26**, 2519 (1984).

3. F. Troyon et al., *Plasma Phys. Controlled Fusion* **26**(1A), 209 (1984).

4 A. Sykes et al., p. B23 in *Proceedings of the 11th European Conference on Controlled Fusion and Plasma Physics (Aachen, 1983).*

2. PHYSICS OF THE STX DEVICE

2.1 DETERMINATION OF DEVICE PARAMETERS

The major parameters for STX have been selected to highlight the characteristics of the spherical torus, characteristics that become significant for $A < 2$. The STX aspect ratio A is 1.67. At this value, the potential benefits of low aspect ratio are dramatic enough to be readily observable in an experiment with only a rudimentary diagnostic set.

The major radius is determined by the ohmic heating (OH) flux requirements. The ohmic flux dissipation depends on the plasma confinement time. Here neo-Alcator electron confinement is assumed. At fixed A the resistive volt-second consumption is independent of the major radius, since the confinement scales as the cube of the size. The inductive component $L_p I_p$ scales as R_0^2. Referring to Fig. 2.1.1, we set c_λ, the distance from plasma boundary to the inner wall of the vacuum vessel, equal to $(2/30)R_0$ (cm) and c_i, the combination of the thickness of the inner wall of the vacuum vessel and the space necessary for

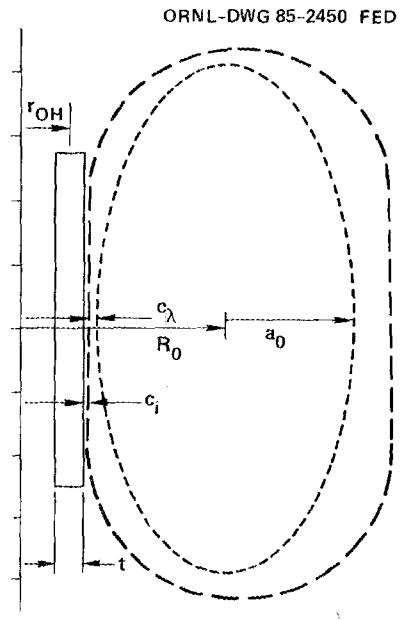

Fig. 2.1.1. Definitions of STX dimensions.

instrumentation (Rogowski coil, flux loops, plasma position sensors, thermocouples, etc.), at 1 cm. A double-swung solenoid is necessary to achieve a volt-second balance. For a rough estimate, we assumed a fixed solenoid thickness t and equated the OH solenoid flux to the flux consumed by plasma operation at $q = 2.3$,

$$2\pi r^2_{\text{solenoid}} B_{\text{solenoid}} = (\text{V} \cdot \text{s})_{\text{res}} + L_{\text{p}} I_{\text{p}} \ ,$$

where

$$r_{\text{solenoid}} = \{[(r_{\text{OH}} + t/2)^3 - (r_{\text{OH}} - t/2)^3]/(3t)\}^{1/2} \ ,$$

$$r_{\text{OH}} = R_0(1 - 1/A - c_\lambda) - t/2 - c_i \ ,$$

and $B_{\text{solenoid}} = 10.5$ T. The 20% additional contribution to the flux from the equilibrium field is taken as a safety margin. Taking

$$L_{\text{p}} \approx \mu_0 R \left(\ln \frac{8R}{\sqrt{ab}} - 2 \right)$$

and I_{p} corresponding to $q = 2.4$, we can solve for R. The volt-second calculation is shown in Fig. 2.1.2 and indicates that 44 cm is the minimum major radius. We have chosen 45 cm for the baseline design study. The toroidal field is then set by the Murakami density limit to be $B_t/R_0 = 1$.

In a more refined calculation, the features of the solution are not changed, but the corrections are quite important. The largest change is the neoclassical correction to the plasma resistivity. (Trapped-particle effects are discussed in Sect. 2.4.) The effect on the

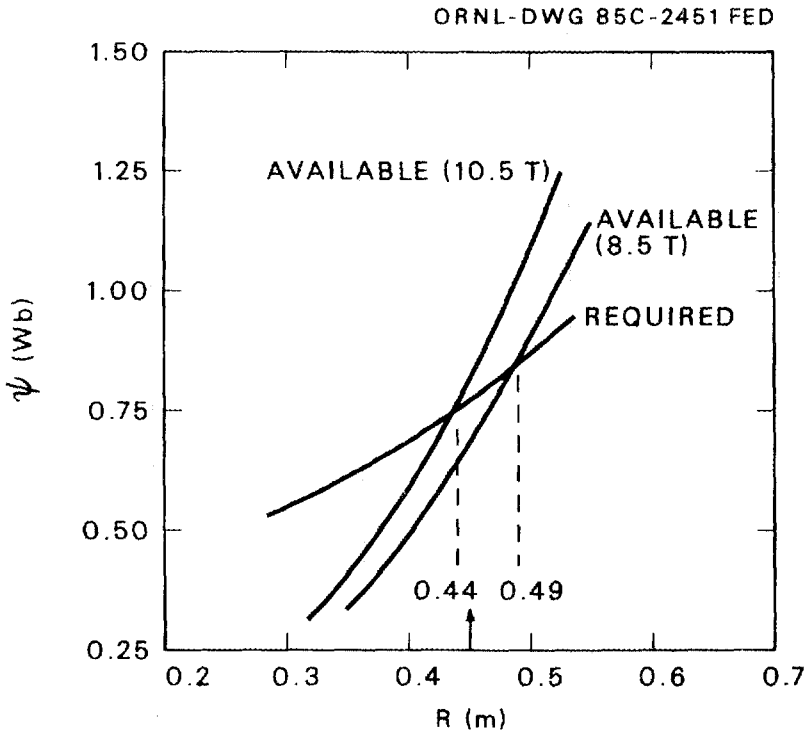

Fig. 2.1.2. Approximate STX volt-second balance.

volt-second balance is to increase the dissipated flux from 0.38 Wb to 0.73 Wb. The approximate plasma inductance has been replaced with a more accurate calculation.[1] In fact, inductance is no longer well defined at this aspect ratio since the poloidal distribution of the surface current is closely related to the flux requirement. However, requiring the plasma boundary to be a flux surface specifies a unique relation between flux and plasma current.[1] The result of the more accurate numerical calculation is to lower external inductance from 0.206 to 0.167 μH. When the presence of an equilibrium field is taken into account, the coupling of the equilibrium field and the OH solenoid by the plasma results in the appearance of an additional 0.066 μH of mutual inductance. It is merely fortuitous that this result and the modified large-aspect-ratio approximation give nearly the same result. Equilibrium calculations yield 0.7 as a typical result for internal inductivity ℓ_i. The flux dissipated in establishing the current profile has been lumped with all other dissipative terms in the value of 0.73 Wb. With the flux return windings described in Sect. 3.1, the

OH flux coupled to the plasma is 0.93 of that obtained in the infinite solenoid approximation.

The revised volt-second balance is shown in Fig. 2.1.3, where the vertical field contribution is included. The intersect has moved to $R = 0.5$ m. For the plasma represented in Table 2.4.1, this balance would result in plasma termination at 385 ms at a current of ~880 kA. For lower-density plasmas with a slightly higher T_e, the volt-seconds are adequate for a pulse length of 450 ms and 900 kA. Also, an increase of size to $R = 0.5$ m is attractive from an engineering point of view, since it eases the design problems for the OH solenoid.

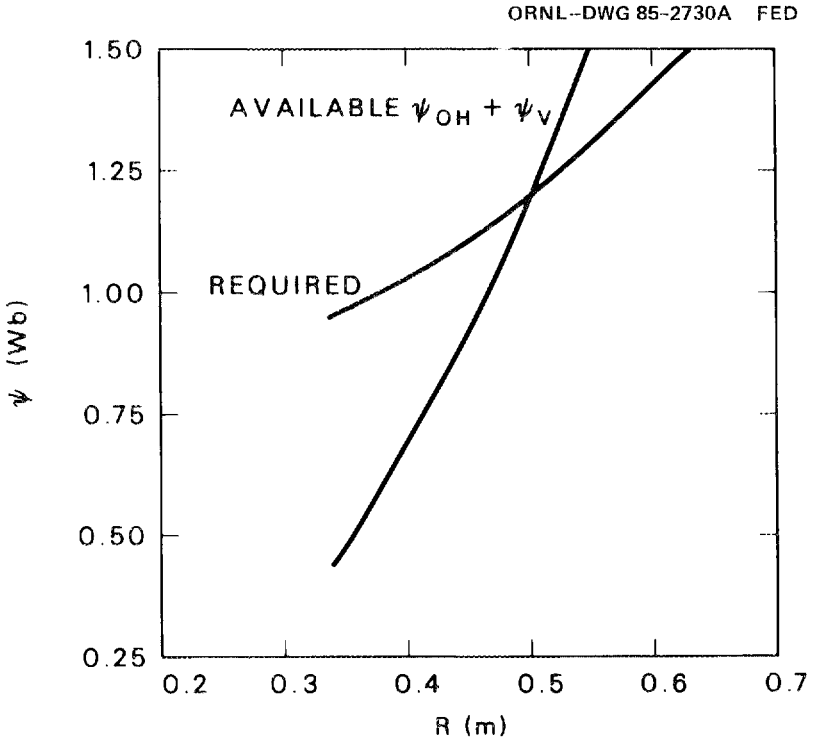

Fig. 2.1.3. STX volt-second balance for $B_{solenoid} = 10.5$ T.

2.2 MHD EQUILIBRIUM

Spherical torus equilibria have a number of important features, as shown by the example of a high-beta equilibrium in Fig. 2.2.1. First, the flux surfaces show high elongation with a shaping coil current that is small compared to that required at larger aspect ratio. Second, the toroidal field within the plasma is substantially higher than the vacuum field. Third, the current profile is very broad. As shown in Sect. 2.3, the current profiles in STX require electron temperatures at the plasma boundary of a few hundred electron volts. The high plasma current is primarily a profile effect. The current density on axis is

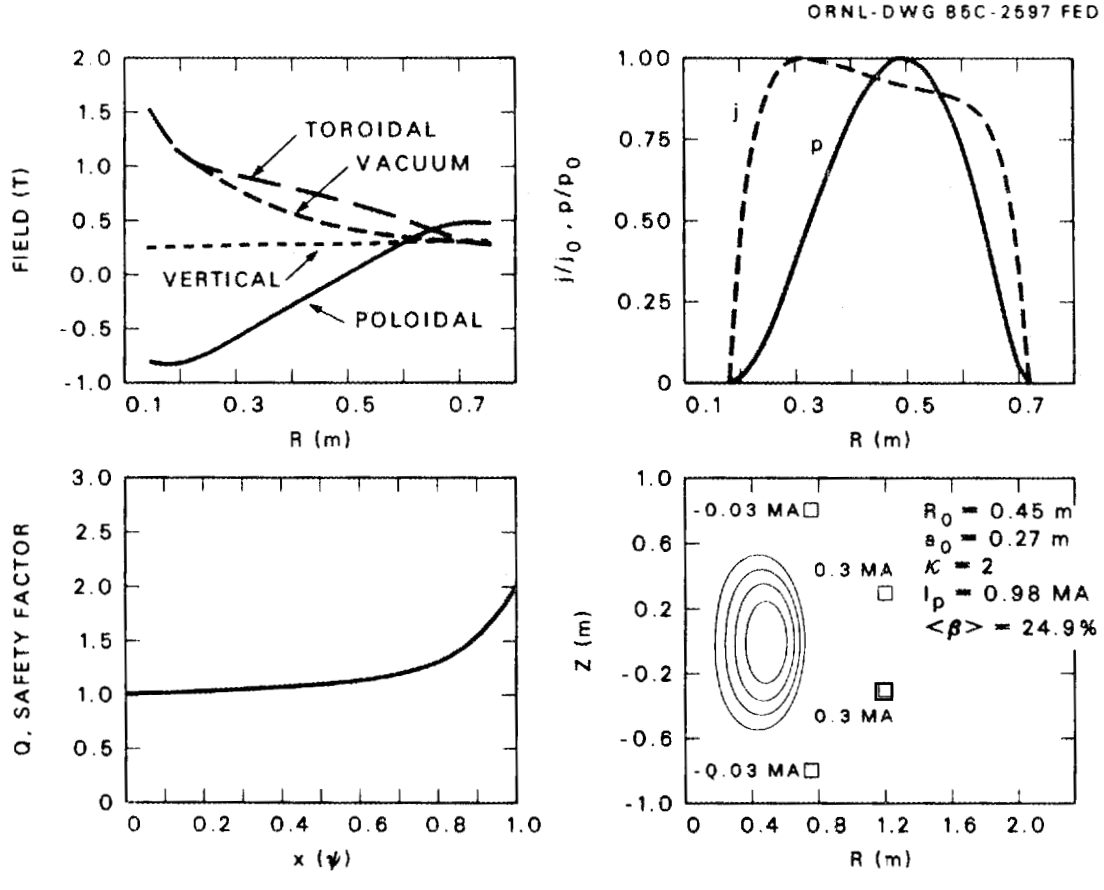

Fig. 2.2.1. High-beta equilibrium.

still restricted by $q_0 = 1$. Thus j_0 is limited to $2B_0/\mu_0 R$. The increase in j_0 due to paramagnetic effects is small compared to the increase in plasma current, and the increased plasma current is essentially a consequence of increased toroidicity. Since poloidal beta remains small in STX, there is not a marked variation in the internal magnetic geometry with increasing beta. A feature of interest is that the mod-B surfaces are no longer vertical but bulge radially outward. Trapped particles will make larger poloidal excursions than in a conventional tokamak with turning points in regions of more favorable curvature. This is discussed in more detail in Sect. 2.8. The equilibrium shown is calculated for beta at the Troyon limit using a coefficient of 0.033. [$\beta_c = 0.033 I/aB$ (MA, m, T)]. Table 2.2.1 shows the important parameters from equilibrium calculations at different q values; the elongation is 2, the external toroidal field is 0.5 T, and beta is at the Troyon limit. Note that the field decay index $(R_0/B_v)(\partial B_v/\partial R)$ is small, typical of the values in circular plasmas at larger aspect ratio. With significant shaping fields, an elongation greater than 3 could be achieved while vertical stability is maintained. An analysis of vertical stability is presented in Sect. 3.1. In the table, I_s and I_v are respectively the required shaping and vertical field currents; B_0 is the total field on axis.

Table 2.2.1. Parameters from equilibrium calculations

Edge q	Plasma current	I_s/I_v	$B_0/B_{0,ext}$	β	β_p	Decay index
2	0.98	0.10	1.52	0.25	0.30	−0.16
3	0.67	0.17	1.27	0.16	0.40	−0.19
4	0.51	0.22	1.17	0.12	0.51	−0.20

2.3 MHD STABILITY

Ideal Modes

Studies of the MHD stability and of the dynamic properties of STX are in progress. One of the primary factors motivating the STX concept is the prospect of achieving high

beta, as suggested by the extrapolation of Troyon's empirical scaling formula[2] to low aspect ratio ($A < 2$), shown in Fig. 2.3.1. This expression for the maximum beta equilibrium stable to long-wavelength (low toroidal mode number n) free boundary modes, ballooning modes, and Mercier modes on axis was derived from a study of the stability properties of the Joint European Torus (JET) ($A = 2.36$) and the International Tokamak Reactor (INTOR) ($A = 4$). The highest beta values attained in tokamaks equipped with strong auxiliary heating have been found to be near the limit given by this scaling law, but neither experimental nor theoretical results have been obtained for aspect ratios smaller than that of JET. One important goal of the MHD stability studies for STX is to extend the critical beta scaling to small aspect ratios. To do this, detailed equilibrium parameter studies are being undertaken, together with free boundary $n = (1–3)$ stability calculations and ballooning stability calculations. As a first step, the stability properties for the JET

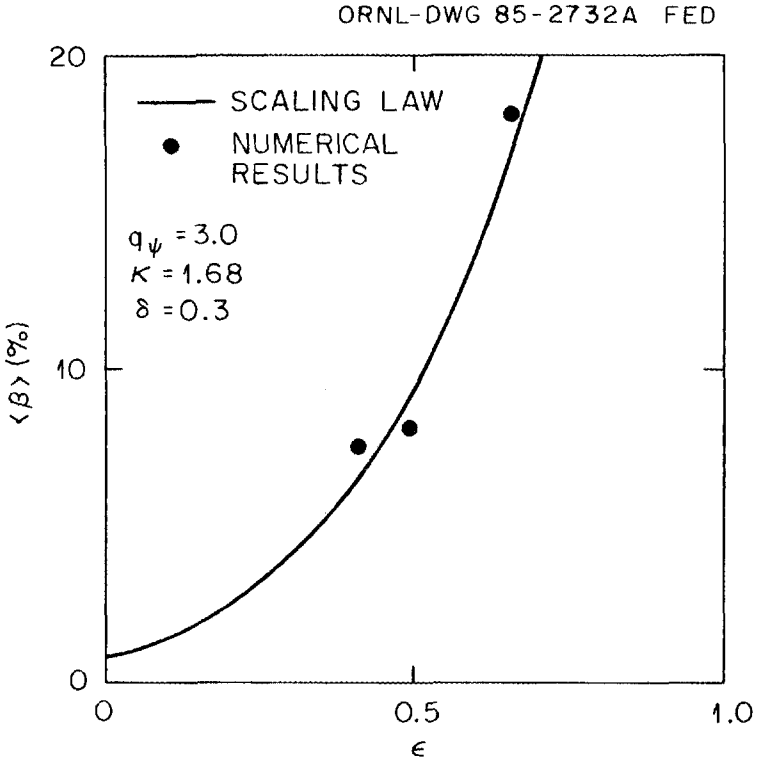

Fig. 2.3.1. Comparison of calculated beta limit and Troyon scaling vs inverse aspect ratio (beta referenced to vacuum magnetic field).

equilibrium given by Troyon have been studied at the smaller STX aspect ratio. The particular parameterization used to fit the Troyon JET case is

$$q = 1.6\frac{1 + 1.02\rho^6}{1 + 0.42\rho^2}$$

with the pressure

$$p \propto 1 - 0.2\psi - 2.6\psi^2 + 1.8\psi^3 \ ,$$

where the poloidal flux ψ varies between 0 at the magnetic axis and 1 at the plasma edge. In the calculations presented here, the outer boundaries are parameterized as

$$R = R_0 + a\cos(\theta + \delta\sin\theta) \ ,$$

$$Z = a\kappa\sin\theta \ ,$$

where κ is the elongation and δ is the triangularity. The horizontal aspect ratio is defined as $\epsilon = a/R_0$. This is the same parameterization used by Troyon. For this particular case we use $\kappa = 1.68$ and $\delta = 0.3$, the JET values used by Troyon, and consider the larger inverse aspect ratios $\epsilon = 0.5$ and 0.7. For this particular case the maximum stable beta ($= 2\langle p\rangle/B_{vac}^2$) as a function of aspect ratio has been compared with the critical beta β_c given by

$$\beta_c = 3.3\frac{I_p}{aB_{vac}} \ ,$$

where B_{vac} is the toroidal field at the magnetic axis without plasma; the results are shown in Fig. 2.3.1. It can be seen that the numerical results agree well with the scaling law, although it must be stressed that no attempt has been made to optimize the $\epsilon = 0.5$ and $\epsilon = 0.7$ cases.

The effects of elongation and triangularity on ballooning stability at the STX aspect ratio for fixed equilibrium profiles have also been studied. Only the optimal JET case given by Troyon has been considered so far. The results are summarized in Figs. 2.3.2 and 2.3.3, where the critical values of beta as functions of ellipticity (at $\delta = 0.13$, $\delta = 0.3$) and triangularity (at $\kappa = 2$) are shown, respectively. It can be seen that increasing the triangularity is always beneficial to ballooning stability, whereas at a given triangularity an optimal elongation exists for ballooning stability. These results may be understood in terms of the analytic treatment given by Pogutse,[3] in which it is shown that the magnetic well deepens with triangularity but an optimal ellipticity exists at which the magnetic well is

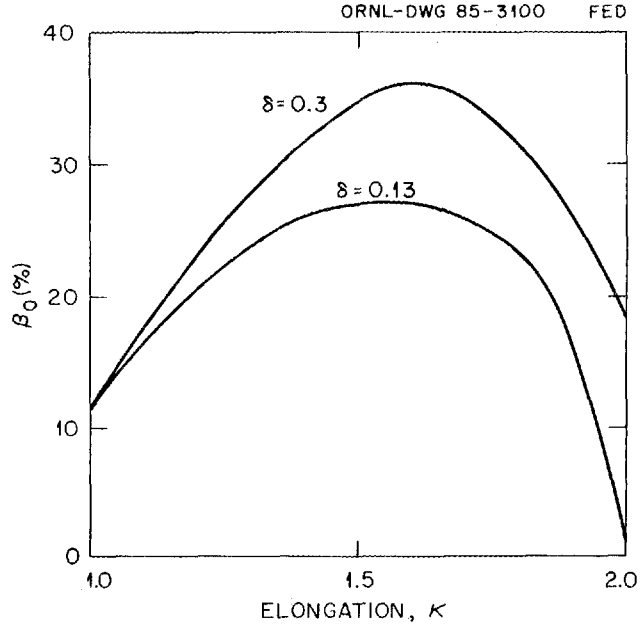

Fig. 2.3.2. Ideal ballooning stability limits vs elongation for two values of triangularity at $A = 1.67$. For the pressure profile used, $<\beta> \sim \beta_0/2$.

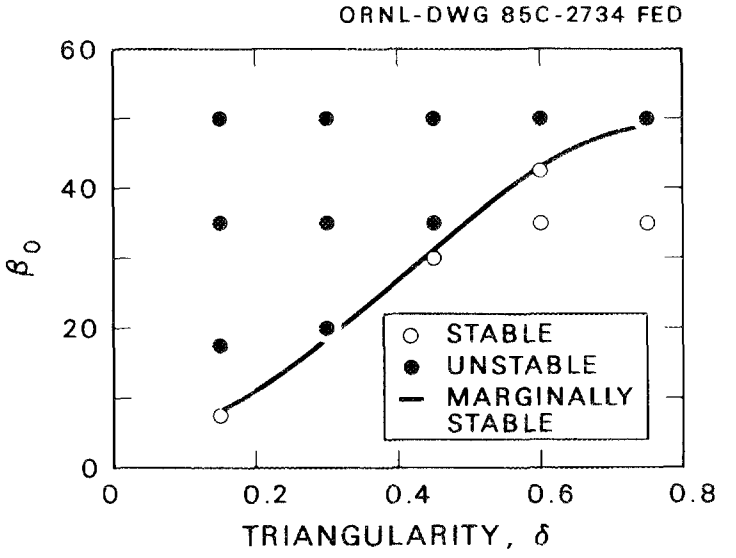

Fig. 2.3.3. Ideal ballooning stability limits vs triangularity at fixed A and κ.

deepest. At large triangularity this optimal ellipticity is 1.6, which agrees with the numerical results given here. These results show a strong dependence of the ballooning stability on shaping, seemingly in contradiction to Troyon, who finds only a weak variation in the β_c scaling with ellipticity. It must be remembered, however, that no attempt has been made to optimize the profiles for ballooning stability, so the critical beta (when this procedure is carried out) may well be relatively insensitive to shaping.

Using the studies described to fix the elongation at $\kappa = 1.7$ and the experimental constraints to find $\delta = 0.3$, a simultaneous study of low-n and $n = \infty$ modes has been started. For selected cases the most unstable low-n toroidal wave number was found to be $n = 1$. Thus, only $n = 1$ low-n modes were considered for the full study. The low-n studies were done with the computer code ERATO,[4] which uses a δW approach to solve the basic low-n ideal MHD stability problem. For the surveys, a spatial grid of 60 $\times$ 60 was used. This gives the stability trends even though a convergence study (extrapolation to zero grid spacing) is needed (and was used) to establish stability. Stability for $n = 1$, $n = \infty$, and Mercier modes has been found for an equilibrium with $\bar{\beta}(= 2\langle p \rangle / B_{vac}^2) = 20\%$. This

is without profile optimization and maintaining a constant pressure profile. The pressure profile was given above and the q profile used was

$$q = q_0 + q_1\psi^{n_1} + (q_a - q_1 - q_0)\psi^{n_2} \ .$$

This allows considerable freedom in varying the shape of the q profile, as well as the values at the axis and at the edge.

In Fig. 2.3.4 normalized growth rates (normalized to the largest value on each curve) are shown as a function of changes in the q profile. The cases shown have $\bar{\beta} = 25\%$. For Fig. 2.3.4(a), q_a was varied with q_0 held fixed. As is true at larger aspect ratio, the larger the value of q_a, the greater the stability for low-n modes, with the opposite true for $n = \infty$. Thus, $n = \infty$ modes are most stable with a broad safety factor profile with $n = 1$ most stable for a narrow profile. The intermediate value of $q_a = 3.5$ offers the greatest stability against both high-n and low-n modes. The effect of varying the q profile shape while holding the axis and edge value fixed was studied and is shown in Fig. 2.3.4(b). The

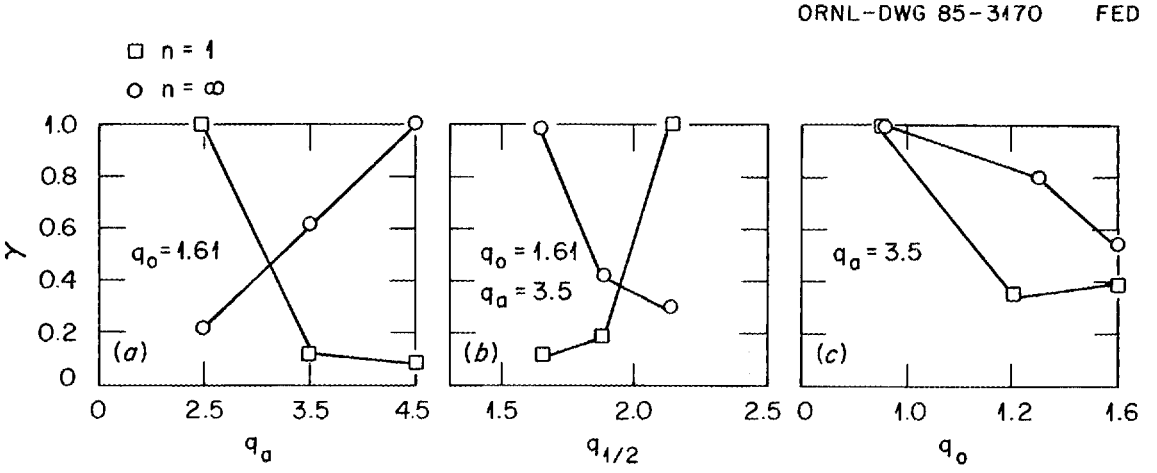

Fig. 2.3.4. Effect of varying the q profile on stability of $n = 1$ and $n = \infty$ ideal growth rates.

change in shape is parameterized by $q_{1/2}$, which is the value of the safety factor at $\psi/\psi_a = 1/2$. As $q_{1/2}$ is made larger, $n = \infty$ becomes more stable and $n = 1$ more unstable. This is consistent with Fig. 2.3.4(a), since the outside of the q profile is becoming wider as $q_{1/2}$ increases, and this is the region where both the $n = 1$ and $n = \infty$ modes are most strongly driven (by the pressure gradient for $n = \infty$ and by the current density gradient for $n = 1$). For all equilibria other than those used for Fig. 2.3.4(a), $q_{1/2} = 1.65$. Results when q_a is varied are shown in Fig. 2.3.4(c). As q_0 is made smaller and the q profile narrower, $n = \infty$ modes become more unstable and $n = 1$ modes more stable until the $q = 1.0$ surface enters the plasma, which strongly destabilizes the $n = 1$ mode, as expected. The equilibrium with $q_a = 3.5$, $q_0 = 1.61$ and $q_{1/2} = 1.65$ [used for the center point in Fig. 2.3.4(a)] was found to be stable for low-n modes when a convergence study was done. This is shown in Fig. 2.3.5, where the calculated values of the growth are squared are shown vs the number of grid points (the scale is $1/N^2$ with N the number of grid points.)

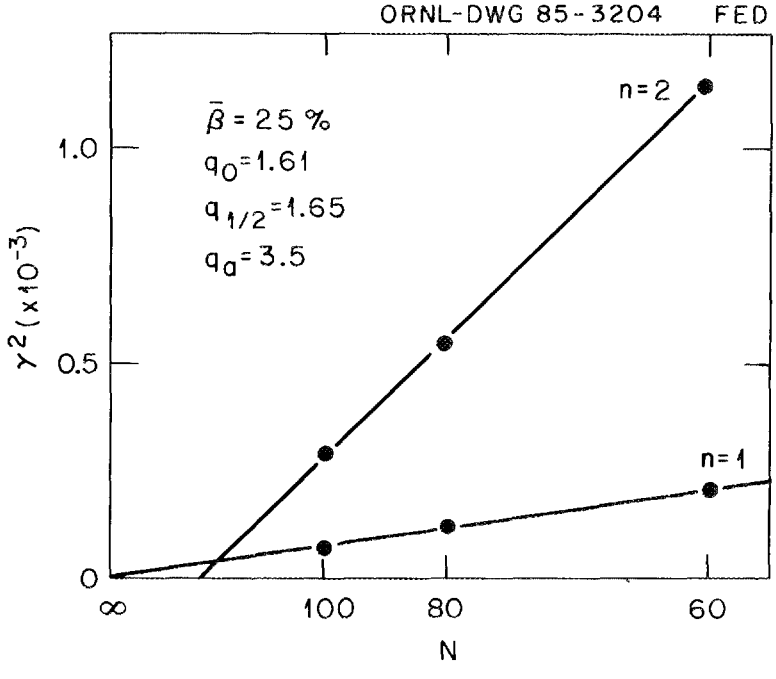

Fig. 2.3.5. Number of grid points N in the poloidal and radial directions vs growth rate squared.

This equilibrium is, however, $n = \infty$ unstable. Lowering $\bar{\beta}$ reduced the $n = \infty$ growth rate as shown in Fig. 2.3.6, where marginal stability is found for $\bar{\beta} \gtrsim$ 20 %. Somewhat higher $\bar{\beta}_c$ may have been found by using a higher value for $q_{1/2}$, as suggested by Fig. 2.3.4(c). The value for q_0 of 1.61 was consistent with that used in the Troyon study, which gave $\bar{\beta}_c$ values somewhat more pessimistic than those found experimentally. Future studies will include profile optimization, which may lead to even higher beta values.

Tearing Modes

The safety factor profiles that are favored by the ideal stability calculations are the types of profiles that show strong tearing instabilities in the cylindrical limit. Therefore, in the spirit of present disruption models,[5] the effects of low aspect ratio on the nonlinear

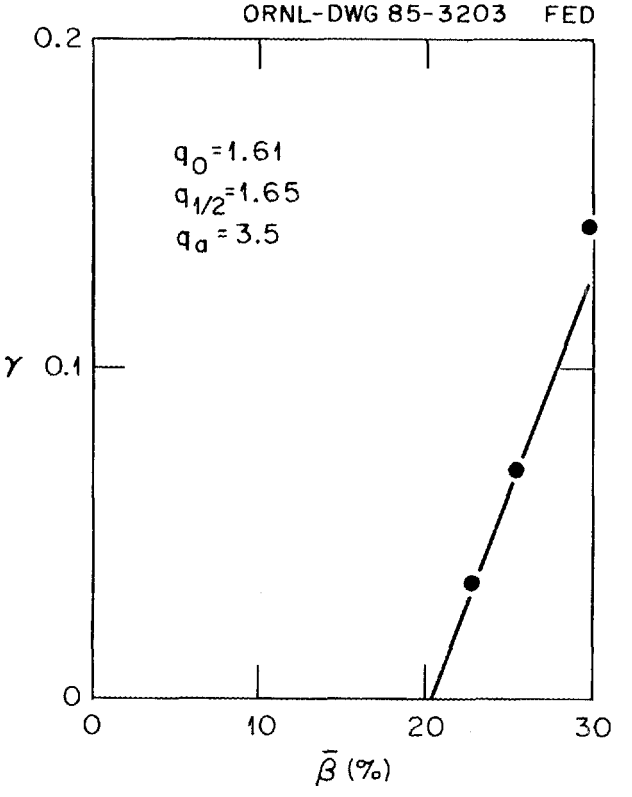

Fig. 2.3.6. The $n = \infty$ growth rate vs $\bar{\beta}$.

interaction of tearing modes are being investigated. Because calculations are being carried out at small aspect ratio, a full set of MHD equations is solved in toroidal geometry, using the computer code FAR.[6] Issues to be studied include the effects of plasma cross section shaping, of equilibrium modification due to toroidicity, and of the geometric coupling of "satellite" modes due to toroidicity and shaping on the evolution and nonlinear interaction of tearing modes. To isolate the effects of toroidal modification of the equilibrium, two equilibrium scans with different constraints have been studied:

1. A scan in which the q profile is maintained constant as the aspect ratio is varied. The profile form is

$$q = 1.34[1 + (\rho/0.56)^8]^{0.25} ,$$

   where ρ is a generalized radial variable that changes between 0 at the magnetic axis and 1 at the plasma edge. This particular q profile has been extensively used in major disruption studies.
2. A scan with the constraint that the FF' term that occurs on the right-hand side of the Grad-Shafranov equation is maintained constant. The form chosen for FF' is that of the constant-q scan at $\epsilon = 0.41$; thus, the two scans intersect at $\epsilon = 0.41$.

While nonlinear studies of the effects of plasma cross section shaping have not been performed (present nonlinear results are restricted to cases with circular cross section), linear calculations of the $n = 1$ eigenfunction, which for the present profiles is dominated by the $m = 2$ component, do not show strong sensitivity to the shape of the plasma (Fig. 2.3.7). For plasmas having a variety of cross-sectional shapes, the linear growth rates, calculated at $S \equiv \tau_R/\tau_{Hp} = 10^5$, where τ_R is the resistive skin time and τ_{Hp} the poloidal Alfvén time, are slightly stabilized at large values of elongation or triangularity

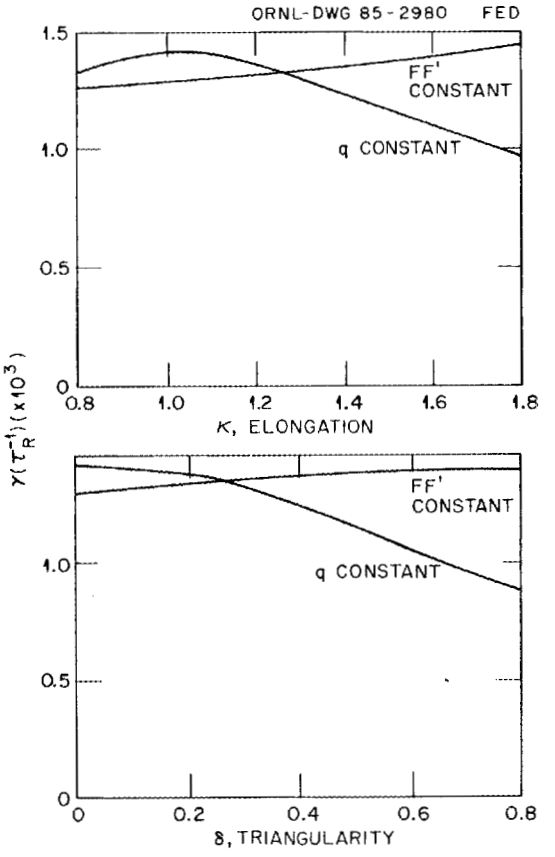

Fig. 2.3.7. Shaping dependences of $n = 1$ tearing mode linear growth rate.

for the constant q scan but are virtually unchanged for the constant FF' scan (Fig. 2.3.7). This indicates that the slight stabilizing effect observed in the constant q scan is due to the effect of the change in shape on the equilibrium current profile. The remaining resistive MHD results to be shown are carried out for circular cross section plasmas.

The effect of equilibrium modification due to increasing toroidicity is clearly illustrated in Fig. 2.3.8. Aspect ratio scans were carried out for $n = 1$ and $n = 2$ eigenfunctions under the assumptions of constant safety factor q and of constant FF'. The scans were carried out keeping $S_A \equiv S/\epsilon = \tau_R/\tau_A = 10^5$, where τ_A is the fast Alfvén time. This corresponds to varying the major radius for fixed minor radius in the scans. The relative stabilization observed in the constant q scan (for which toroidal effects modify the current profile significantly) as compared with the scan for constant FF' (for which the

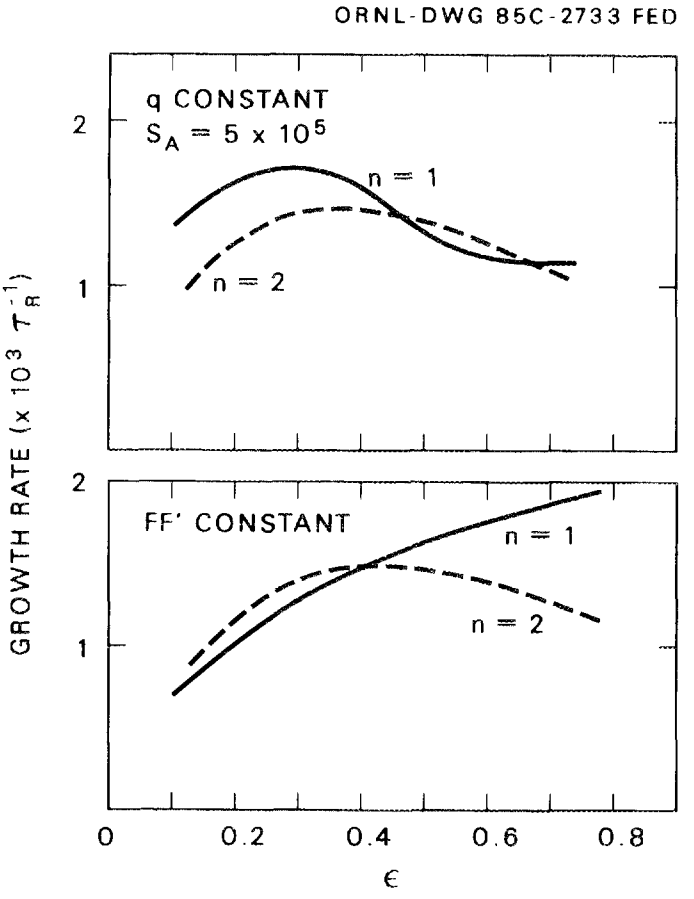

Fig. 2.3.8. Growth rate of $n = 1$, $n = 2$ tearing modes vs inverse aspect ratio.

modification of the current profile is much smaller) shows the stabilizing effect of toroidal modification of the equilibrium profiles. Furthermore, the strength of these couplings increases with ϵ, as shown in the magnetic energy spectrum of the $n = 1$ eigenmode in Fig. 2.3.9.

The destabilizing effect of the toroidal coupling to satellite modes is shown in Fig. 2.3.10. This figure shows aspect ratio scans carried out for constant q profile at fixed $S = 10^5$ for the $n = 1$ eigenfunction in cylindrical geometry (varying the cylinder length) and in toroidal geometry. In cylindrical geometry, where there is no toroidal coupling, the growth rate of the ($m = 2$; $n = 1$) mode has only a slight variation as the length of the cylinder is shortened. The bottom curve labeled "$m = 2$ only" was calculated in toroidal

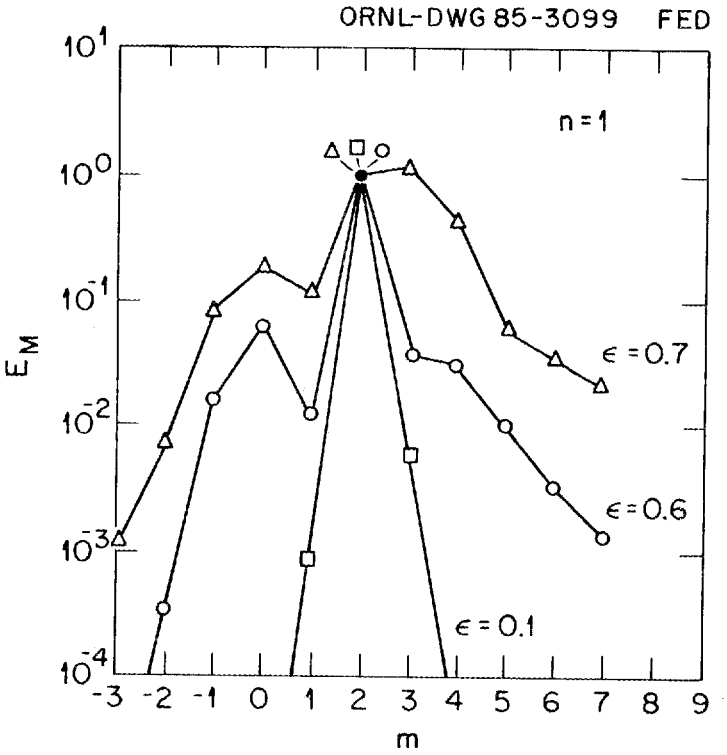

Fig. 2.3.9. Broadening of the *m* spectrum with decreasing aspect ratio.

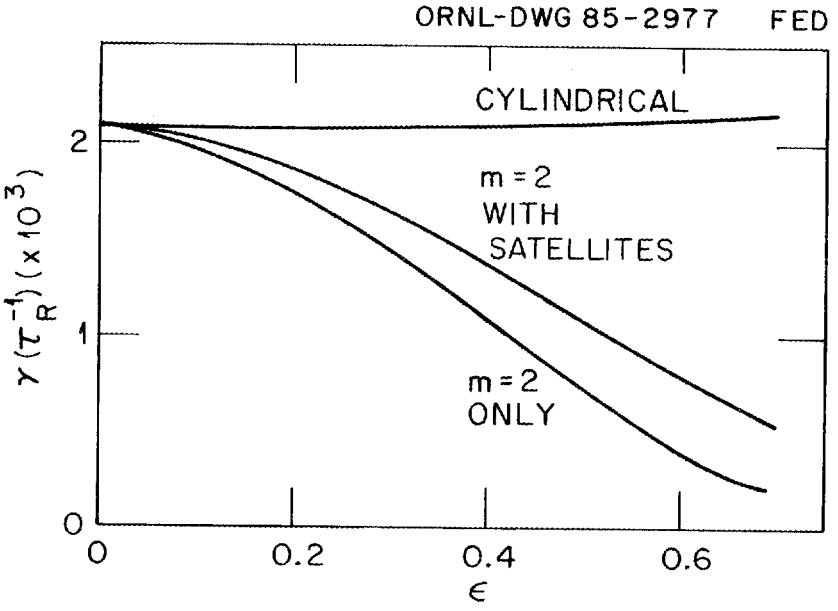

Fig. 2.3.10. Growth rate of $n = 1$ tearing mode with cylindrical limit, effect of toroidicity, and effect of satellite coupling.

geometry without including the higher and lower sideband m's. The stabilizing effect of the toroidally modified equilibrium, compared with that obtained in cylindrical geometry, is apparent. The third curve, which is obtained from a toroidal calculation including the satellite modes, demonstrates the destabilizing effect of these couplings.[7]

Nonlinear calculations for these cases are in progress, with the ultimate goal of understanding the effects of toroidicity on mode interaction and on disruptions. As a first study, the effects of decreasing aspect ratio are being examined for "single-helicity" calculations of the (2/1) mode, including its satellite modes and their harmonics. A similar exercise is being performed for the (3/2) instability. The saturated magnetic island widths exhibit strong reduction with decreasing aspect ratio, as shown in Fig. 2.3.11, which shows the (2/1) island evolution for a constant q scan. Results for the constant FF' scan are similar, but less pronounced, with saturated island widths of W/a = 0.39, 0.28, and 0.15 for ϵ_0 = 0.1, 0.4, and 0.7, respectively. Partial results for the (3/2) mode suggest similar behavior.

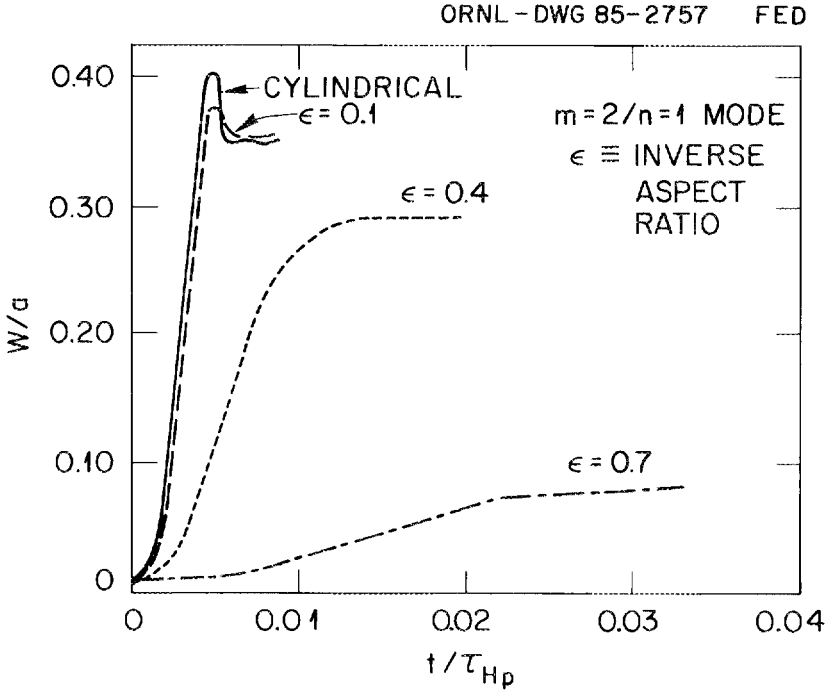

Fig. 2.3.11. Strong reduction of the "saturated" island width with decreasing aspect ratio.

The magnetic field lines for the saturated (2/1) driven instability are shown in Fig. 2.3.12. The reduction in the saturated width of the (2/1) magnetic island for decreasing aspect ratio is associated with an increase in the toroidally generated satellite modes. A study of the overall effect of these variations on the nonlinear interaction of the (2/1) and (3/2) modes has not yet been carried out.

In summary, MHD studies for STX show promising results. While not yet optimized, present stability tests based on ballooning and low-n free boundary calculations indicate high-beta accessibility ($<\beta> \sim 20\%$ at $q \sim 3$) in the first stability regime. The resistive tearing instability is less severe at low aspect ratio when comparisons are made at the same q values. Further work is being performed in equilibrium and ideal stability to optimize the stable beta region for ballooning and low-n modes and in resistive MHD to determine the effects of small aspect ratio on the nonlinear interaction of tearing modes. Further MHD work is also required to study OFCD and the operation of STX in a new regime as a small-aspect-ratio RFP.

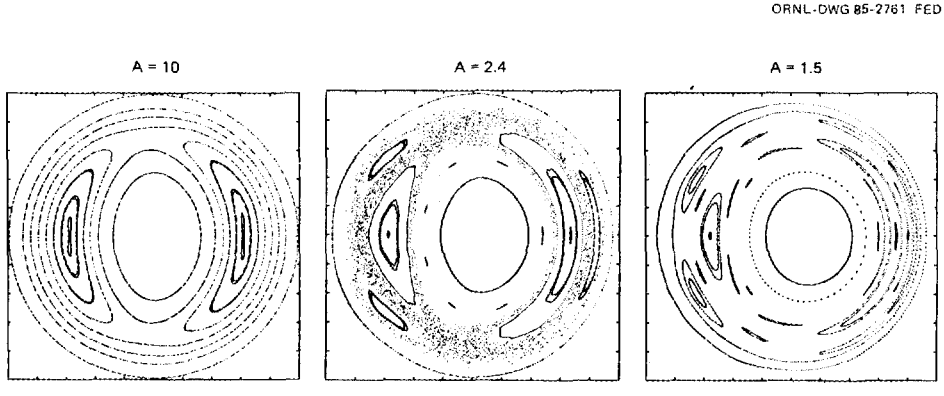

Fig. 2.3.12. Aspect ratio scans of plasmas with circular cross sections, showing magnetic field line structure at saturation for an ($m = 2$; $n = 1$) mode driven instability.

2.4 TRANSPORT

The low aspect ratio and high-current capability of STX make it an extremely sensitive test for confinement scaling laws. The discrepancy among these laws is only a small factor in a tokamak, but in a spherical torus, the difference in the predictions becomes quite large. For ohmic plasmas, the size scaling remains uncertain; both R^2a and a^2 have been proposed. The ratio of these is R^2/a, which ranges from 2.5 to 7 in present tokamaks. The scatter in confinement results from a single experiment is typically a factor of 2, making it difficult to resolve this uncertainty. In STX, the ratio R^2/a is 0.75, which will provide a significant extension of the data base. Table 2.4.1 lists confinement scaling predictions for STX. The device design is based on the neo-Alcator scaling.

The question of confinement degradation with beam heating is difficult to address, since we will operate at points in $\langle\beta\rangle$, β_p space that are far from those accessed by current tokamaks. If we apply Goldston's empirical scaling,[8] then $\tau_E^{aux} > \tau_E^{neo\text{-}Alc}$ for plasma currents $I_p > 133$ kA. The ISX scaling ($0.29\sqrt{I}/\beta_p^2$) leads to a similar result. In fact, any one of the proposed empirical scalings for electron confinement with auxiliary heating

Table 2.4.1. Confinement predictions for STX

Scaling	Confinement time (ms)
OH confinement	
Neo-Alcator	5
INTOR	18
Gruber	56
Mirnov	95
Beam-heated confinement	
ISX	44
Kaye	38
Goldston	41
Gruber	24
ASDEX-L	26
ASDEX-H	37

results in $\tau_E^{aux} > \tau_E^{neo\text{-}Alc}$. In the transport simulations, we assume no degradation of confinement from the ohmic values.

Another feature of the low aspect ratio is that STX is expected to operate in the collisionless regime even for ohmic plasmas. With beam heating, the transport simulations indicate that most of the plasma is well into the collisionless regime ($\nu_* \ll 1$). Thus, we expect operation simultaneously at high beta and low collisionality. The low collisionality is expected to enhance the plasma resistivity. At this aspect ratio, the trapped particle fraction cannot be geometrically approximated, and a pitch-angle-weighted measure of the trapped fraction is used in evaluating the plasma resistivity.[9] The trapped fraction under typical conditions is shown in Fig. 2.4.1 for several aspect ratios. For reference, the large-aspect-ratio limit of $(3/\pi)(2/A)^{1/2}$ is also shown. We find that the drift parameter v_D/v_{th}, while larger than in a conventional tokamak, is still much less than unity; $v_D/v_{th} \sim 0.14$ at the plasma edge.

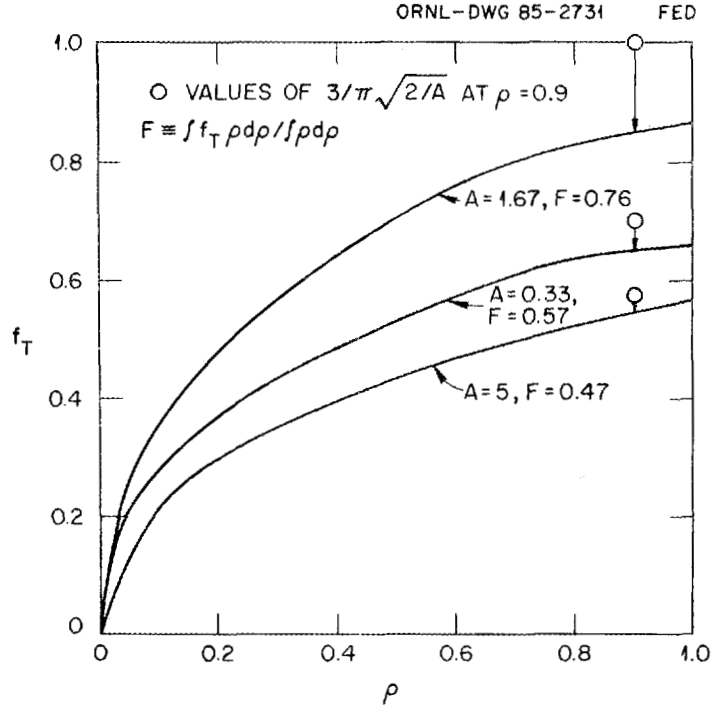

Fig. 2.4.1. Pitch-angle-weighted trapped fraction for different aspect ratios.

Transport simulations have been performed using the WHIST code[10] for a variety of conditions. The power balance in Fig. 2.4.2 corresponds to the case shown in column 1 of Table 2.4.2; profiles are shown in Fig. 2.4.3. As can be seen, the electron channel dominates, with most of the power flowing into the electrons and being lost by electron heat conduction. Confinement times for the ions are much longer than those for the electrons.

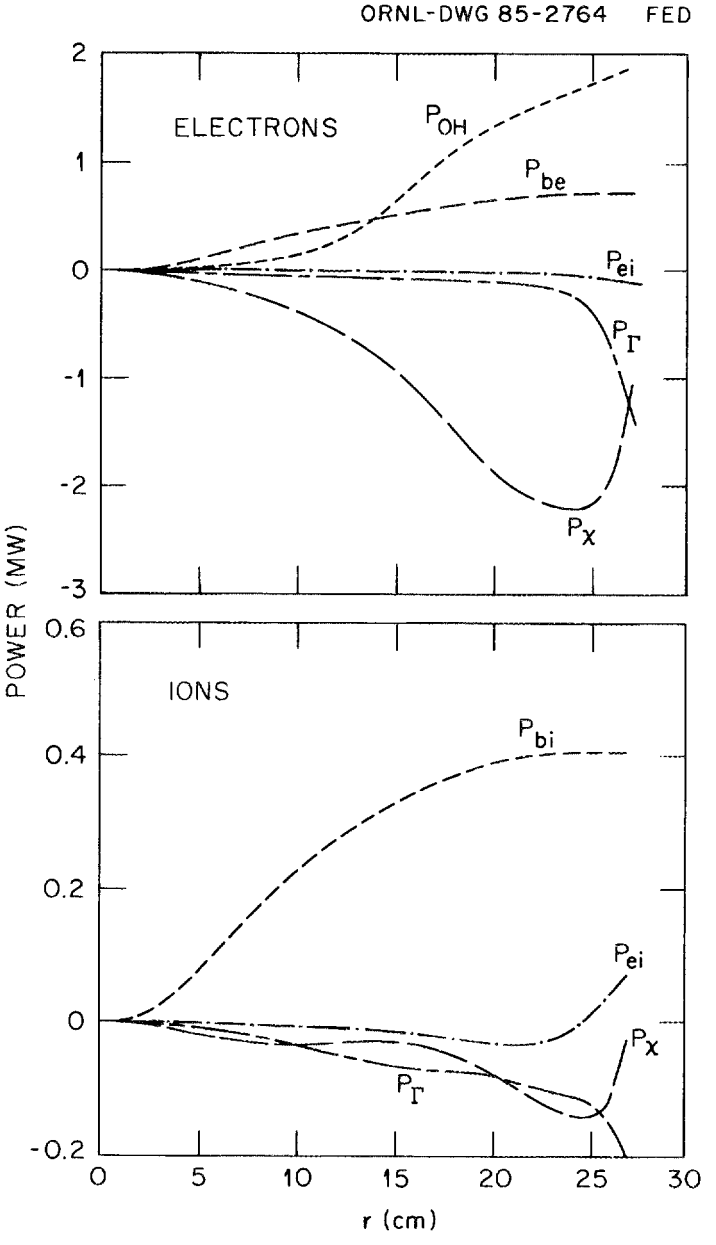

Fig. 2.4.2. Power balance for conditions in column 1 of Table 2.4.2.

Table 2.4.2. Results of transport simulations performed using WHIST

	Case of Fig. 2.4.2	Low-density case	Low-plasma current case	Spitzer resistivity case
β_{tot}, %	13.6	10.8	13.3	10.4
$\beta_{thermal}$, %	12	6	12	
β_p	0.21	0.17	0.45	0.16
P_{be}, MW	0.73	0.56	0.79	0.85
P_{bi}, MW	0.41	0.32	0.45	0.368
P_{OH}, MW	1.87	1.4	0.73	0.804
$<T_e>$, eV	608	792	551	434
T_{e0}, eV	1035	1213	1049	853
T_{ea}, eV	266	481	170	166
$<T_i>$, eV	584	755	572	465
T_{i0}, eV	1054	2153	1046	900
τ_{Ee}, ms	4.5	3.4	7.5	4.8
τ_{Ei}, ms	21	18	23	24
R_0, m	0.45	0.45	0.45	0.45
a_0, m	0.27	0.27	0.27	0.27
κ	2	2	2	2
B_t, T	0.5	0.5	0.5	0.5
I_p, MA	0.9	0.9	0.6	0.9
P_b, MW	1.5	1.5	1.5	1.5
$\bar{n}_e$, 10^{19} m^{-3}	6	3	6.5	6
q_ψ	2.3	2.3	3.6	2.3
Z_{eff}	1.6	1.6	1.6	1.6

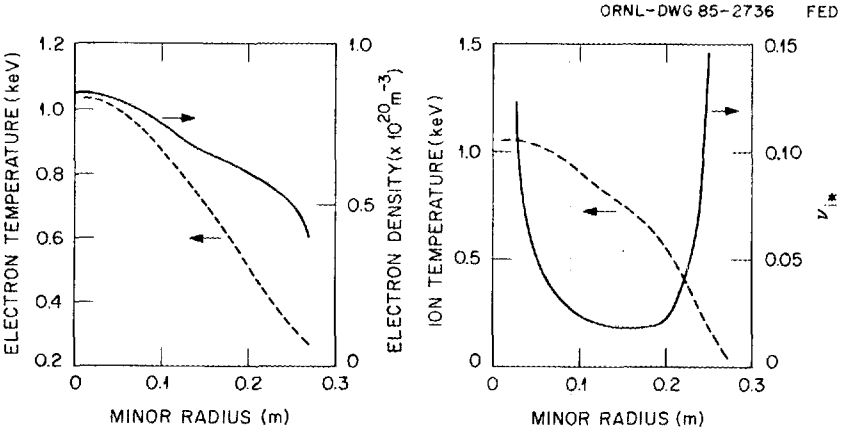

Fig. 2.4.3. Electron temperature, electron density, ion temperature, and ν_* profiles for power balance in Fig. 2.4.2.

The second column of Table 2.4.2 shows a low-density case. Total beta is not greatly reduced, but the thermal component is approximately linear in density.

The third column of Table 2.4.2 is a case at lower plasma current. The electron confinement is improved since we are using

$$\chi_e = 4.5 \times 10^{20} \left[\frac{2\kappa^2}{1 + \kappa^2} \right]^{1/2} \frac{a}{R^2 n_e q_a} ,$$

a version of neo-Alcator scaling with a q dependence. This improvement is reflected in a large reduction in the ohmic heating power P_{OH}, and thus beta is not much changed from the higher current cases. Simulations at higher beam power (2.3 MW) show beta values of 20%.

The correction to plasma resistivity due to trapped electrons is a significant factor in the power balance. In column 4 of Table 2.4.2 the Spitzer resistivity is used. The difference in ohmic heating power between this case and that in column 1 is more than a megawatt.

In summary, the transport simulation assumes neo-Alcator electron heat conduction and neoclassical ions. With these assumptions, STX will achieve beta values of about 12% with a beam power of 1.5 MW. The beam will initially produce this amount of power and can be upgraded to 2.3 MW. The power balance is dominated by the electron channel. A wider view of the STX n, T operating space is shown in Fig. 2.4.4. These WHIST simulations were done at a plasma current of 700 kA.

2.5 OSCILLATING-FIELD CURRENT DRIVE

A current drive scheme based on adding an ac modulation to the toroidal and poloidal magnetic field has been proposed by Bevir and Grey,[11] and a concrete proposal for the ZT-40 device was put forward by Shoenburg et al.[12] This type of current drive has the

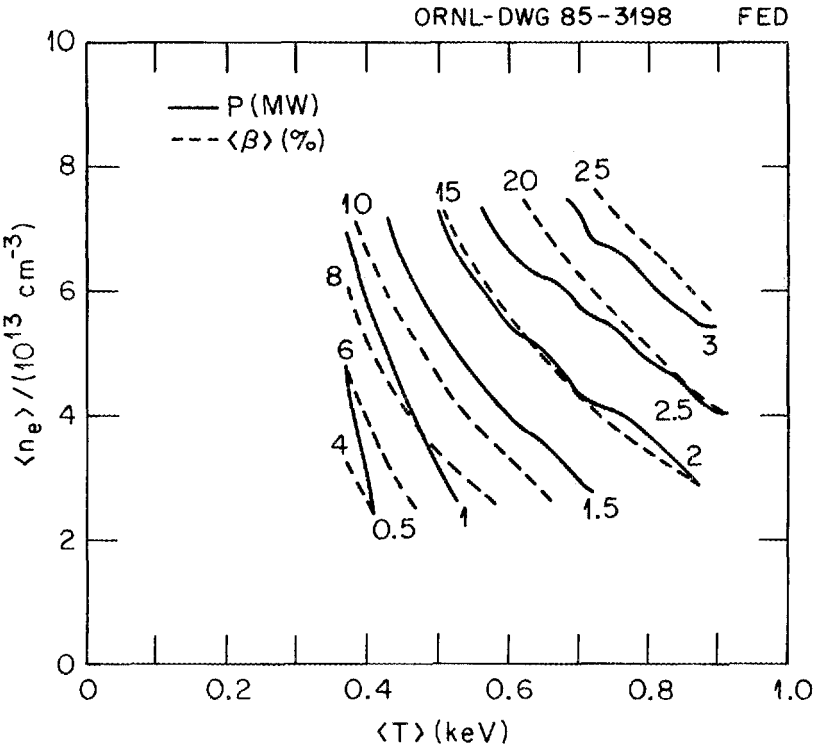

Fig. 2.4.4. $<\beta>$ (dotted lines) and auxiliary power P_a (solid lines) contours in n, T space.

attractive feature of simple technology. Bellam[13] has showed that it can be applied to tokamaks.

The basic idea of the oscillating-field current drive (OFCD) method is to generate in the plasma a time-varying radial velocity and magnetic field such that the time-averaged electric field $\langle \mathbf{U} \times \mathbf{B} \rangle$ is nonzero and is large enough to sustain the toroidal current. Although the ideal is simple, the physics of the problem is quite complicated. One must consider

1. the external driving of the ac components of the magnetic field,
2. the dynamics of the driven perturbations in the plasma,
3. the existence of an anomalous mechanism for the penetration of the current in the plasma, and
4. the consequences of these processes for the plasma confinement.

Complete answers to these issues can only be obtained by the experiment. At present, we can make a few estimates of the external field requirement for such an experiment, and some aspects of the dynamics will be studied in the near future. Here we briefly consider these four problems.

1. To estimate the characteristics of the ac component of the external field, one must consider Faraday's law,

$$\frac{\partial \mathbf{B}}{\partial t} = -\nabla \times \mathbf{E} \ . \tag{2.5.1}$$

If we multiply Eq. (2.5.1) by **B** and integrate over the plasma volume, we have an equation for the evolution of the magnetic energy $W_M = \int dV\, \mathbf{B}^2/2\mu_0$,

$$\frac{dW_M}{dt} + \int dV\, \mathbf{J} \cdot \mathbf{E} = I_\theta V_\theta + I_\phi V_\phi \ ,$$

where I_θ and I_ϕ are the poloidal and toroidal plasma currents and V_θ and V_ϕ are the respective potentials. Because we do not have a direct relation between currents and potentials, this equation is not the most convenient way of posing the problem. We need further information to find out if by oscillating the potentials we can produce a time-averaged net power. Instead of using the energy equation, we can multiply Eq. (2.5.1) by **A**, the vector potential, and integrate over the volume. We obtain an equation for the evolution of the helicity $K = \int dV\, \mathbf{A} \cdot \mathbf{B}$,

$$\frac{dK}{dt} = 2\Phi_T V_\phi - 2 \int dV\, \mathbf{E} \cdot \mathbf{B} \ ,$$

where Φ_T is the toroidal magnetic flux. Taking the time average of this equation and assuming a steady state ($d\langle K\rangle/dt = 0$), we have

$$\langle \Phi_T V_\phi \rangle = \langle \int dV\, \mathbf{E}\cdot\mathbf{B} \rangle \ .$$

With the usual inductive drive for the tokamak, the toroidal magnetic flux $\Phi_T = \Phi_T^{(0)}$ is constant in time, and the toroidal potential $V_\phi = V_\phi^{(0)}$ can also be taken as constant in time. That is,

$$\Phi_T^{(0)} V_\phi^{(0)} = \langle \int dV\, \mathbf{E}\cdot\mathbf{B} \rangle \ .$$

If an ac component is added to the toroidal and poloidal external fields, we can write the corresponding fluxes as

$$\Phi_T = \Phi_T^{(0)} + \Phi_T^{(1)} \sin \omega t \ , \qquad \psi_p = \psi_p^{(0)} + \psi_p^{(1)} \cos \omega t \ ;$$

as a consequence, we have $V_\phi^{(1)} = \omega \psi_p^{(1)} \sin \omega t$. Then $\langle \Phi_T V_\phi \rangle = \Phi_T^{(1)} \psi_p^{(1)}\, (\omega/2)$. To sustain the current, this contribution must be equal to the one that would be produced by the inductive drive, $\Phi_T^{(1)} \psi_p^{(1)} (\omega/2) = \Phi_T^{(0)} V_\phi^{(0)}$. That is,

$$\frac{\Phi_T^{(1)}}{\Phi_T^{(0)}} \frac{\psi_p^{(1)}}{\psi_p^{(0)}} = \frac{2}{\omega} \frac{V_\phi^{(0)}}{\psi_p^{(0)}} \ , \tag{2.5.2}$$

which gives the relative ac amplitudes of the toroidal and poloidal fluxes in terms of the voltage necessary for maintaining the current by the inductive drive, the external poloidal

flux, and the frequency of modulation. Equation (2.5.2) can be rewritten in terms of the fluctuating toroidal voltage as

$$\left[\frac{\Phi_T^{(1)}}{\Phi_T^{(0)}}\right] V_\phi^{(1)} = 2V_\phi^{(0)} \quad . \tag{2.5.3}$$

2. The dynamical evolution of the driven perturbations is a complex problem strongly related to the penetration of the current. Bellam[13] has done a simple calculation to show the plausibility of the current drive scheme. However, full three-dimensional (3-D) nonlinear simulations will be needed to understand the basic mechanisms involved. We plan to do these calculations in the next 12 months.

3. The current penetration must be anomalously fast for this current drive scheme to be effective. This fast penetration can be achieved by exciting double tearing modes[14] in a way similar to the usual tokamak startup. We know that such a mechanism is effective and reasonable. Two points should be made in considering this mechanism. First, it seems logical to have the safety factor at the plasma edge $q_a > 3$ to avoid the dangerous effect of exciting the double tearing mode at the $q = 2$ surface. Second, the frequency ω must be smaller than the growth rate of the double tearing mode γ_T. The most effective range of values for ω must be assessed by numerical simulation.

4. The detrimental effects on confinement are obvious from the proposed mechanism for current penetration. At this point the full consequences cannot be evaluated.

It is clear from this discussion that two parameters, the amplitude of the oscillation and the frequency, must finally be obtained by an optimization that will maintain both the current drive efficiency and good confinement. The numerical calculations will provide an

estimate of the required range of values. However, to minimize the amplitude of the fluctuations, from Eq. (2.5.2) it is clear that ω must be as large as possible. On the other hand,

$$\tau_T^{-1} \ll \omega \lesssim \gamma_T \ , \tag{2.5.4}$$

so we can take $\omega \approx \gamma_T$.

From the WHIST simulations we expect the loop voltage to be about 2 V. Frequencies in the range from 50 to 500 Hz will be appropriate. Thus, the magnitude of the oscillations required will be $\phi_T^{(1)}/\phi_T^{(0)}$, $\psi_P^{(1)}/\psi_P^{(0)}$ in the range from 6 to 14%.

The effects of OFCD are being examined using a transport code to assess the feasibility of this technique. The usual particle and energy balance equations for tokamak radial transport are solved, along with the coupled poloidal and toroidal field diffusion equations:

$$\frac{\partial B_{pol}}{\partial t} = \frac{\partial}{\partial r}\left\{\eta_\parallel\left[\frac{1}{r}\frac{\partial}{\partial r}(rB_{pol}) - j_{source}\right]\right\} \ , \tag{2.5.5}$$

$$\frac{\partial B_{tor}}{\partial t} = \frac{1}{r}\frac{\partial}{\partial r}\left[r\eta_\parallel \frac{\partial B_{tor}}{\partial r}\right] \ . \tag{2.5.6}$$

The poloidal flux modulation is modeled by imposing a specified voltage at the plasma edge,

$$V_{edge}(t) = \bar{V} + \delta V \sin\left[2\pi \frac{t}{\tau} + \delta\right] \ , \tag{2.5.7}$$

and the toroidal flux modulation is modeled by fixing the toroidal field at the plasma edge,

$$B_{\mathrm{tor}}(t) = \bar{B}_{\mathrm{tor}} + \delta B_{\mathrm{tor}} \sin\left[2\pi \frac{t}{\tau}\right] . \tag{2.5.8}$$

A major issue is the nature of $\eta_{\|}$ with the interactive combination of classical resistivity, trapped-particle effects, tearing mode activity, and rippling modes.

An illustration is the ENCORE tokamak, in which $\delta B_{\mathrm{tor}} = 0$ and only loop voltage modulation was performed to test the resistive plasma response. As shown in Fig. 2.5.1, the resistive response of the model is similar to that observed in the ENCORE experiment [Fig. 3(a) of ref. 13].

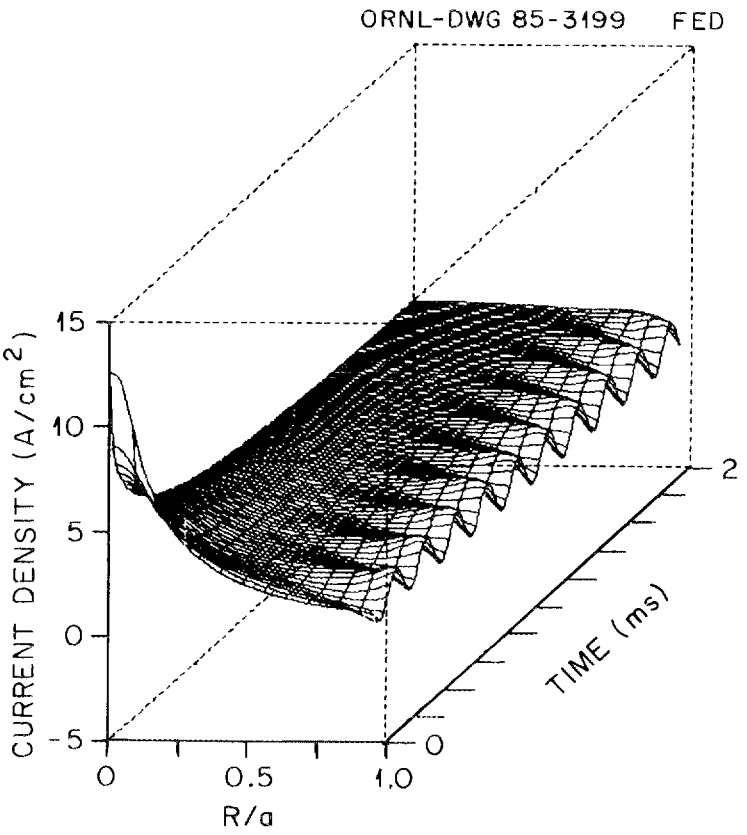

Fig. 2.5.1. Resistive plasma response to poloidal field oscillations.

The STX simulation is shown in Figs. 2.5.2–2.5.4. The value of j_{source} in Eq. (2.5.5) is given by the OFCD model,

$$j_{source} = \frac{V_r B_{pol}}{\eta_\parallel} \quad , \tag{2.5.9}$$

where V_r (the "quiver" velocity) is determined by the toroidal flux modulation.

Figure 2.5.2 shows the B_{tor} variation, with the active region of variation in the low-T_e edge. Figure 2.5.3 shows the time response of the toroidal electric field, and Fig. 2.5.4 shows the I vs V trajectory of the discharge. Here only classical resistivity is used, and thus the additional current remains near the plasma surface. The theoretical efficiency for

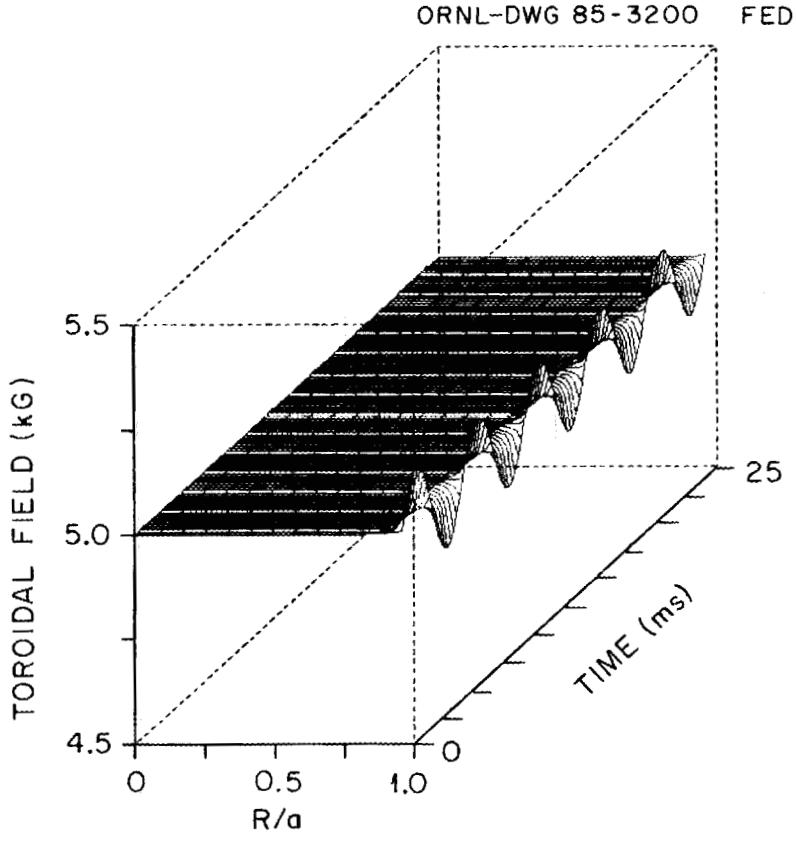

Fig. 2.5.2. Variation of B_{tor}.

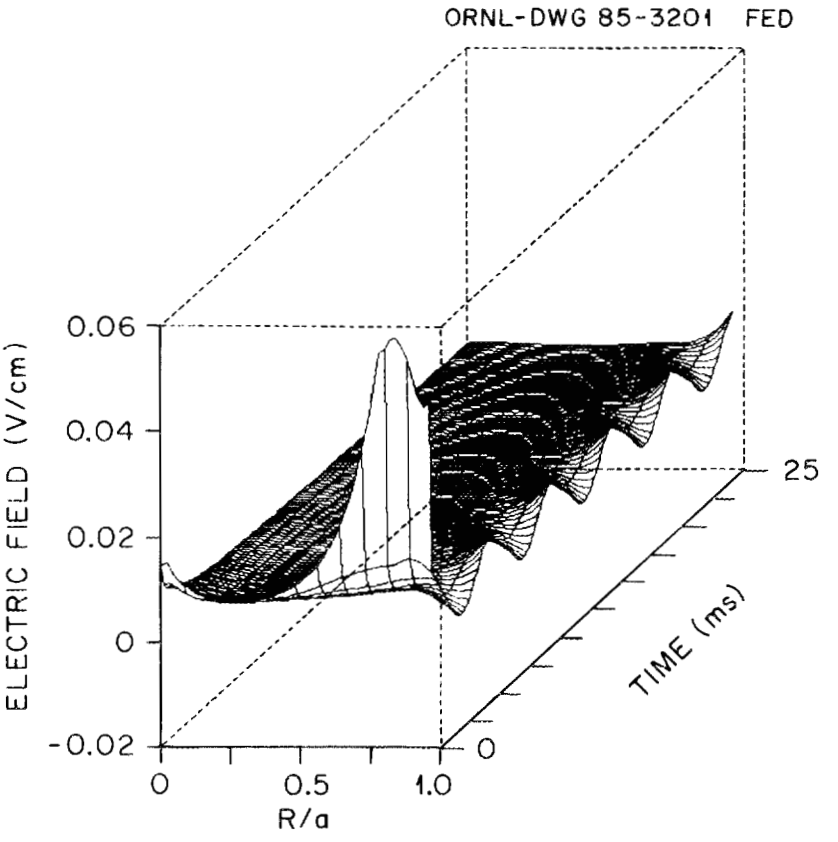

Fig. 2.5.3. Variation of toroidal electric field.

OFCD will depend on the detailed dynamics of both reconnection processes and rippling modes. State-of-the-art coupled, nonlinear, 3-D MHD calculations are needed to determine the expected OFCD efficiency and to provide reliable estimates of the experimental requirements.

2.6 FIELD REVERSAL

The possibility of running STX with the toroidal field reversed offers the opportunity of examining highly elongated, low-aspect-ratio configurations. This represents a new area of parameter space for the reversed-field pinch (RFP). In addition, it will demonstrate RFP operation with beam heating.

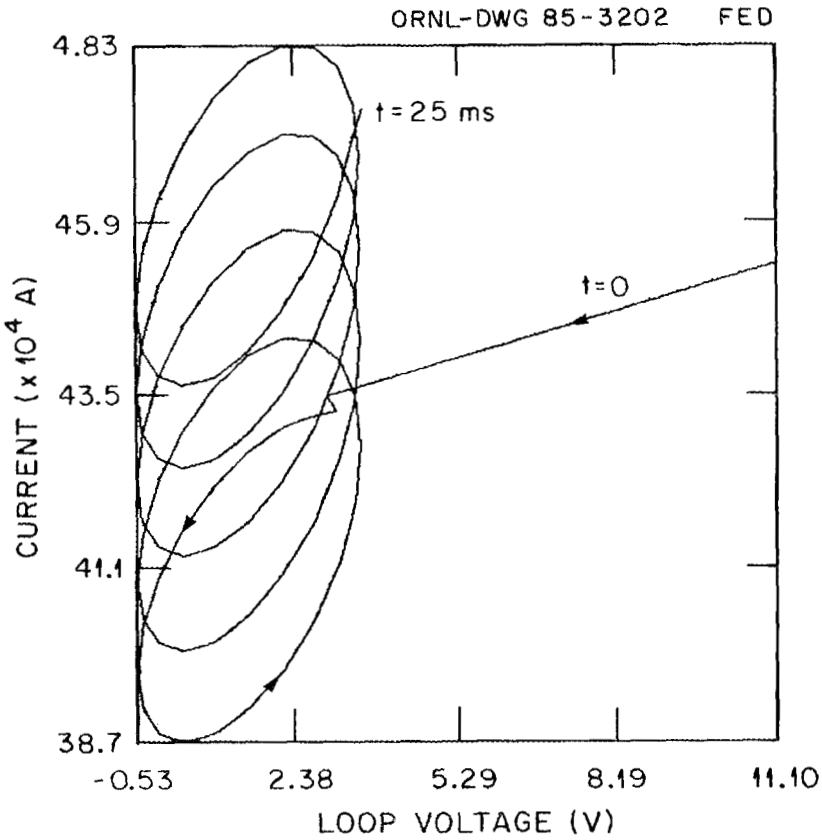

Fig. 2.5.4. I vs V trajectory for oscillatory behavior in Figs. 2.5.2 and 2.5.3.

The constraint that an RFP be at (or near) the minimum energy state means that the q profile scales as the inverse aspect ratio (ϵ). Figure 2.6.1 shows the flux surfaces and q profiles for an aspect ratio of 5 (e.g., ZT-40) and an aspect ratio of 1.5 (elongated RFP; e.g., STX). The change of the q profile with aspect ratio causes the important $m = 1$ rational surfaces to become less densely packed at low aspect ratio. The first few $m = 1$ surfaces are indicated by the arrows in Fig. 2.6.1. Since the $m = 1$ tearing modes are thought to be responsible for the dynamo and to contribute to the electron transport in the RFP, changing the density of the $m = 1$ modes may have interesting consequences and lead to a greater understanding of RFP physics. The effects of aspect ratio and shaping on linear and nonlinear MHD activity in the RFP are currently under investigation.

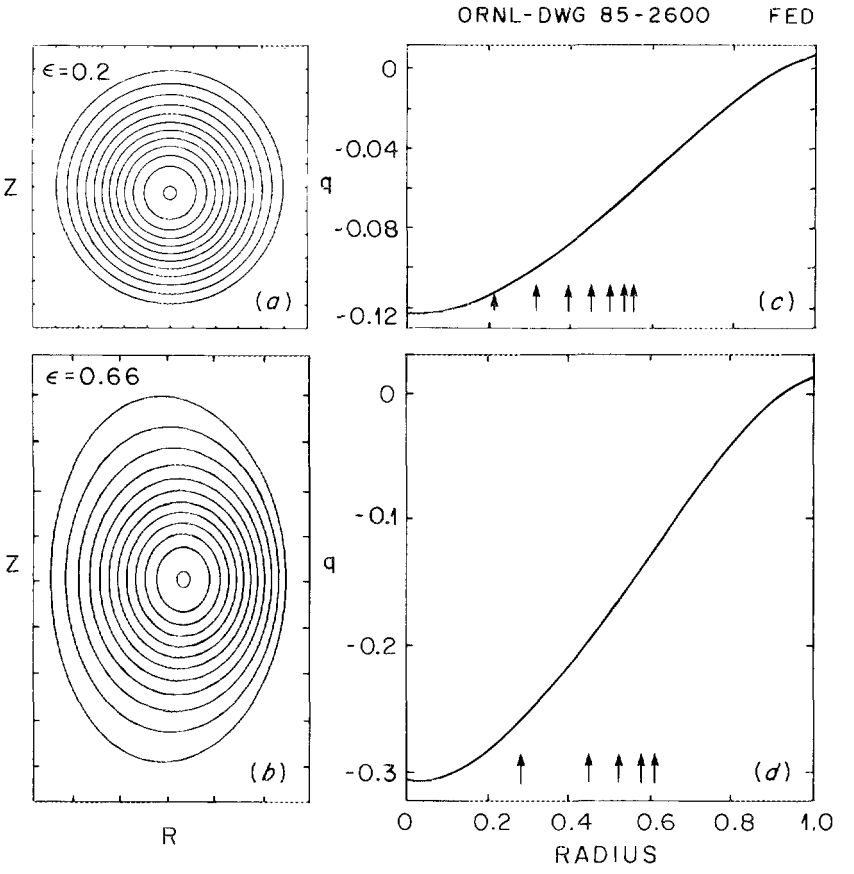

Fig. 2.6.1. Flux surfaces and q profiles for $A = 5$ and 1.5. Arrows indicate the first few $m = 1$ surfaces.

2.7 ORBITS IN STX

Orbit topology in STX differs in some important ways from that in a conventional tokamak.[15] These differences can affect transport, neutral beam injection, and loss regions in STX. We briefly review orbits in a conventional tokamak; then we show how STX is different and what the consequences of these differences will be.

2.7.1 Orbit Topology in Conventional Tokamaks

Ideal tokamaks are axisymmetric, which means that the toroidal angle Φ is an ignorable variable and the toroidal canonical angular momentum P_Φ is conserved. If the

poloidal flux function is ψ, the particle mass is m, the charge is e, and the parallel velocity is $v_\parallel$, then P_Φ is given by

$$P_\Phi = \frac{F}{B} m v_\parallel - e\psi \ . \tag{2.7.1}$$

Here, $F = RB_T$, which is a function of ψ alone.

Because the gyroradius of the particles is small compared to the scale length of the magnetic field, the magnetic moment μ is adiabatically conserved. This, together with conservation of energy E, means that $v_\parallel$ is a function of B and the constants of motion (COMs):

$$v_\parallel = \pm \left[\frac{2}{m} (E - \mu B) \right]^{1/2} \ . \tag{2.7.2}$$

Substituting into Eq. (2.7.1) for P_Φ, we obtain

$$P_\Phi = \pm \frac{F(\psi)}{B} [2m(E - \mu B)]^{1/2} - e\psi \ . \tag{2.7.3}$$

We have explicitly shown the dependence of F on ψ to prove that along the orbit B is a function of both ψ and the COMs.

Equation (2.7.3) is a quadratic equation for B and may be solved as in ref. 15. The equation demonstrates that the appropriate coordinates for tokamak orbits are B and ψ. These coordinates are nonorthogonal but very useful. In Fig. 2.7.1, we show the B and ψ contours for an INTOR-like tokamak at low and high beta. At low beta, the mod-B contours are vertical cylinders because B is proportional to $1/R$. However, at high beta, the diamagnetic plasma digs a well in the magnetic field and a minimum in B forms outside

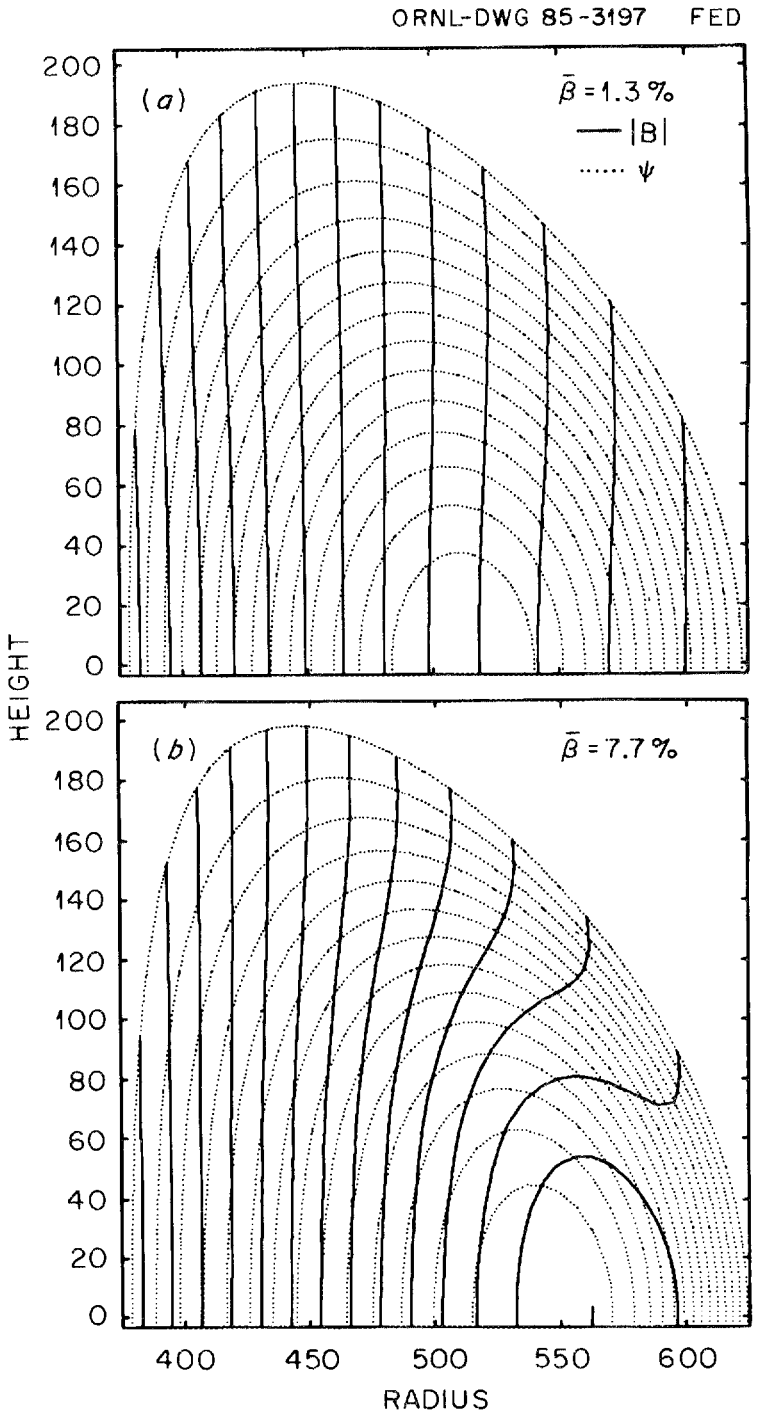

Fig. 2.7.1. B (solid lines) and ψ (dotted lines) contours for INTOR-like tokamak at low and high beta.

the magnetic axis. The essential feature of either case is that on a given flux surface, both B_{max} and B_{min} lie on the equatorial plane.

We exploit this fact to plot the orbits. In Fig. 2.7.2(a), we plot B vs ψ on the equatorial plane for the two beta values. Then we plot Eq. (2.7.3) (the orbits) on the same

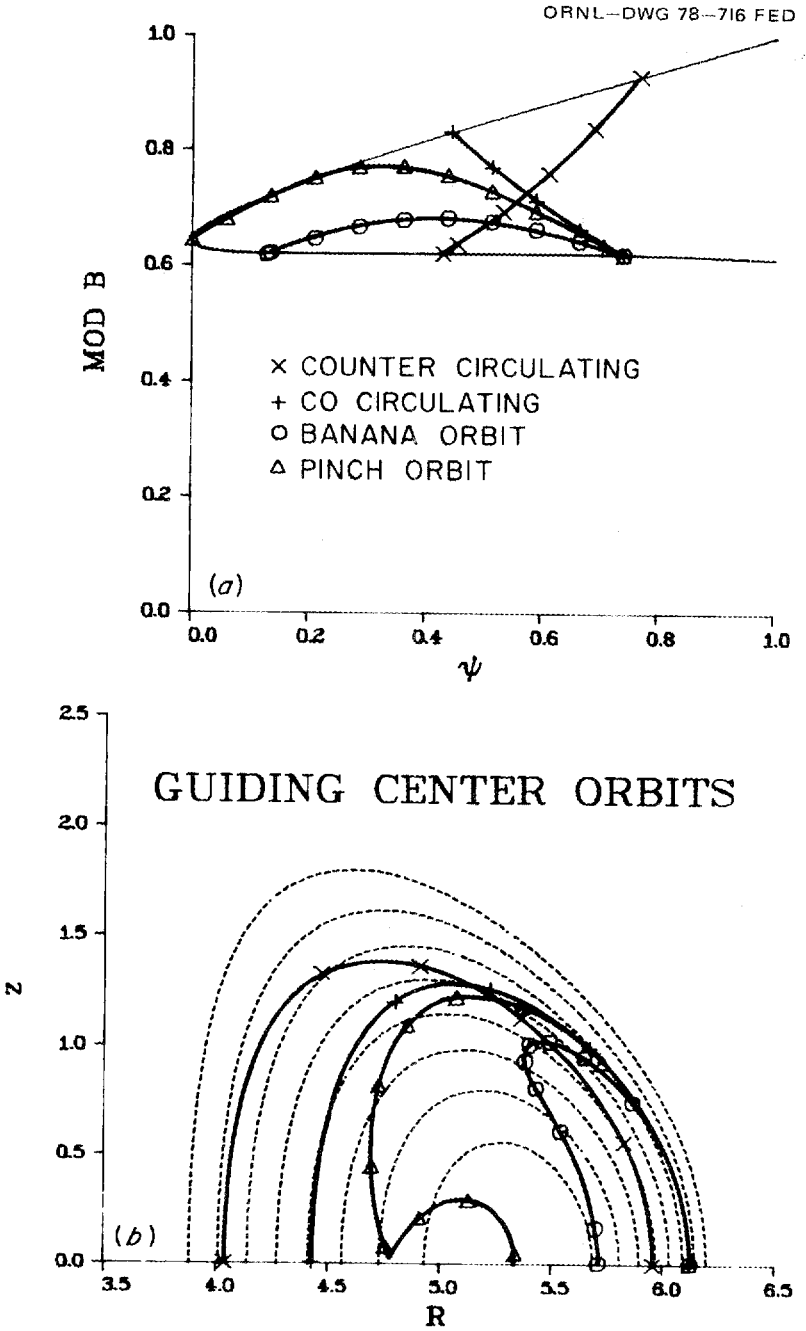

Fig. 2.7.2. B vs ψ on the equatorial plane for low and high beta.

graphs. Because the maxima and minima of B lie on the equatorial plane, the orbits are guaranteed to lie completely within the curve formed by the values of B and ψ on this plane. The different types of orbits are shown in configuration space in Fig. 2.7.2(b). For purposes of illustration, we present the orbits for very energetic particles.

2.7.2 Orbit Topology in STX

STX is still an axisymmetric tokamak, so P_Φ, μ, and E are still conserved and the orbits obey the same equation, Eq. (2.7.3). However, STX has a very low aspect ratio and a very high plasma current, so it is paramagnetic; B is higher in the center of the plasma than it is near the TF coils (due mostly to the high B_p). This causes profound changes in the B contours.

Figure 2.7.3 shows the B and ψ contours for STX with $\beta \simeq 20\%$. On the outer flux surfaces, minima of B occur off the midplane at about the $R = 63$ cm and $Z = \pm 20$ cm

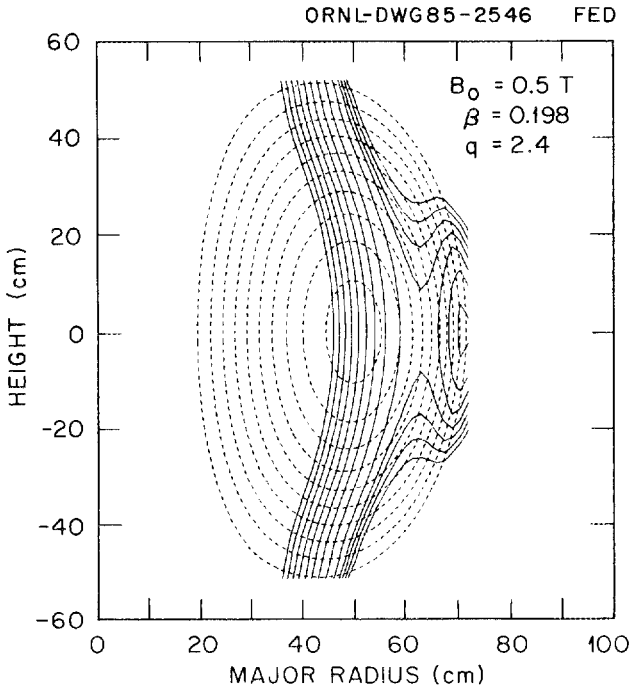

Fig. 2.7.3. |B| and ψ contours in STX.

positions. Particles with small values of $v_\parallel$ can become trapped within these minima. However, in contrast to ripple-trapped particles, these particles are perfectly well confined; they do not $\mathbf{B} \times \nabla\mathbf{B}$ drift out of the machine. Axisymmetry and P_Φ guarantee perfect containment (if no walls exist).

We can also plot the orbits in STX on the B-ψ plane (Fig. 2.7.4). In addition to the B-ψ curves on the equatorial plane, we also require the B-ψ curve that goes out along the minima. Orbits that start on the midplane go downward to the minima and then return upward to complete their orbits.

Figure 2.7.5 shows a collection of 1-keV orbits in STX. The bananas are unusually skinny because the B and ψ contours are almost parallel in the region outside the magnetic axis. This near-omnigeneity significantly lowers the radial step size of these particles. Most of the bananas drift both outward and inward as they traverse their orbit. Thus, the drifts on different parts of the top (or bottom) half of the orbit tend to cancel. One of the off-midplane trapped orbits is also shown.

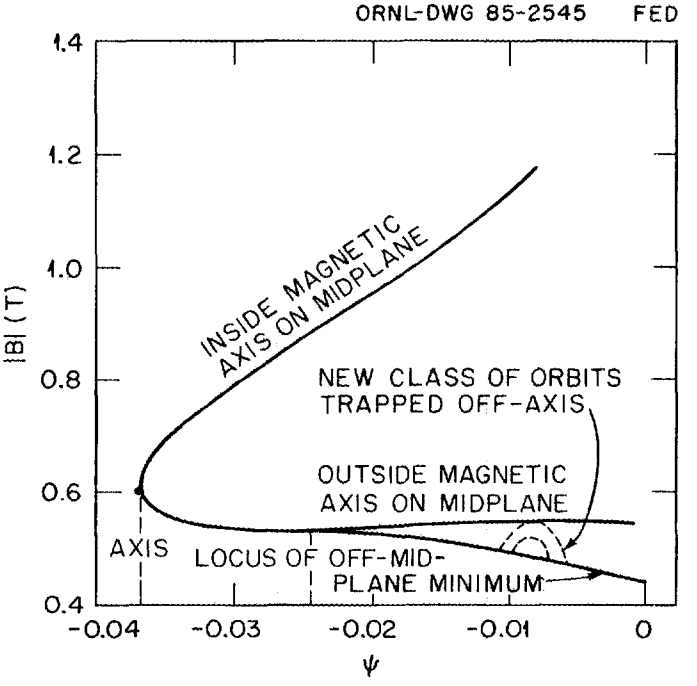

Fig. 2.7.4. New class of orbits in STX on the B-ψ plane.

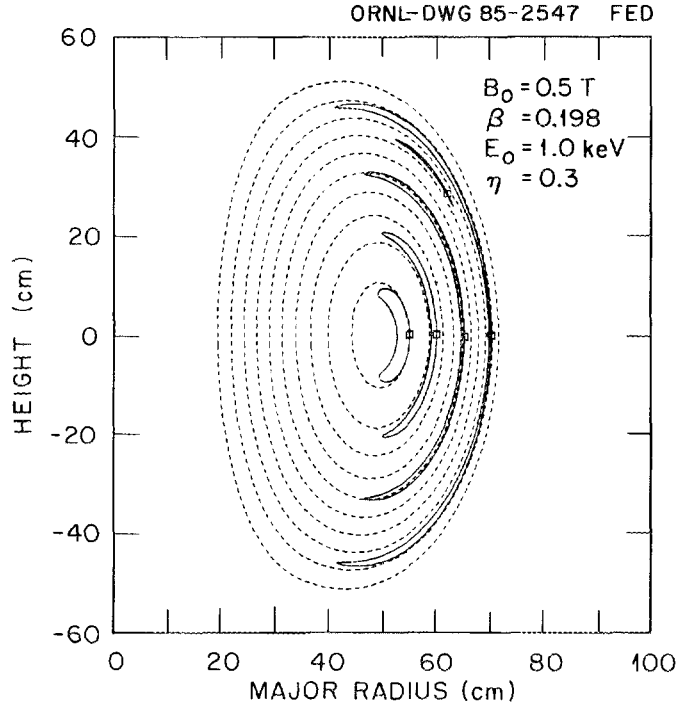

Fig. 2.7.5. 1-keV H^+ orbits in STX.

Due to the low aspect ratio and large elongation of STX, we expect more trapped particles than in a conventional tokamak. Because the analytic formulas are suspect in this parameter range, we started 1000 protons, randomly distributed in pitch angle, on a flux surface that is halfway out in ψ, or equivalently at $r/a \sim 1/4$. The orbits were followed for a complete poloidal transit to determine if each orbit was trapped, circulating, or lost. At 1 keV, 43% of the particles are trapped and none are lost. For 50-keV particles, 42% are trapped and 4% are lost. Even though the fraction of trapped particles is large, we do not expect large increases in transport because of the small banana widths. These trapped-particle fractions agree closely with those used in Fig. 2.4.1.

To properly evaluate transport in STX, we have run the ORNL Monte Carlo transport code to evaluate the diffusion coefficients. Indications are that the neoclassical transport is reduced by about a factor of 2 compared with a tokamak that has $A = 2.5$ for the same q and B_0.

2.8 EXPERIMENTAL APPROACH

The experimental program will be designed to address the issues discussed in this chapter. Broadly speaking, we expect a program with four distinct phases: ohmic confinement, beta investigations, oscillating-field current drive, and nontokamak configurations. While these phases will overlap, the emphasis would be likely to evolve in the order indicated.

The first several months would be a period of shakedown and bringing up diagnostics. Plasma control will be somewhat more critical in STX than in most tokamaks. First, the closeness of the plasma to the inner wall imposes a requirement for radial position control to an accuracy of about 1% of the major radius. Second, dq/dR is quite large in the spherical torus. In STX dq/dR is about 0.22 per centimeter; thus, a few centimeters of outward excursion could drop the edge q by 1. Feedback optimization will be one of the early tasks in the experiment.

Another task will be the optimization of startup, including the shunting circuit across the OH solenoid. During this period primary operating diagnostics will be checked out. These include magnetic sensors for plasma control, a 1-mm interferometer, radiometers, flux loops, Rogowski coils, shunts, etc. The data acquistion system that operated on ISX-B will be used on STX. The VAX data acquisition computers used for ATF will also service STX (although both devices could not be pulsed at the same instant of time).

While STX is in many ways like a conventional tokamak, there are some differences. One would hope to rely primarily on magnetic diagnostics for beta investigations; however, a distinguishing characteristic of the spherical torus is that poloidal beta will be small and beta measurements may of necessity require Thomson scattering profile measurements. This diagnostic will need to be installed early in the experimental program. We envision this to be as simple as possible—namely, a single-point radially scanning system.

The initial experiments will characterize the ohmic plasma and will primarily explore confinement and impurity properties. An important goal in this phase is the establishment of good target plasmas for neutral beam heating.

Neutral heating will be available from the beginning of the experimental program. Heating experiments will begin as soon as good target plasmas are available. The experiments will be divided into two basic segments: without and then with the divertor. The division is enforced by the need for an additional power supply for the divertor and will to some extent depend on experimental results. It is possible that the divertor will be crucial to the high-beta program, since the high plasma current equilibrium requires a fairly high edge temperature. It is anticipated that the substation improvements required for 900-kA plasmas would be implemented when the divertor power supply is installed.

Based on ISX-B experience a large fraction of the high-beta experiments will involve plasma optimization. The efficiency of this process is greatly enhanced by the use of diamagnetic and poloidal field measurements from which we can infer plasma pressure. These diagnostics will have a high priority in the early phases of the experiment.

It is desirable to have a profile measurement of ion temperature based on Doppler broadening measurements of impurity atoms. This would allow ion thermal diffusivity to be measured. We also expect to have PIN arrays and arrays of Mirnov coils to study MHD fluctuations.

The experimental analysis of confinement and beta will primarily use the codes ZOR-NOC and MAGDAT, which were used on ISX-B. The long-standing and productive tradition of close cooperation between the theory and experimental groups at ORNL in the analysis and interpretation of the experimental data would continue.

At present a significant theoretical effort is under way in oscillating-field current drive. We cannot as yet provide details of the experimental program. There will clearly be a period between the beta and current drive experiments while the ac power supplies are

installed. New magnetic diagnostics will have to be developed for these experiments. As yet, the optimal approach is unclear. Issues to be resolved are the frequency of oscillation, the relative amplitudes of toroidal and poloidal oscillation, and the nature of the poloidal oscillation—which could either be the OH solenoid flux or the plasma elongation.

Work on nontokamak configurations would most likely be the final phase of the STX program.

REFERENCES FOR CHAP. 2

1. S. P. Hirshman and G. H. Neilson, Oak Ridge National Laboratory, unpublished data, May 1985 (submitted to *Phys. Fluids*).

2. F. Troyon et al., *Plasma Phys. Controlled Fusion* **26**, 209 (1984).

3. O. B. Pogutse et al., *Sov. J. Plasma Phys.* **6**, 341 (1980).

4. R. Gruber et al., *Comput. Phys. Commun.* **21**, 323 (1981).

5. B. V. Waddell, B. A. Carreras, H. R. Hicks, and J. A. Holmes, *Phys. Fluids* **22**, 896 (1979); B. A. Carreras, M. N. Rosenbluth, and H. R. Hicks, *Phys. Rev. Lett.* **46**, 1131 (1981); P. H. Diamond et al., *Phys. Fluids* **27**, 1449 (1984).

6. L. A. Charlton et al., *J. Comput. Phys.*, to be published.

7. B. A. Carreras et al., *Nucl. Fusion* **21**, 511 (1981).

8. R. Goldston, *Plasma Phys. Controlled Fusion* **26**(1A), 87 (1984).

9. S. P. Hirshman et al., *Phys. Fluids* **22**, 731 (1979).

10. W. A. Houlberg, S. E. Attenberger, and L. L. Lao, *Computational Methods in Tokamak Transport*, ORNL/TM-8193, Oak Ridge Natl. Lab., 1982.

11. M. K. Bevir and J. W. Gray, p. 176 in *Proceedings of the Reverse Field Pinch Theory Workshop*, LA-8966-C, Los Alamos Scientific Laboratory, Los Alamos, N.M., 1981.

12. K. F. Schoenberg, R. F. Gribble, and D. A. Baker, *J. Appl. Phys.* **56**, 2519 (1984).

13. P. M. Bellam, *Phys. Rev. Lett.* **54**, 1381 (1985).

14. B. A. Carreras, H. R. Hicks, and B. V. Waddell, *Nucl. Fusion* **19**, 583 (1979).

15. J. A. Rome and Y-K. M. Peng, *Nucl. Fusion* **19**, 1193 (1979).

3. STX DESIGN, COST, AND SCHEDULE

An engineering feasibility study was carried out for the STX device to identify major feasibility issues and to define an engineering approach in enough detail that a preliminary projection of the cost and schedule could be made. The main conclusion was that it does appear feasible to construct such a device at a reasonable cost (approximately $6 million) using conventional fabrication processes.

High cost-impact areas have been identified, and further cost reductions are possible. The design approaches and assembly plans for the major components are given in this chapter, along with the estimated cost and schedule. This study forms a basis from which to proceed with a conceptual design that focuses on the higher-risk areas and the areas identified as cost sensitive.

3.1 MAGNET SYSTEM

The baseline magnet system can be divided into three main groups: (1) the magnetizing coil (ohmic heating) system, (2) the poloidal coil system, and (3) the toroidal magnet system. Figure 3.1.1 is a cross section showing all the windings. Following an overview in Sect. 3.1.1, the principal design and fabrication considerations for each group are given. The external support structure is discussed in Sect. 3.2.

3.1.1 Overview

By its nature, a low-aspect-ratio tokamak requires a high-energy-density solenoid. The principal feature of the STX ohmic heating (OH) system is the high-performance central solenoid. The detailed analysis of this solenoid is presented in Sect. 3.1.2. The return windings, which constitute the remainder of the OH system, are a compromise between excluding the OH flux from the plasma volume and allowing reasonable diagnostic access. The

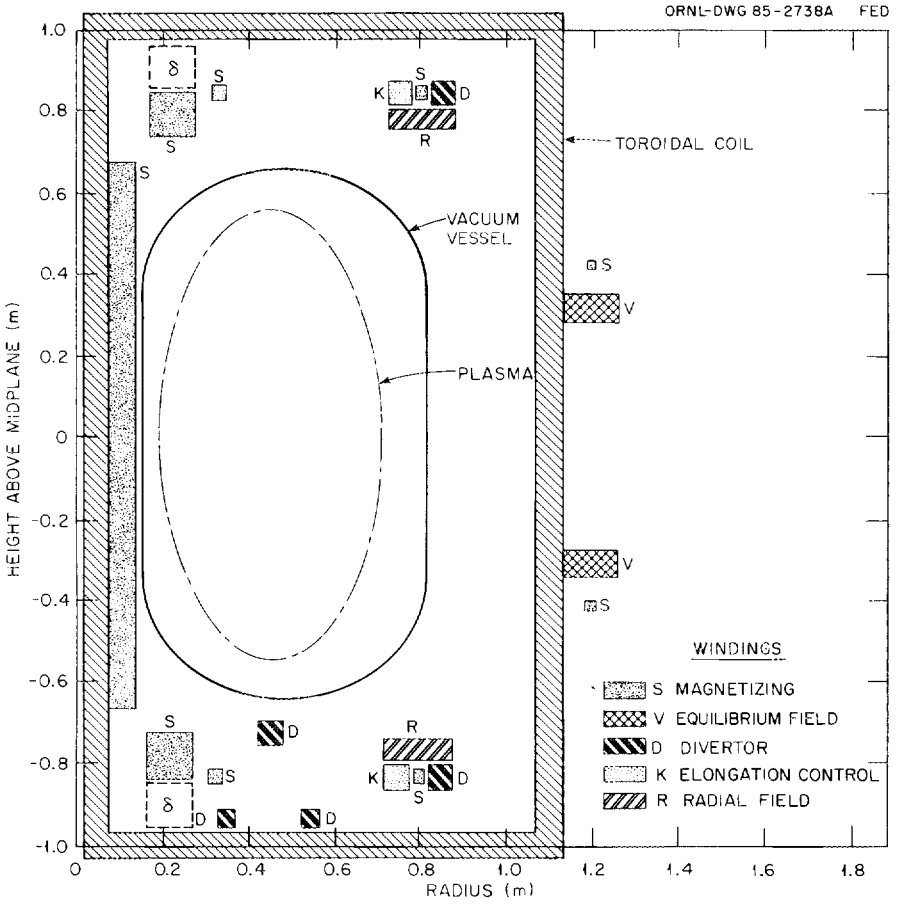

Fig. 3.1.1. STX magnet system.

system shown in Fig. 3.1.1 is sufficient, as shown by the small plasma shape variation through the flux swing (Fig. 3.1.2), and allows access for a Thomson scattering system viewing the plasma from the major radius to the outer edge of the plasma. The field pattern at startup is shown in Fig. 3.1.3 with the null positioned near the major radius. If electron cyclotron heating (ECH) is used to assist startup, the null can be moved to the resonance location.

The poloidal coil system consists of coil sets to provide the equilibrium field, shape control, and an expanded-boundary divertor. The flux pattern with the divertor activated is shown in Fig. 3.1.4. The separatrix motion through the flux swing is less than 1 cm in radius and less than 2 cm vertically. Baffle plates will be located to prevent recycling of the working gas from the divertor region.

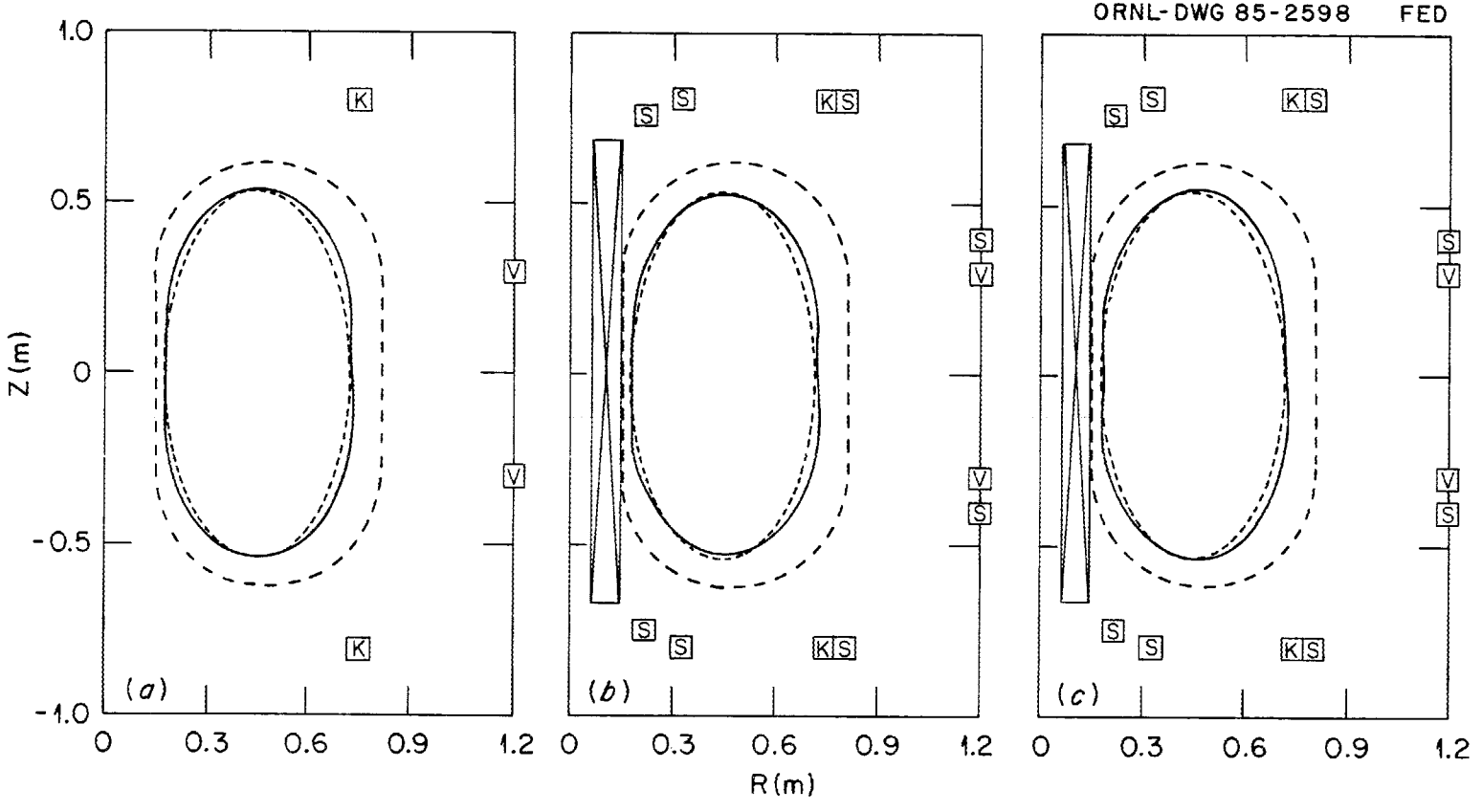

Fig. 3.1.2. Variation in plasma shape through the flux swing. (a) Center of flux swing, $I_s = 0$; (b) start of flux swing, $I_s = 23$ kA; (c) end of flux swing, $I_s = -23$ kA. Plasma current, pressure, vertical field, and shaping field all held constant. Outer dashed line: vacuum vessel. Inner dashed line: desired plasma shape. Solid line: calculated plasma shape. (The slight pinching on the outside midplane is an artifact resulting from the use of six filaments to model the plasma current distribution.)

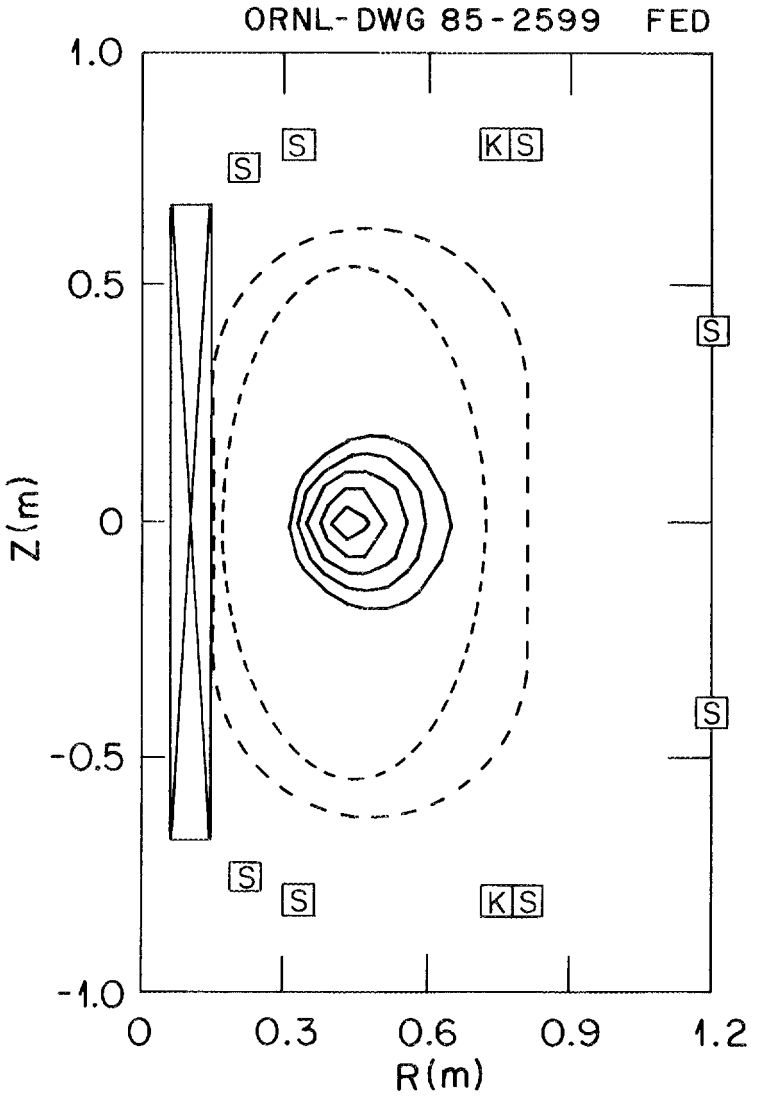

Fig. 3.1.3. Field pattern at startup. Null is near the major radius.

The divertor has been included in STX for a number of reasons. First, although we expect very high plasma currents, the axial current density is still limited by $q \geq 1$ to the value $2B_t/\mu_0 R$. The increase in current is entirely a profile effect. Thus, the ability to produce a broad current channel is essential. The divertor is a means to segregate the atomic physics zone from the current channel and to allow the high-temperature region to extend over the plasma radius (see Table 2.4.1). Second, the design of a device with very low aspect ratio truly places a premium on the space at the inboard side of the plasma column.

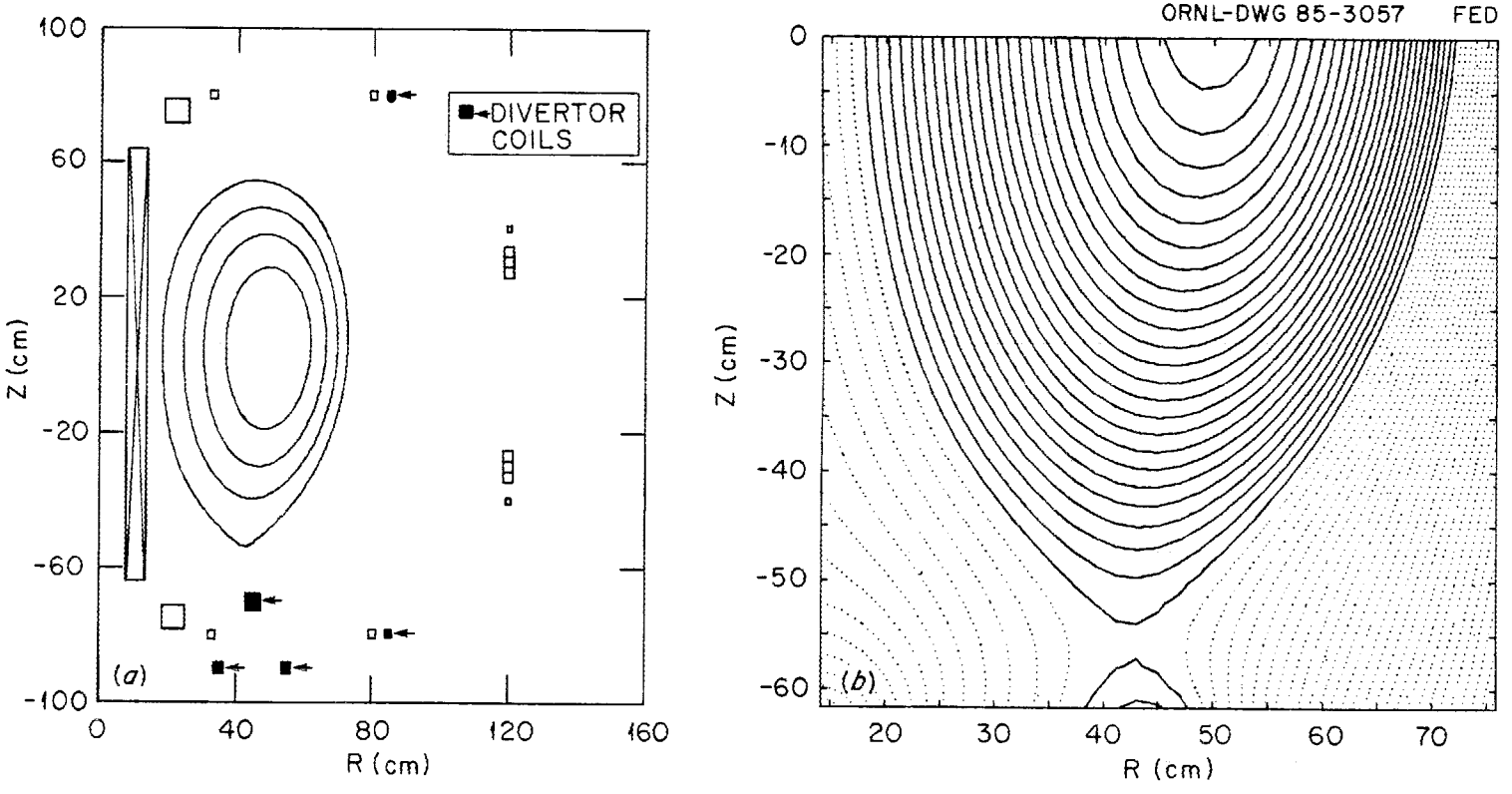

Fig. 3.1.4. Flux pattern with divertor activated.

We have allowed only 3 cm from the plasma to the inner wall of the vacuum vessel. If this is too little space and the impurity generation is severe, a divertor will allow us to reduce the temperature of the plasma contacting the inner wall. Finally, only tokamaks with divertors have been able to operate with both neutral beam heating and good energy confinement (i.e., with $\tau_E \approx \tau_E^{OH}$).

The vertical position control system in STX will be designed to satisfy two requirements: (1) to keep the plasma vertically centered (or at some other prescribed position) within ± 1 cm, and (2) to stabilize the axisymmetric vertical instability. The first requirement is necessary to control the minor radius for operation with a top-rail limiter. It is also critical in divertor operation to control the position of the X-point. The second requirement is common to all vertically elongated tokamaks, including ISX-B, in which the equilibrium field index is negative. Stabilization will be accomplished in the usual manner, through a combination of passive and feedback-driven active conductors.

An advantage of the low-aspect-ratio configuration is that it is naturally elongated. That is, a perfectly vertical equilibrium field produces an elongation κ greater than 1.5, and only a small field gradient is required to increase κ to the design value of 2.0. Since it is the field gradient, and not the elongation per se, that causes the vertical instability, the problem in STX at $\kappa = 2$ is no worse than in ISX-B at $\kappa = 1.4$. (In fact, STX would be stable at $\kappa = 1.5$).

A prerequisite for feedback stabilization of the vertical instability with realizable power supplies is the existence of enough passive stabilization to slow the vertical instability's growth rate from an Alfvén to an L/R time scale. The resistive vacuum vessel used in STX is inadequate for this purpose because its time constant is too short (<1 ms). Therefore, a set of aluminum or copper conductors will be installed outside the vacuum vessel, as illustrated in Fig. 3.1.5. At a toroidal break, the top and bottom conductors will be connected in series with each other and with opposite polarity, so that they enclose no

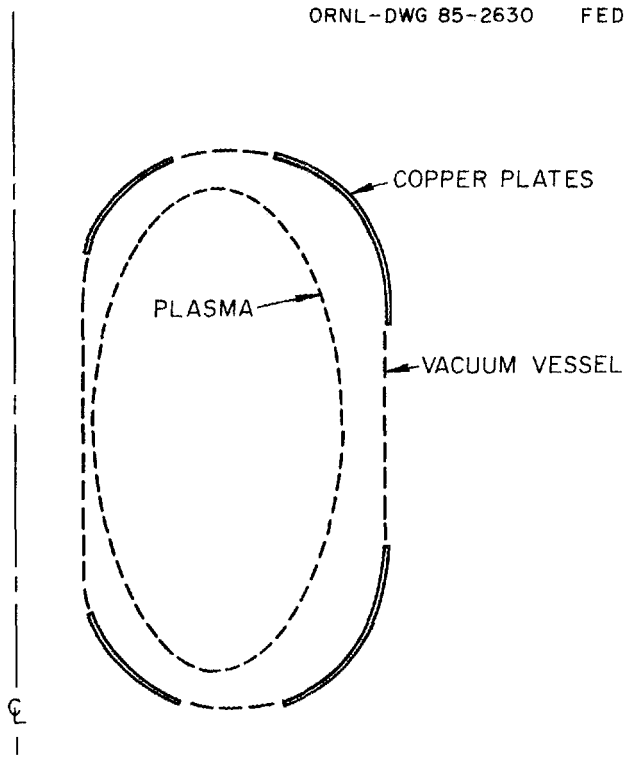

Fig. 3.1.5. Plates outside the vacuum vessel for vertical stabilization.

net OH flux. With such passive stabilizers, a filamentary plasma model gives the following expression for the growth rate of the vertical instability:

$$\gamma = (\tau_g)^{-1} = (\tau_s)^{-1} \frac{-m}{m_c + m} \quad . \tag{3.1.1}$$

The gradient in the equilibrium field, B'_R, is normalized in terms of the modified field index, $m = 2\pi R_0^2 B'_R/\mu_0 I_p$. The largest value of $|m|$ that can be stabilized is the "critical" index m_c, a geometrical constant of the passive conductors. The L/R decay time of the passive conductors is τ_s. From MHD equilibrium calculations, we determine that $m = -0.12$ for $\kappa \simeq 2$ (with some dependence on the current profile). For the passive plates illustrated in Fig. 3.1.5, $m_c = 0.20$ and, assuming 0.5-in.-thick aluminum, $\tau_s = 80$ ms.

Substituting these parameters into Eq. (3.1.1) yields a passively stabilized growth time τ_g of about 50 ms.

Active control of the vertical position will be accomplished using a pair of radial field (RF) coils (shown in Fig. 3.1.1) powered by the four-quadrant, ±3-kA, ±72-V transistor power supply used on ISX-B. The maximum ampere-turns in each RF coil were determined by requiring a ±10-cm dynamic range in plasma position. This implies that the windings must provide a range of radial fields B_R of $\pm B_{max} = 100$ G on axis, which in turn requires ±42 kA-turns in each coil. Fourteen turns per coil will match this requirement to the existing supply.

The voltage required for stabilization depends on the character of the "noise," or stray radial fields, driving vertical displacements. We have used a nonlinear model of the feedback control loop to simulate the response to a step in stray radial field ΔB_R of 50 G, which corresponds to a ~5-cm vertical shift. Using $\tau_g = 50$ ms, letting the power supply voltage and current be clipped at $\pm V_{max}$ and $\pm I_{max}$, respectively, and accounting for the delayed radial field penetration due to the passive stabilizers, we find that stable operation is conservatively obtained with $V_{max} \times I_{max} = 200$ kW. This quantity scales as $B_{max}\Delta B_R/\tau_g$, indicating the dependence on the previous assumptions. Since the ISX-B supply has $V_{max} \times I_{max} = 216$ kW, it is compatible with STX requirements.

3.1.2 Magnetizing Coil System

3.1.2.1 Central OH solenoid

Configuration: Table 3.1.1 gives the baseline configuration for the central OH solenoid. The proposed design has a central field of 10.2 T with an inside radius to the insulation of 7.9 cm, an outside radius of 14.2 cm, and a length of 129 cm. The current was limited to 23.5 kA so that existing SCR power supply components can be used. To

Table 3.1.1. Central OH solenoid

Inside radius, cm	7.9
Outside radius, cm	14.2
Length, cm	129
Current, kA	23.5
Number of turns	448
Number of axial layers	112
Conductor radial height, cm	1.45
Conductor width, cm	1.05
Layer-to-layer insulation thickness, cm	0.1
Turn-to-turn insulation thickness, cm	0.1
Cooling tube inside diameter, cm	0.635
Current density, kA/cm^2	19.4
Space factor λ	0.677
Resistance, Ω (at 20°C)	0.056
Inductance, H	0.006
Central field, T	10.2
Flux swing, V·s	0.76
Material	CDA 182 copper
Peak hoop stress, MPa (ksi)	134 (19.5)
Adiabatic temperature rise, K	82

obtain adequate cooling for a 3-min repetition rate, the coil will be wound 4-in-hand with 4 radial layers, giving 16 parallel flow passages.

The use of multiple-in-hand windings will also allow construction without joints in the interior of the coil. All flow connections and electrical jumpering will be done at the ends. A possible configuration is shown in Fig. 3.1.6. The positive and negative leads both enter and exit at the top. All other turns are connected by soldered joints to copper blocks. All connecting turns have the opposite helical pitch so that they support each others' hoop forces. After winding, the ends will be sealed in a thick epoxy layer to restrain the jumper blocks from twisting, and the entire coil will be vacuum-impregnated with epoxy.

Structural analysis: The stresses due to magnetic loads in the central region of the coil were calculated using the STANSOL program and the ANSYS finite-element code for a 1.43- by 1.43-cm hollow conductor. The STANSOL results are shown in Fig. 3.1.7, where the peak hoop stress is 16.3 ksi on the inside radius. In this model, the conductor hole is accounted for by lowering the current density so that the current per conductor is correct.

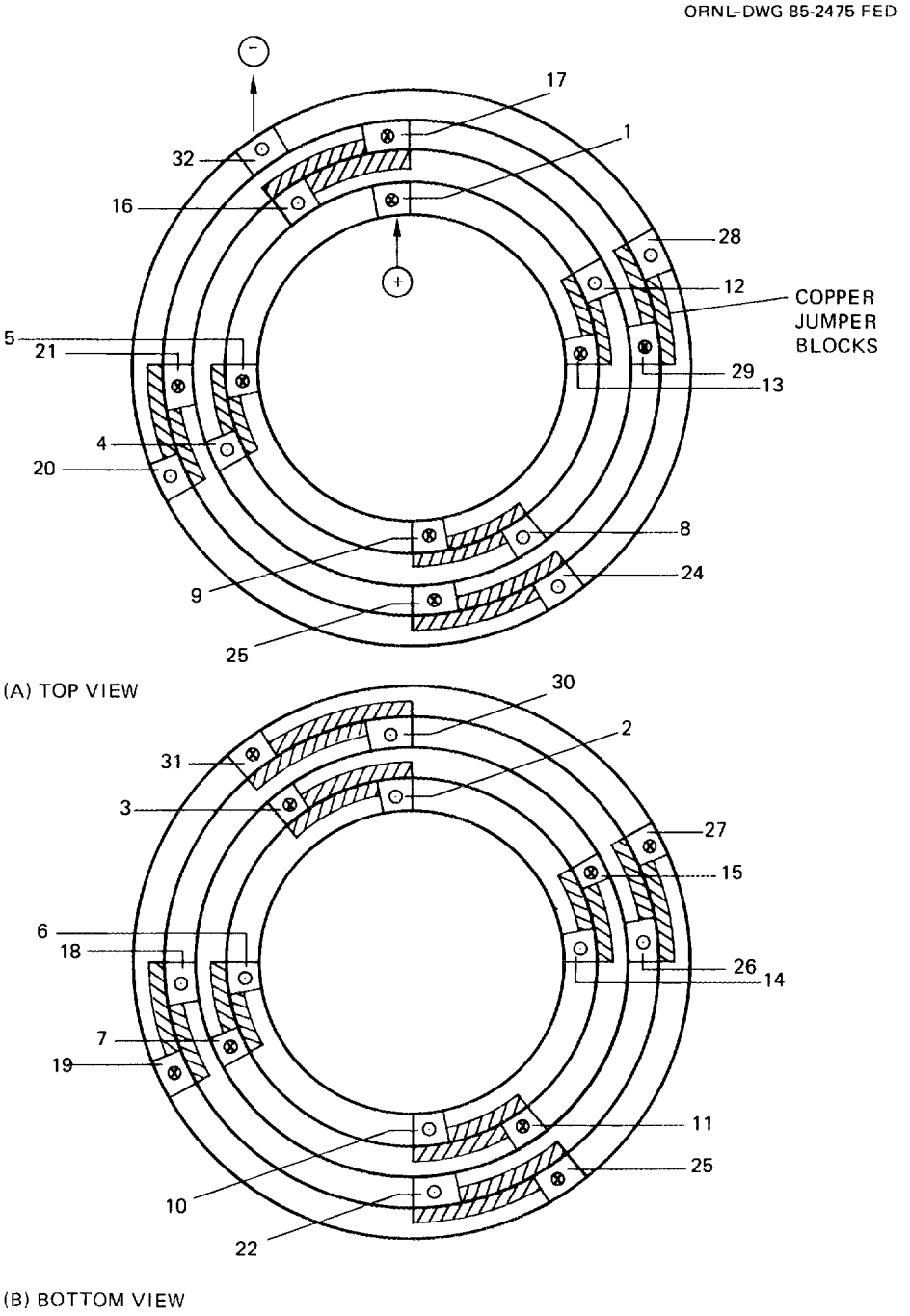

Fig. 3.1.6. OH coil top and bottom views, showing electrical connections for a four-in-hand winding. Numbers indicate sequence of electrical connections.

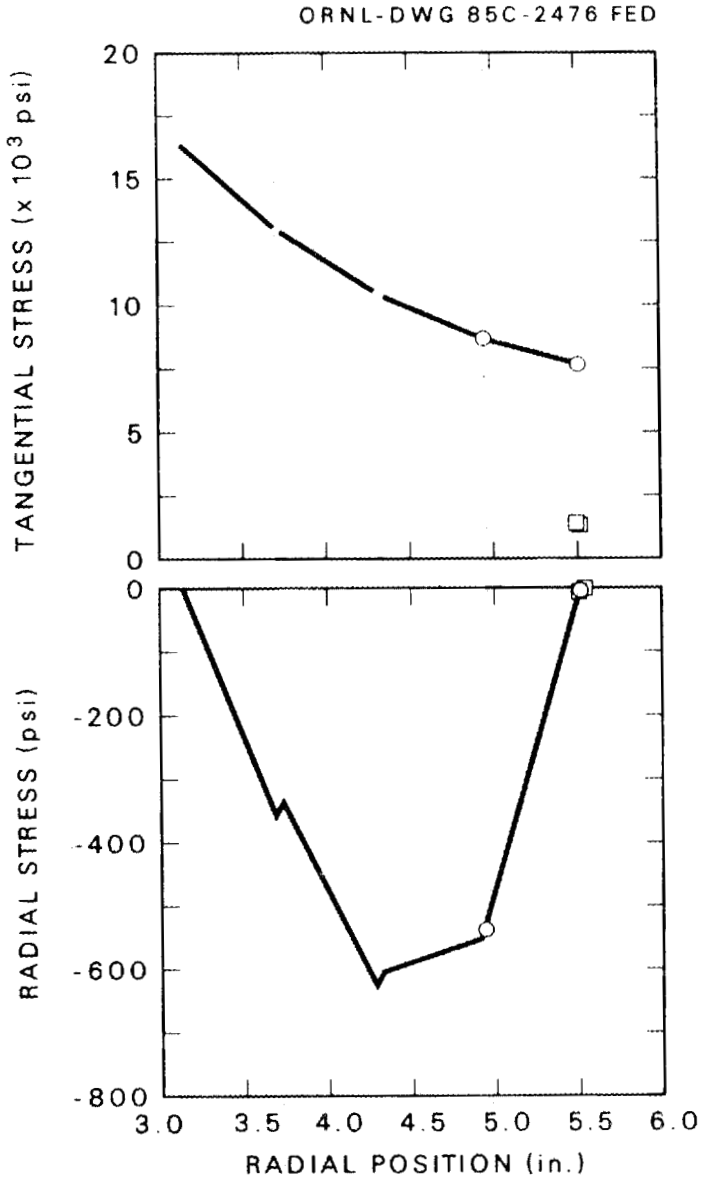

Fig. 3.1.7. OH coil STANSOL stress analysis for a solid conductor with epoxy insulation.

The stresses must then be increased by the ratio of the conductor and hole area divided by the conductor area. This correction gives 19.3 ksi for the peak tensile stress on the inside.

The ANSYS model for the same conductor is shown in Fig. 3.1.8. This is a model of 4 radial turns with the magnetic load per conductor distributed as line loads (lb/rad) on

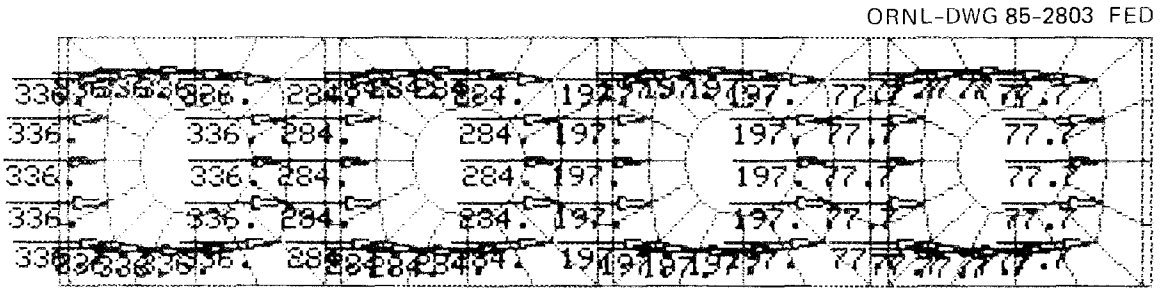

Fig. 3.1.8. ANSYS axisymmetric load model of four radial OH coil turns.

the 16 nodes around each hole. The calculated peak stress in the copper is 18.7 ksi, which is in good agreement with the STANSOL calculations and also agrees very well with a simple JBR approximation of the inner hoop stress (19.5 ksi).

Fatigue analysis: The design criteria for the machine require 20,000 machine cycles, which is equivalent to 40,000 stress cycles for the OH coil. A fatigue life estimate based on elastically calculated stress was done for annealed and half-hard OFHC copper and for CD-182 chrome copper. A stress concentration factor K_t was also included to estimate the effects of end joints and fittings, although actual design concentration factors were not available. The results are given in Table 3.1.2, and the methodology is described in Appendix D. Annealed OFHC copper is not adequate, and half-hard OFHC copper is marginal with no concentration factors. CD 182 is acceptable with concentration factors of at least 2. Full-hard OFHC was not considered, since it would not have adequate ductility to wind on the inner layer, where the winding strain is 0.08.

Thermal analysis: With 16 flow passages, the average coolant channel length is 19 m. For reasonable pressure drops and water flow rates, the time constant for heat transport through the cross section of a turn will be small compared to the transit time of the water from inlet to exit. To estimate the temperature rise and cooldown rates, a thermal model of the coil was made in which the temperature was assumed to be a function of the axial length and time only. A triangular sawtooth current waveform was assumed in which the current ramps to its maximum in 0.25 s, goes through zero and to the negative maximum

Table 3.1.2. Fatigue design life summary

Stress	Fatigue design life, cycles[a]		
	Fully annealed OFHC Cu	Half-hard OFHC Cu	CD-182 Cu alloy
1. 0 to 20 ksi nominal in conductor	11,000	35,000	10^7
2. 0 to 20 ksi, $K_t = 2$[b]	4,800	8,600	10^7
3. 0 to 20 ksi, $K_t = 4$	1,300	1,700	10,000

[a]Design life cycles = cycles to failure/10 (stress cycles).
[b]K_t = stress concentration factor.

in 0.5 s, and ramps back to zero in 0.25 s. The equivalent square wave pulse length is 0.33 s. The temperature response of the copper is shown in Figs. 3.1.9 and 3.1.10 for a representative case using an alloy such as CD-182 with 80% of the conductivity of IACS copper. The peak temperature is 102°C with an inlet water temperature of 20°C. Both inlet and exit ends are cooled back to 20°C within 2 min. The water flow velocity was 1.5 m/s with a 100-psi pressure drop. Further data can be found in Appendix B.

Fabrication: Hollow conductor would be desirable for this coil; however, if CD 182 chrome copper is used, it probably cannot be obtained as hollow conductor because of the difficulty in extrusion. One possible design solution is to obtain rectangular solid conductor with a groove on the inside radius face for a 0.3125-in.-diam copper tube. The tube would be soldered and swaged into the groove on a production line.

The coil would be wound four-in-hand with four radial layers on a mandrel using Kapton and G-10 turn-to-turn and layer-to-layer insulation. After winding, the coil would be vacuum-impregnated with epoxy and the mandrel removed. Final machining would be done on the epoxy if required to ensure the proper radial spacing from the vacuum vessel, which must slide over the OH coil with a nominal 0.1875-in. gap.

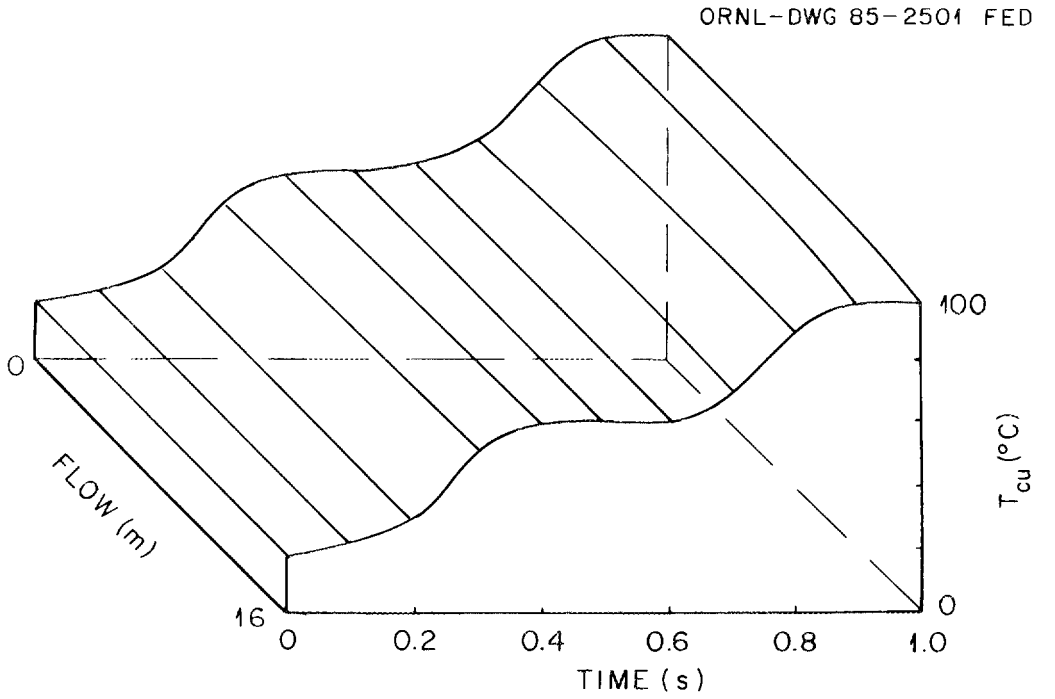

Fig. 3.1.9. OH coil copper temperature as a function of the z coordinate along the flow direction, t = 0 to 1 s, during the sawtooth current pulse.

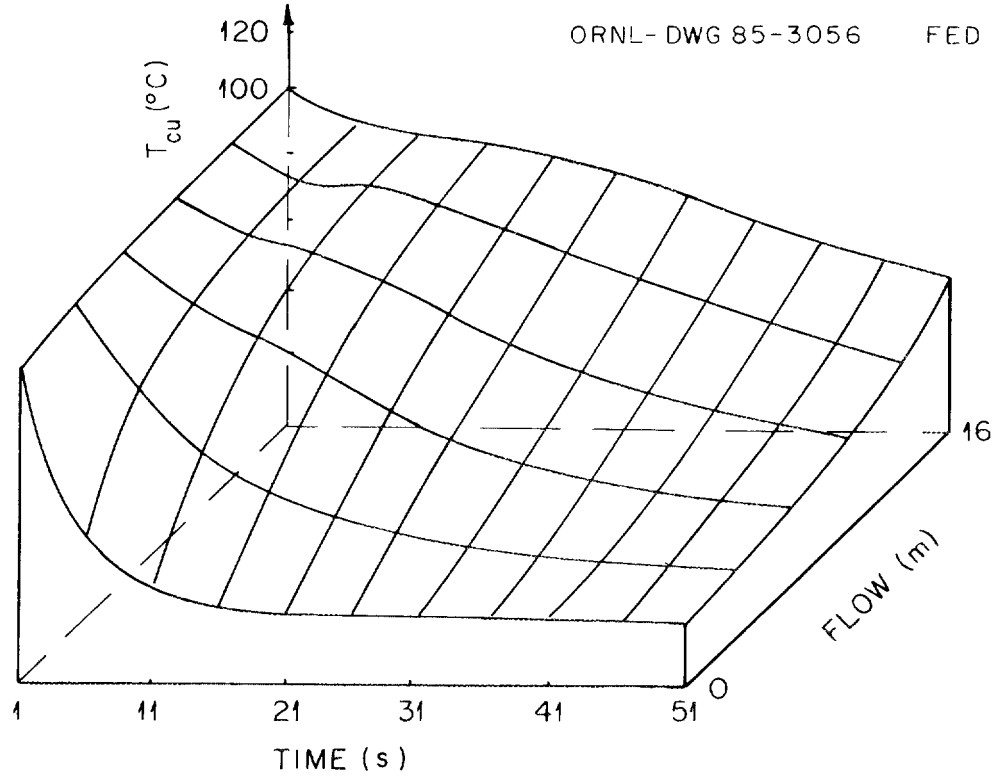

Fig. 3.1.10. OH coil copper temperature as a function of the z coordinate along the flow direction, t = 0 to 51 s after the sawtooth current pulse.

3.1.2.2 S2 through S5 coils

The additional magnetizing field coils (except for the central OH solenoid) are listed in Table 3.1.3 and shown in Fig. 3.1.1. These coils (S2 through S5) are symmetrical above and below the midplane. All solenoid coils are run in series with the central OH solenoid. The combined resistance for the five coils is 63 mΩ and the net inductance is 8.2 mH. The S2, S3, S4, and S5 coils will be hollow-conductor OFHC copper with water cooling.

3.1.3 Poloidal Coil System

The poloidal coils are listed in Table 3.1.3 and consist of vertical field coils (V), radial field coils (R), shaping coils (K), and divertor coils (D). Each set will be run in series from

Table 3.1.3. Poloidal coils

Name	Radius R (cm)	Z (cm)	N (turns)	I (kA)	J_{cu} (kA/cm^2)	ΔR (cm)	ΔZ (cm)	Resistance R (mΩ)	Mass (kg)
S2	22	75	27	23	7.5	10.5	10.5	2.2	102
S2	22	−75	27	23	7.5	10.5	10.5	2.2	102
S3	33	80	3	23	7.5	3.5	3.5	0.36	17
S3	33	−80	3	23	7.5	3.5	3.5	0.36	17
S4	80	80	2	23	7.5	2.9	2.9	0.58	28
S4	80	−80	2	23	7.5	2.9	2.9	0.58	28
S5	120	40	1	23	7.5	2.0	2.0	0.43	21
S5	120	−40	1	23	7.5	2.0	2.0	0.43	21
V	120	30	20	18	6.0	12.6	6.3	8.9	403
V	120	−30	20	18	6.0	12.6	6.3	8.9	403
D4	85	80	10	4	3.7	6.0	6.0	3.5	130
D5	85	−80	10	−4	3.7	6.0	6.0	3.5	130
K	75	80	10	10	3.7	6.0	6.0	3.3	115
K	75	−80	10	10	3.7	6.0	6.0	3.3	115
R	80	74	14	3	0.64	16.0	5.5	2.6	295
R	80	−74	14	3	0.64	16.0	5.5	2.6	295
D1	35	−90	10	−10	7.5	4.2	4.2	2.9	26
D2	45	−70	20	10	7.5	6.0	6.0	7.5	67
D3	55	−90	10	−10	7.5	4.2	4.2	4.6	41
Plasma	45	0		900					

independent power supplies with the polarities indicated. A positive polarity is in the direction of the plasma current. Table 3.1.4 gives the net inductance and resistance for the coil sets.

All coils will be hollow-conductor OFHC copper with water cooling. Insulation will be epoxy-impregnated glass fiber tape with polyimide tape wrapped around turns.

Table 3.1.4. Coil set inductance and resistance

Coil set	*L* (mH)	*R* (mΩ)
Solenoid (S1–S5)	8.21	63.1
Vertical field	6.06	17.8
Shaping (K)	0.71	6.6
Divertor	0.92	22

3.1.4 Toroidal Magnet System

3.1.4.1 Configuration

The toroidal magnet system is required to produce a 0.5-T field at a major radius of 0.45 m on midplane for a 0.5-s plasma current time. The coil set consists of 12 single-turn toroidal field (TF) coils, each carrying a current of 93 kA, as listed in Table 3.1.5.

The 12 inner legs nest together inside the central solenoid in an annular region with an inside radius of 2.5 cm and an outside radius of 7.0 cm. At the top of the central legs will be demountable joints, which make it possible to fabricate the central OH solenoid separately and then to slide it down over the center TF coil legs during machine assembly. The 1.03-m separation between inner and outer legs was selected to keep the field ripple below 1%. The vertical separation was chosen to provide access for assembly and room for the poloidal magnet set support, buswork, and cooling.

Table 3.1.5. TF coil set

Number of coils	12
Current, kA	93
Turns per coil	1
Shape	Rectangular
Height, m	1.97
Radial width, m	1.03
Outer leg cross section, cm	5 × 5
Inner leg cross section	30° arc; 2.5 cm ≤ r ≤ 7.0 cm
Material	OFHC copper (full hard)
Resistance (12 coils), mΩ	0.61
Inductance (12 coils), mH	0.14
Toroidal field on axis (45 cm), T	0.5 for 1 s
Adiabatic temperature rise (inboard leg), °C	55
Pulse repetition rate, min^{-1}	1/3
Total weight (12 coils), kg	1.31×10^3

3.1.4.2 Structural analysis

The computer code BARC was used to estimate the fields and forces on the TF and poloidal field (PF) coils. The centering force on the TF inner legs is 1400 lb/in. and can be accommodated by wedging the coil nose sections. The loads on the horizontal and outer vertical leg will require an external support structure, as discussed in Sect. 3.2. The demountable joint must carry a vertical load of 4700 lb if the external structure does not share the load. A possible configuration is shown in Fig. 3.1.11 and is discussed further in Sect. 3.2.

There will be a lower joint on the central TF coil leg; however, it will not be constrained to remain within the solenoid bore envelope. It appears feasible to develop a configuration that eliminates external buswork with the current supply and return at the bottom of the central leg (see Fig. 3.1.12). In this concept the single-turn coils have a machined offset at the bottom to provide the connections between coils, and there is a return path underneath the offset to cancel the error field.

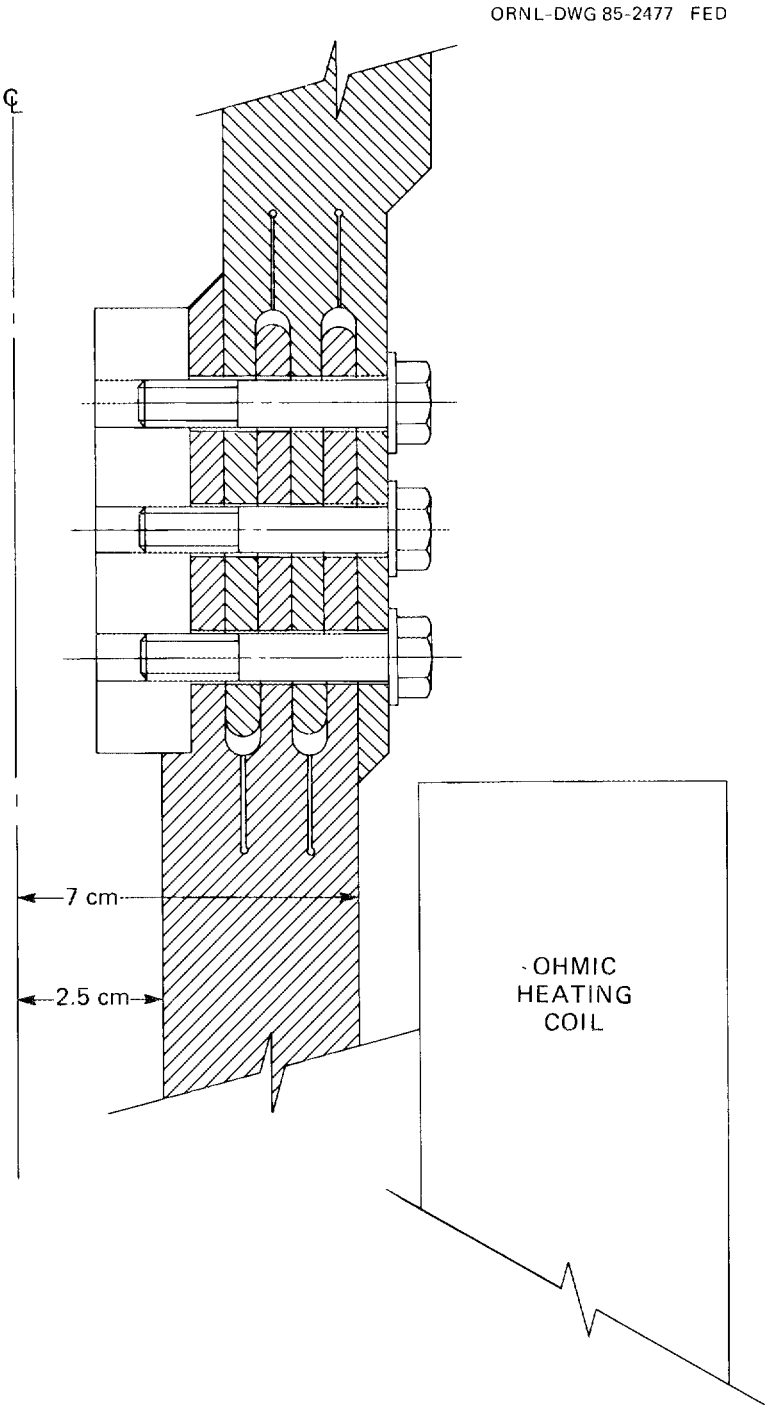

Fig. 3.1.11. TF coil upper demountable joint concept.

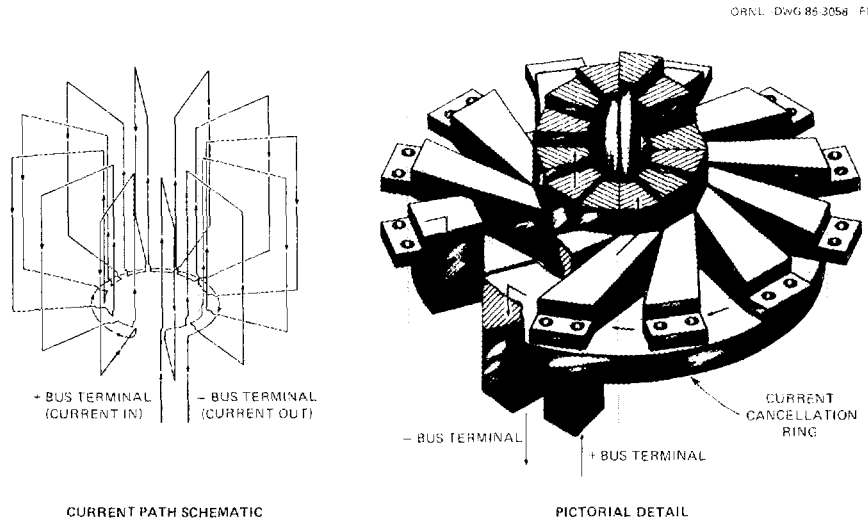

Fig. 3.1.12. TF coil lower joint concept.

3.1.4.3 Thermal analysis

In the central section, the copper current density is 9.9 kA/cm^2, assuming a 0.85 packing fraction. The adiabatic temperature rise, neglecting the water heat capacity, would be 55°C for a 1-s flattop pulse. A 3-min repetition rate can be achieved by cooling with a ⅜-in.-diam copper water-cooling tube within each center leg. The outside legs' adiabatic temperature rise is 7°C, and these will be cooled by natural convection.

3.2 STRUCTURAL SYSTEM

The STX structural support system is designed to support both magnetic and gravity loads. Major structural loads are bridged around the vacuum vessel to avoid the need for support in the central region. For this initial design, coil fault conditions were not considered. Future iterations of support structure design will need to address all combinations of fault conditions and accommodate worst-case conditions. Further information on the structural concept and design details is contained in Appendix A.

3.2.1 Generation of Structural Loads

Mechanical loads were generated for 12 TF coils, 14 PF coils, 5 divertor coils, and the OH solenoid. The BARC magnetic forces and field computer code was used to calculate unit-distributed loading due to magnetic field interaction on all 32 coils.

Loads from five sets of operating conditions were considered: (1) end of flux swing, (2) middle of flux swing, (3) start of flux swing, (4) end of flux swing without divertor or R coils, and (5) end of flux swing with R coil current. Coil currents assumed for these five cases are listed in Table 3.2.1.

3.2.2 Global Magnet Loads

Unit-distributed loading was computed for each coil. Because of the overall asymmetry in coil currents and physical coil locations, coil loadings, even on symmetric coil sets, were not equal and opposite.

3.2.2.1 Poloidal magnet system

On the poloidal coils, including the divertor, distributed vertical loads were integrated to provide overall vertical loads on each coil. Maximum and minimum overall vertical

Table 3.2.1. BARC operating conditions
(see Fig. 3.1.1 for coil set definition)

Case number	Current (kA)						Comments
	Plasma I_p	S coils	V coils	D coils	K coils	R coils	
1	900	−23	−18	10	10	0	End of flux swing
2	900	0	−18	10	10	0	Middle of flux swing
3	0	23	0	10	10	0	Start of flux swing
4	900	−23	−13	0	5	0	End of flux swing without divertor
5	900	−23	−18	10	10	3	End of flux swing with R coils

loads were determined for each poloidal and divertor coil (Fig. 3.2.1). Resultant overall vertical loads for the five operating cases considered are listed in Table 3.2.2.

3.2.2.2 Toroidal coil system

Toroidal coil forces were generated in both the in-plane and out-of-plane directions. Worst-case overall loads on the TF coils are identified in Fig. 3.2.2.

A demountable joint is required in the upper portion of the TF coil inner leg for assembly and disassembly as described in Sect. 3.8. Basic criteria for the design of the joint are as follows:

1. The joint shall carry the full current of the TF coil with minimal impact on overall coil resistance.

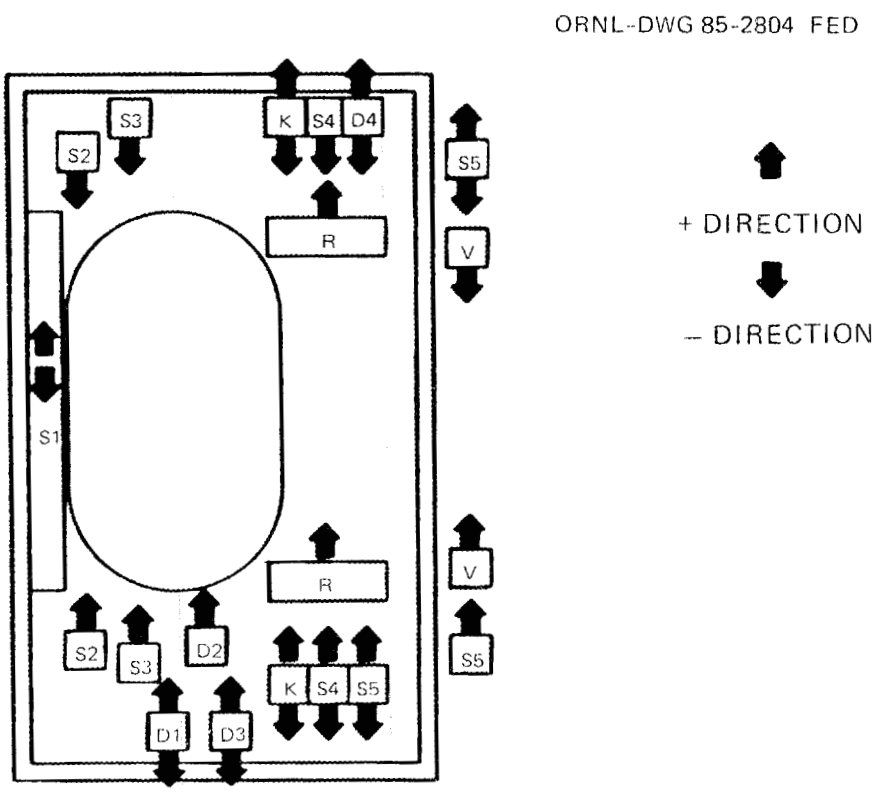

Fig. 3.2.1. Overall loads on PF and D coils.

Table 3.2.2. Vertical loads on PF and D coils for cases described in Table 3.2.1

Coil	Circumferential coil length (m)	Total load (kN) (+ = up, − = down) by case number[a]				
		1	2	3	4	5
S1	0.69	**−16.6**	0	**+18.5**	0	−8.27
S2 Top	1.38	−334	0	**−374**	−324	−334
S2 Bottom	1.28	+222	0	**+486**	+326	+222
S3 Top	2.07	−67.8	0	**−75.2**	−66.2	−67.4
S3 Bottom	2.07	+12.7	0	**+130**	+66.2	+12.2
S4 Top	5.02	**−23.2**	0	−13.7	−15.6	−0.308
S4 Bottom	5.02	+12.3	0	**+24.6**	+15.6	**−10.6**
S5 Top	7.53	−129	0	**+3.96**	−89.2	**−130**
S5 Bottom	7.53	+120	0	+5.00	+89.2	**+121**
D1	2.19	**+79.2**	**−41.8**	−15.1	0	+77.8
D2	2.82	+86.2	**+108**	+107	0	+85.2
D3	3.45	**+2.02**	−68.8	**−107**	0	−3.90
D4	5.34	**+59.6**	+27.4	**−28.8**	0	+14.4
D5	5.34	**+40.8**	−12.2	**−47.6**	0	−4.32
V Top	7.53	−196	**−256**	0	−34.8	−204
V Bottom	7.53	+63.4	**+256**	0	+34.8	+73.4
K Top	4.71	+42.6	+8.20	**−31.4**	+14.2	+136
K Bottom	4.71	−11.1	+20.0	**+62.8**	**−14.1**	+30.0
R Top	5.02	0	0	0	0	**+69.8**
R Bottom	5.02	0	0	0	0	**+2.46**

[a]Worst-case loads are printed in boldface type.

2. The joint shall carry all mechanical loads in the coil at the joint location.
3. The joint shall allow for assembly of the S1 solenoid, vacuum vessel, and other internal components.
4. The joint shall be located in the upper portion of the TF coil inner leg above the level of the top of the S1 solenoid.
5. The joint shall be easily demounted with standard machinists' tools.

The optimum location for the joint is in a region of low TF coil stress and bending. A PAFEC finite-element model of the TF coil, in which the coil is modeled as a series of 105 simple beam elements (Fig. 3.2.3), was developed to find such a region. Magnetic loads generated by the BARC (magnetic fields and forces) code are applied to each beam element. The model assumes that the TF coils are restrained vertically at the top and bottom

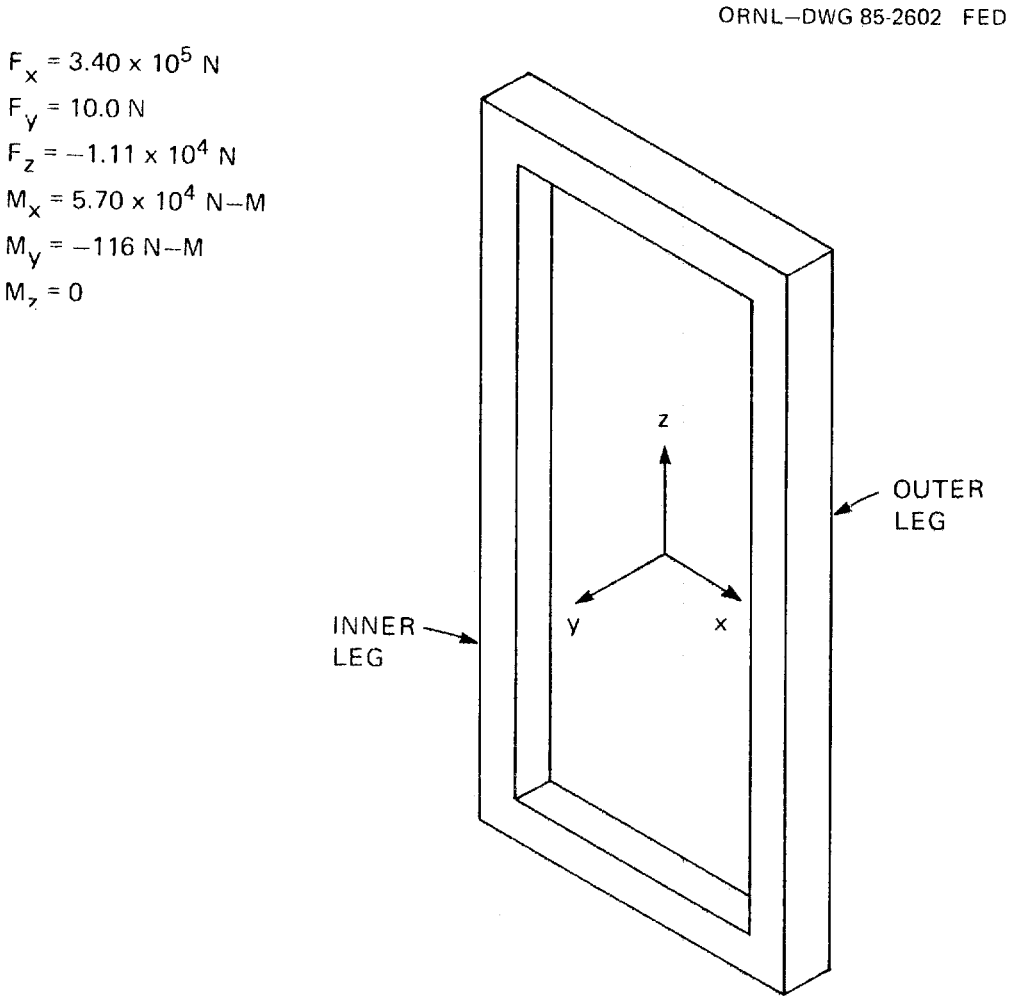

Fig. 3.2.2. Overall loads on TF coils.

of the inner leg by the beams of the overall STX support structure; Fig. 3.2.4 shows constraints applied at other coil support points. The resulting unit loads on beam elements are shown in Fig. 3.2.5 and listed in Table 3.2.3.

In the desired joint area, a location has been found with low bending moments and minimal shear, torsional, and axial loading. At node 40, located 0.17 m below the top of the inner leg, the following forces and moments exist:

ORNL-DWG 85-2806 FED

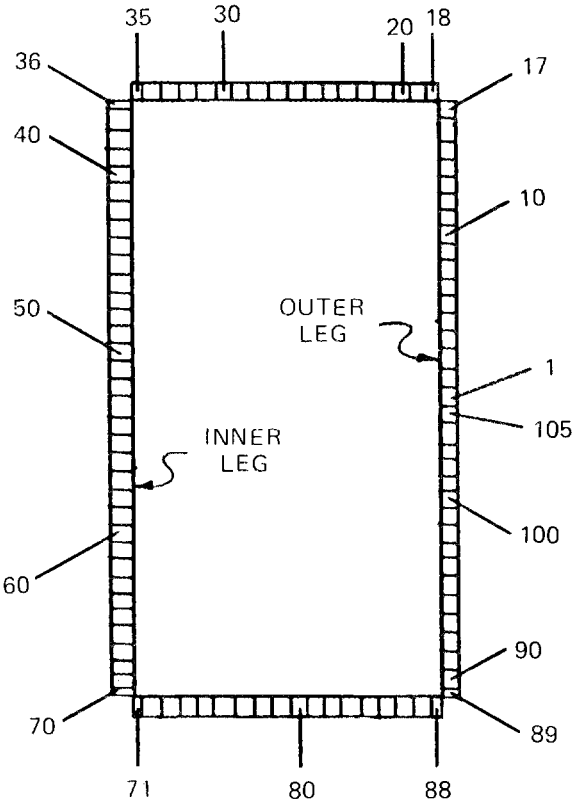

Fig. 3.2.3. Model of TF coil elements.

Axial force	1160 N	(261 lb)
In-plane bending	13 N·m	(115 lb)
Out-of-plane bending	5 N·m	(44 lb)
Axial torsion	21 N·m	(185 lb)
Out-of-plane shear	1008 N	(226 lb)
In-plane shear	4026 N	(906 lb)

The selected joint design consists of a three-fingered joint, similar to the ISX-B design, clamped together with three 0.95-cm-diam shoulder bolts (see Fig. 3.2.6). The bolts are tensioned to provide a contact pressure of 2.07×10^7 N/m^2 (3000 psi) between finger surfaces.

ORNL–DWG 85-2601 FED

	LOCATION	DIRECTION OF RESTRAINT
A	INNER TF COIL SUPPORT RING	OUT OF PLANE
B	MID TF COIL SUPPORT RING	OUT OF PLANE
C	OUTER TF COIL SUPPORT RING	OUT OF PLANE
D	OUTER LEG TF COIL SUPPORT RING	HORIZONTAL IN PLANE AND OUT OF PLANE
E	OUTER LEG TF COIL SUPPORT RING	HORIZONTAL IN PLANE AND OUT OF PLANE
F	OUTER TF COIL SUPPORT RING	OUT OF PLANE
G	MID TF COIL SUPPORT RING	OUT OF PLANE
H	LOWER NOSE SUPPORT	VERTICAL IN PLANE
I	ALL NOSE ELEMENTS	HORIZONTAL IN PLANE AND OUT OF PLANE
J	UPPER NOSE SUPPORT	VERTICAL IN PLANE

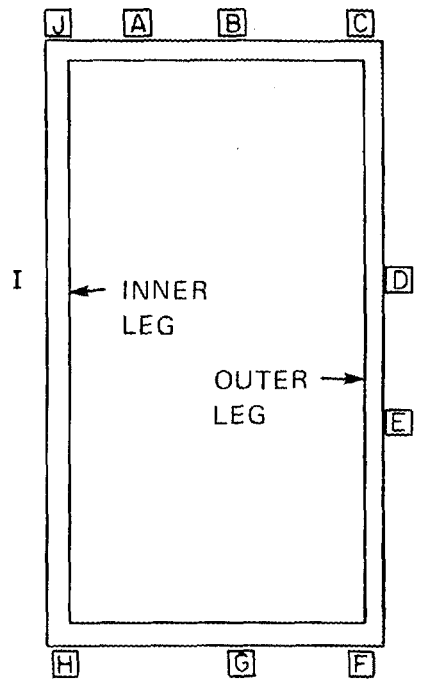

Fig. 3.2.4. TF coil model restraints.

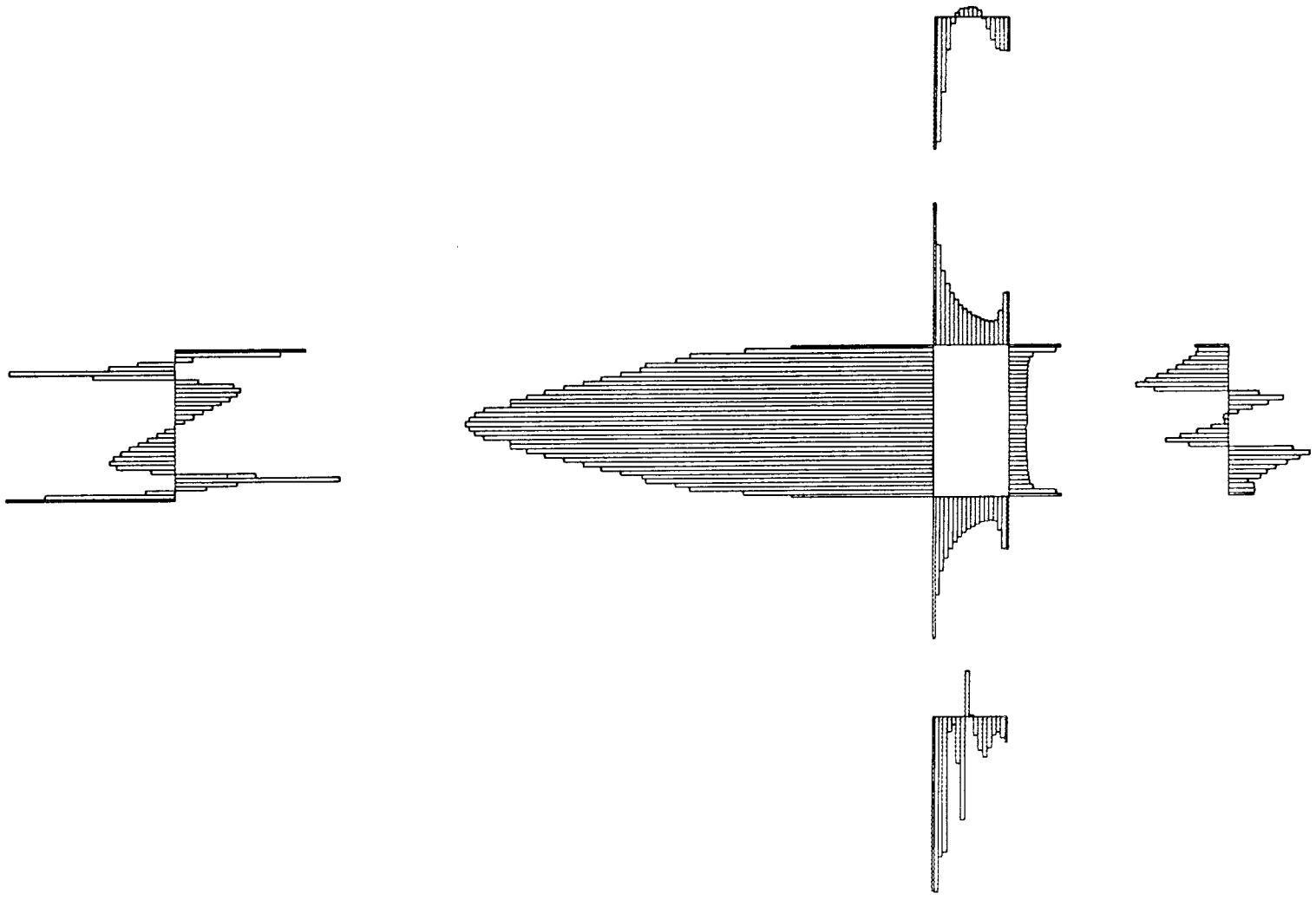

Fig. 3.2.5. Proportioned view of loads on TF coils.

Table 3.2.3. TF coil loads

Element number	Unit force in plane (kN/m)	Unit force out of plane (kN/m)	Element number	Unit force in plane (kN/m)	Unit force out of plane (kN/m)	Element number	Unit force in plane (kN/m)	Unit force out of plane (kN/m)	Element number	Unit force in plane (kN/m)	Unit force out of plane (kN/m)
1	10.3	2.25	28	20.2	−5.16	55	258	−10.6	82	14.2	−18.9
2	10.4	−5.26	29	22.6	−4.61	56	253	−15.9	83	13.7	−22.5
3	10.4	−13.3	30	25.5	−2.70	57	238	−21.1	84	13.4	−17.2
4	10.4	−22.4	31	29.3	3.64	58	238	−26.4	85	13.8	−10.5
5	10.4	−30.9	32	34.5	18.1	59	229	−31.0	86	19.0	−8.32
6	10.4	−17.2	33	41.6	41.4	60	219	−35.1	87	29.3	−12.0
7	10.4	41.9	34	56.0	69.1	61	208	−37.1	88	29.7	−14.7
8	10.5	52.0	35	79.7	73.8	62	197	−33.4	89	29.7	−14.7
9	10.5	46.8	36	79.7	73.8	63	187	−13.6	90	26.9	−14.9
10	10.6	40.1	37	106	59.6	64	176	45.7	91	13.9	−14.7
11	10.6	34.2	38	137	10.1	65	164	93.1	92	11.9	−16.0
12	10.9	29.5	39	145	−21.2	66	162	35.0	93	11.1	−18.4
13	11.1	25.6	40	162	−37.7	67	145	17.6	94	10.9	−22.0
14	11.9	22.0	41	165	−94.7	68	137	−16.8	95	10.6	−26.9
15	13.9	18.6	42	176	−46.5	69	107	−74.5	96	10.6	−33.6
16	26.8	17.6	43	187	13.3	70	79.7	−96.3	97	10.5	−40.4
17	29.7	19.0	44	197	33.4	71	79,7	−96.3	98	10.5	−46.1
18	29.7	19.0	45	208	37.2	72	56.1	−97.1	99	10.4	−36.4
19	29.3	18.8	46	219	35.1	73	41.6	−77.7	100	10.4	22.4
20	19.1	18.5	47	229	31.0	74	34.5	−75.2	101	10.4	35.8
21	13.8	17.5	48	238	26.2	75	29.3	−8.32	102	10.4	27.1
22	13.4	12.6	49	238	21.0	76	25.5	−4.40	103	10.4	17.9
23	13.7	6.83	50	253	15.8	77	22.7	−25.9	104	10.3	9.70
24	14.5	0.916	51	258	10.5	78	20.2	−57.1	105	10.5	2.17
25	15.6	−3.88	52	261	5.23	79	18.4	25.7			
26	16.8	−5.42	53	263	−0.00556	80	16.8	0.0973			
27	18.4	−5.44	54	261	−5.33	81	15.6	−10.1			

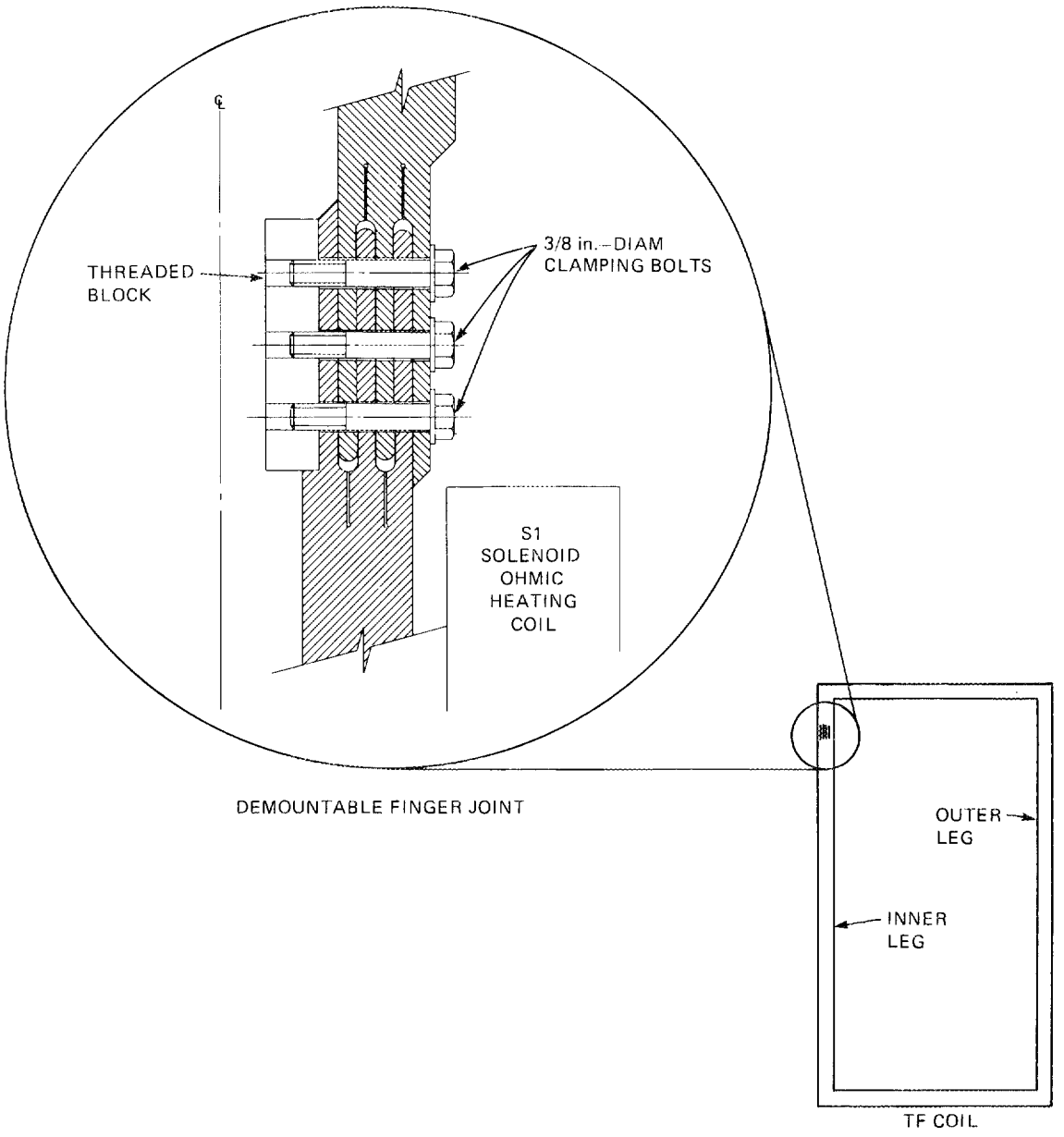

Fig. 3.2.6. Demountable finger joint design.

When dismantled, the joint surface provides no obstruction to assembly of the S1 solenoid, vacuum vessel, or other components. Joint assembly consists of sliding the two joint halves together, inserting three bolts, and torquing the bolts to the required pre-tension.

Under the applied loads, the fingers experience a maximum principal stress of 2.07 × 10^7 N/m^2 (3000 psi) at the root of the outermost fingers. The bolts experience a maximum principal stress of 1.79 × 10^8 N/m^2 (26,000 psi), including both coil loads and clamping pre-tension.

The magnetic loads used in this joint design are steady-state loads with all coils operating at design current. Coil failure and transient conditions have not been addressed. Under standard conditions, a demountable joint in the inner TF coil leg appears feasible with readily available materials and reasonable factors of safety.

3.2.3 Gravity Load

For these initial calculations each coil was considered to have no case. The weight of each coil was assumed to be the weight of copper to fill up the coil volume. Coil weights are given in Table 3.2.4. The overall structural concept is shown in Fig. 3.2.7.

Table 3.2.4 Coil weights

Coil name	Number	Unit weight (kg)	Total weight (kg)
TF	12	102	1224
S1	1	484	484
S2	2	124	248
S3	2	50	100
S4	2	45	90
S5	2	79	158
D1	1	35	35
D2	1	92	92
D3	1	56	56
D4	1	158	158
D5	1	158	158
V	2	213	426
K	2	34	68
R	2	39	78
Total of all coil weights			3375

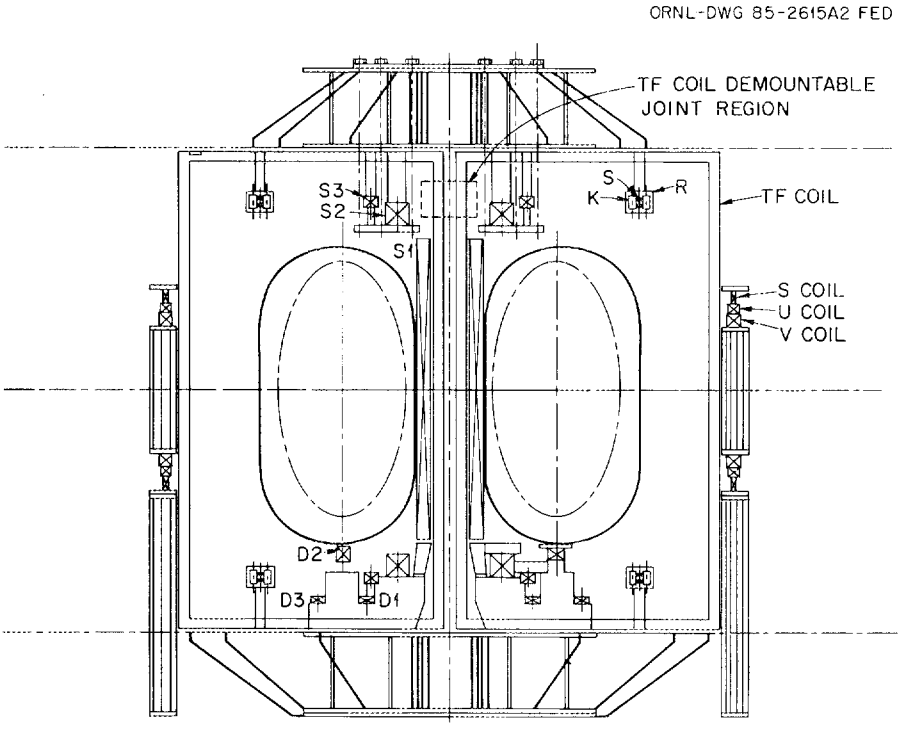

Fig. 3.2.7. Overall structural concept.

3.3 POWER CONDITIONING

3.3.1 Assumptions

The following assumptions are made for the power conditioning of STX.

1. Major items for OH, TF, vertical field (VF), and shaping field (SF) power supplies will be salvaged from the existing ISX-B toroidal power supply, which is rated at 1000 V dc and 120 kA, pulsed for 0.6 s on a 10% duty cycle. It is composed of eight identical modules, each rated at 500 V dc and 30 kA. The planned upgrade for the ATF will replace the existing transformer, SCRs, and dc bus of each module to provide a power supply for the helical field of ATF. The discarded items will be reassembled into separate power supplies for STX. These salvaged modules will not meet the ultimate needs of STX because the proposed short-pulse loading of approximately 88 MW on the existing

40-MVA transformer will produce excessive voltage drop. Thus, during initial operation, the OH and VF power supplies will be voltage-limited.

After the initial experimental program is completed, a second 40-MVA transformer (currently available but not in use) will be installed in parallel with the existing 40-MVA transformer. The regulation of all the power supplies will be improved, and the output voltage of the VF power supply will be increased to the experiment design requirement.

The addition of the second transformer alone will not produce the voltage needed to drive the OH coil to 23 kA. During the shutdown for installing the second transformer, the four OH power supply transformers will be rewound to obtain the increase in output voltage required to reach the experiment design point.

2. Space will be available on the first floor of Bldg. 9201-2 to install the power supplies.

3. Bus C of the 13.8-kV switchgear and the 40-MVA transformer primary supply will be dedicated to the STX experiment.

4. Four existing 13.8-kV circuit breakers will be available for STX use.

5. The STX experiment will be located in the High Power Test Facility (HPTF) area on the second floor of Bldg. 9201-2.

6. Provisions must be made to dedicate the 13.8-kV bus C to STX. Three motor-generator (MG) sets (S1, S2, and S3) tie to this bus, as do the ISX-B 60-kV power supply, the 150-kV power supply, and the ISX-B pulsed power supplies. The MG sets will not be used and can be deenergized. The three ISX-B power supply feeders will need to be switched to 13.8-kV bus D (see Fig. 3.3.1), which has four spare circuit breakers to accommodate them. These moves will free breaker compartments so that STX can be supplied from a dedicated bus, bus C.

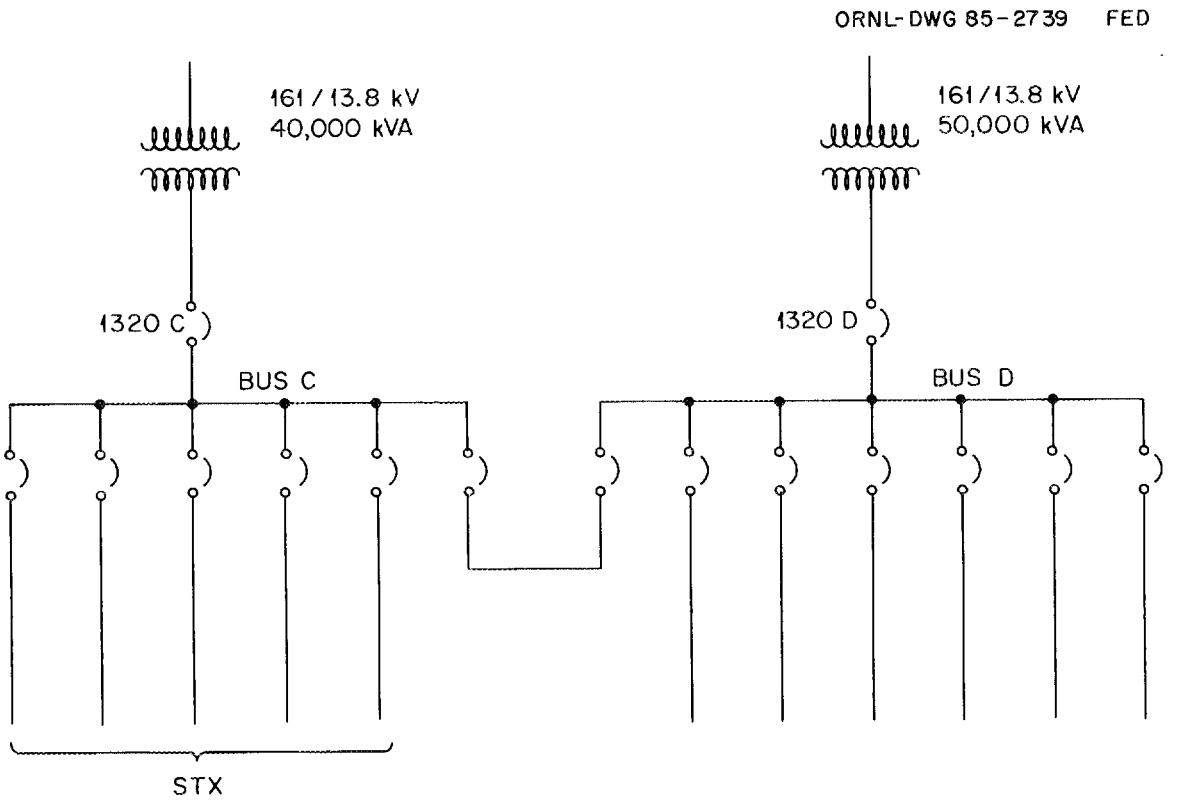

Fig. 3.3.1. 13.8-kV power source.

3.3.2 OH Power Supply (S1–S5)

For power, ohmic heating requires 23 kA at $R = 0.082\ \Omega$, $L = 0.0082$ H, ramped from 0 to 23 kA in 0.25 s. Four modules, built using the discarded transformers and SCR assemblies from the ATF upgrade, will be installed on the first floor of Bldg. 9201-2. These modules will be series-connected to conduct 18 kA into the OH coil. Insufficient output voltage from the existing power supply due to the steep regulation curve limits the volt-seconds obtainable (see Fig. 3.3.2). The addition of a second 40-MVA transformer in parallel with the existing 40-MVA transformer will improve the regulation of all power supplies. Rewinding the OH power supply transformers to obtain an increase in output voltage will provide the needed drive voltage.

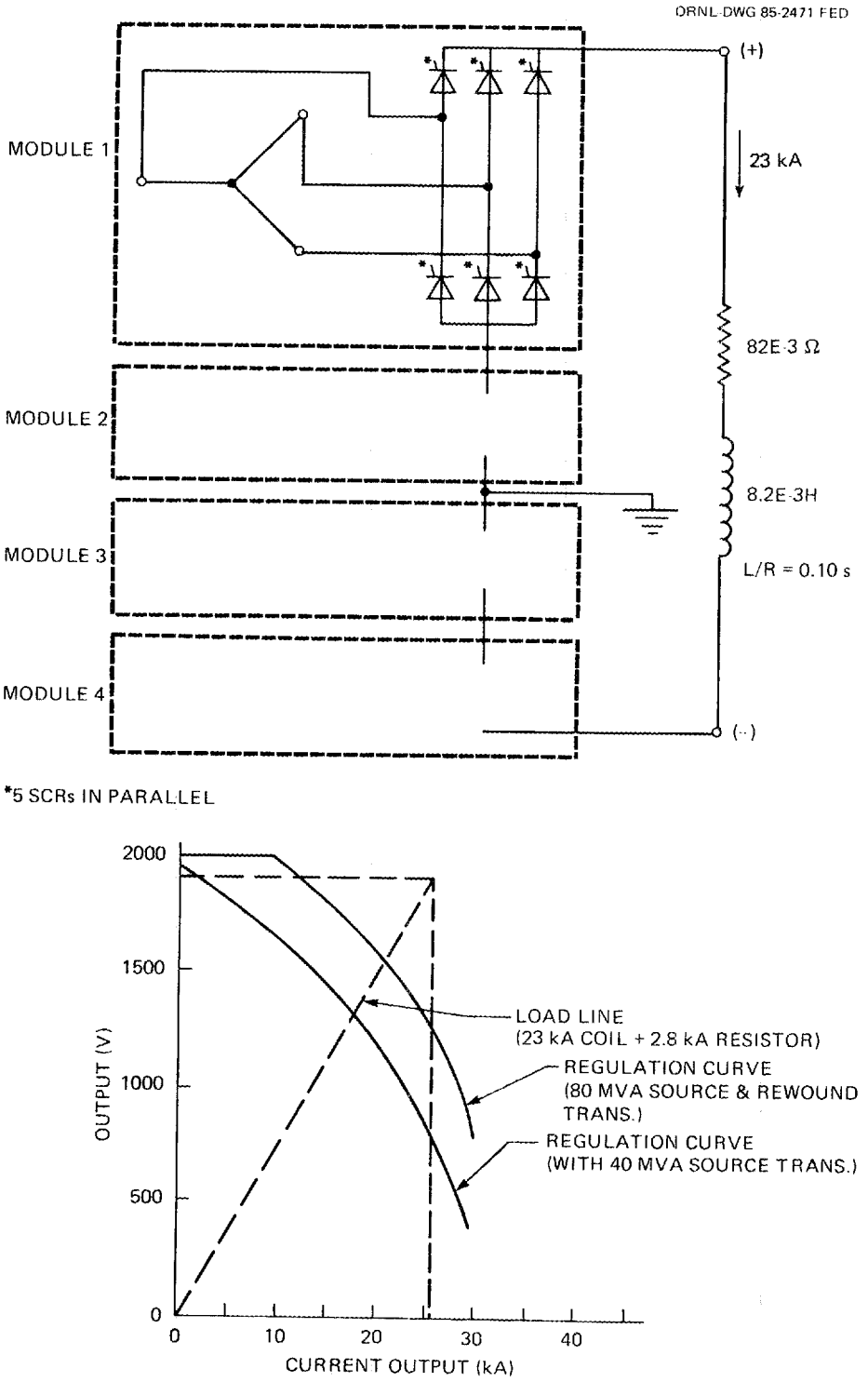

Fig. 3.3.2. OH power supply regulation curves.

3.3.3 OH Switching (Plasma Initiation)

Ohmic heating switching requires a 12-kV ionization potential. This OH power supply will be incorporated in a circuit that will divert an established current of 18 kA from the power supply into a resistor to generate 12 kV (see Fig. 3.3.3). Suitable current interrupting and reversing switches, protective circuitry, and controls will be provided to monitor and control the OH current from zero to +18 kA, +18 kA to −18 kA, and back to zero, thus providing the required ionization potential to establish a plasma and 65% of the experiment design capability (see Fig. 3.3.4). These switches will function without modification when the improvements described in Sect. 3.3.1 have been completed and will handle the 23 kA required to meet the full needs of the experiment.

3.3.4 TF Power Supply

The TF coils require 93 kA at $R = 0.00061\ \Omega$, $L = 0.00014$ H, ramped from 0 to 93 kA in 125 ms at 135 V (Fig. 3.3.4). Two modules of the existing ISX-B toroidal power supply will be reassembled as in the OH power supply. However, the modules will be

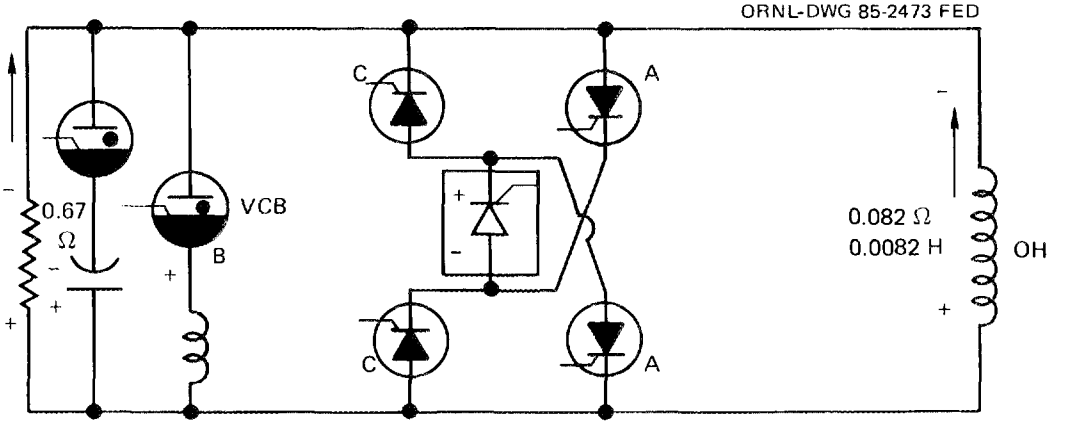

Fig. 3.3.3. OH power supply.

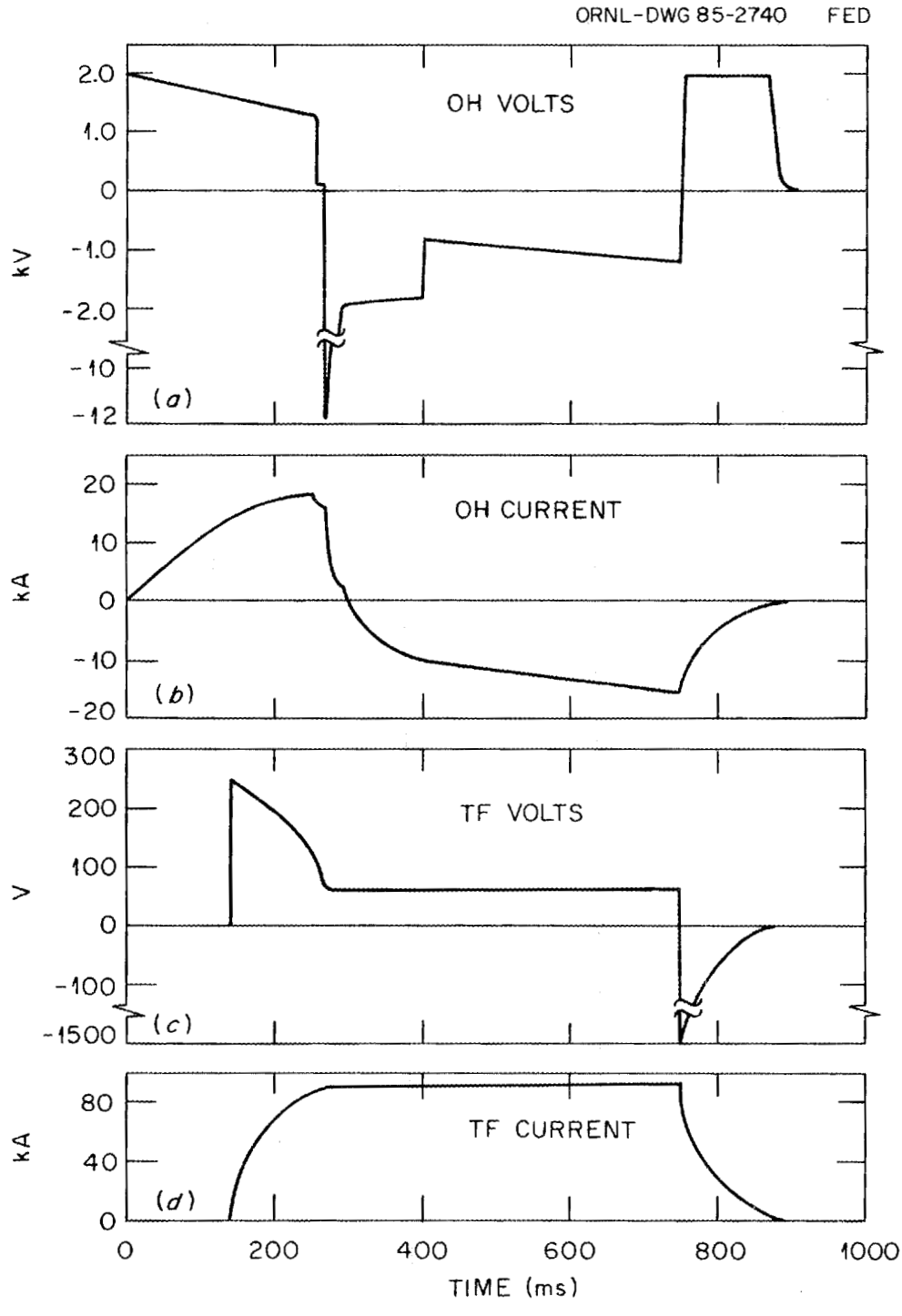

Fig. 3.3.4. Current and voltage waveforms for OH and TF coils.

reconfigured to produce 252 V (open circuit) at 47 kA per module with two modules connected in parallel to produce 135 V at 93 kA (see Fig. 3.3.5).

This will require rewinding the existing rectifier transformers to provide a double-Y secondary capable of producing 135 V at 23.25 kA each. The SCRs will be reconnected to carry 23.25 kA in the four-Y secondary circuit, thus producing 93 kA dc at 135 V dc from only two modules that are designed to produce 60 kA dc at 500 V dc.

3.3.5 VF Power Supply

The vertical fields require 18 kA at $R = 0.018\ \Omega$ and $L = 0.006$ H, ramped from 0 to 18 kA in 0.2 s. One module of the existing ISX-B toroidal power supply will be reassembled to produce 18 kA dc at 297 V. This is approximately 50 V below the voltage needed to drive the current from 0 to 18 kA in 0.2 s. The addition of the second 40-MVA transformer, as described in Sect. 3.3.1, will correct this situation.

3.3.6 Shaping Power Supply

The shaping power supply requires 10 kA at $R = 0.013\ \Omega$ and $L = 0.002$ H, ramped from 0 to 10 kA in 0.2 s. One module of the existing ISX-B toroidal power supply will be reassembled to produce 10 kA at 341 V, which is adequate.

3.3.7 Radial Power Supply

The radial power supply requires ± 3 kA at $R = 0.028\ \Omega$ and $L = 0.004$ H, with fast-response current regulation. An existing ISX-B four-quadrant battery power supply with a series transistor regulator will be used to drive the radial field. Open circuit potential is ± 72 V dc.

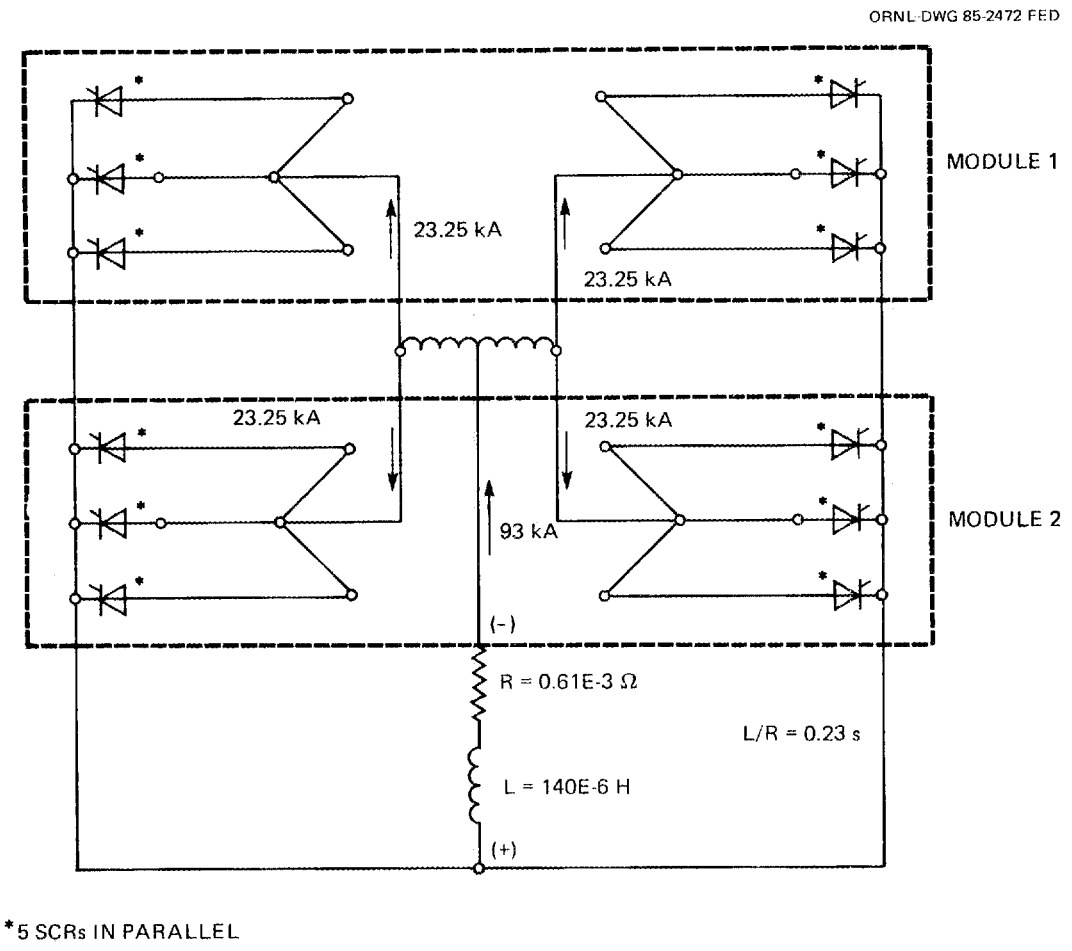

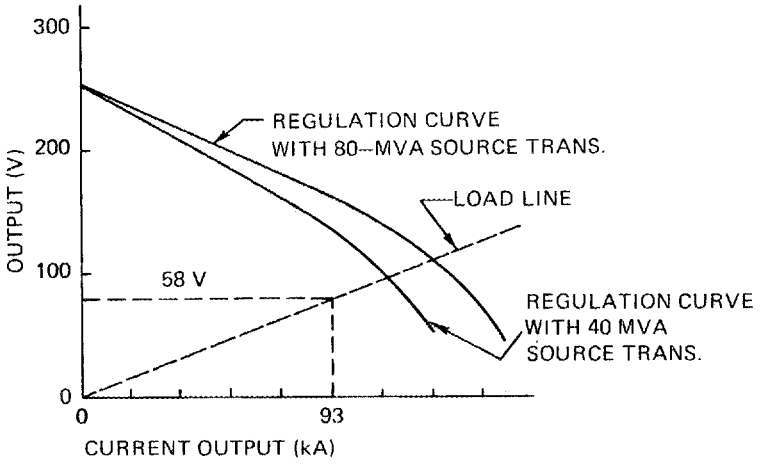

Fig. 3.3.5. TF power supply (top) and regulation curves (bottom).

3.3.8 Divertor Power Supply

The divertor coils require 10 kA at $R = 0.028\ \Omega$ and $L = 0.001$ H, ramped from 0 to 10 kA in 0.05 s. No power supply will be provided for the divertor coils during the initial phase of STX. When the divertor coils are required during a later phase of the experimental program, a new power supply similar to the ISX-B bundle divertor supply will be built. The secondary of an existing transformer will be rewound to produce the needed secondary voltage. An SCR module will be fabricated in-house and installed on the first floor of Bldg. 9201-2. This supply will receive its power from switchgear bus D (see Fig. 3.3.1). The 50-MVA building transformer supplies this bus, and spare circuit breakers are available.

3.3.9 Electrical Distribution

Existing facilities within Bldg. 9201-2 can provide the 480/240/120-V services required. Electrical equipment will be installed to provide power for the vacuum system, cooling equipment, lighting, receptacles, controls, and miscellaneous equipment.

3.4 VACUUM VESSEL

The vacuum vessel was sized for an elliptically shaped plasma with a width of 54 cm, a height of 108 cm, and a major radius of 45 cm. Plasma motions of ± 5 cm vertically and 5 cm radially outward were also included in the sizing. A 3-cm edge space was allowed on the inside between the plasma and wall. A simple racetrack shape, similar to that of the Poloidal Divertor Experiment (PDX), was chosen, with all coils external to the vessel. The principal dimensions and characteristics are given in Table 3.4.1, and the cross section and plasma size are shown in Fig. 3.4.1.

Table 3.4.1. Vacuum vessel

Shape	Racetrack
Inside radius, cm	15
Outside midplane radius, cm	81.3
Dome radius of curvature, cm	33
Cylindrical section height, cm	57.8
Total height, cm	123.8
Thickness	
Outer cylinder, cm	0.635
Domes and inner cylinder, cm	0.32
Toroidal resistance, mΩ	0.23
Critical pressure, MPa (psi)	1.65 (240)
Material	Inconel 625
Primary limiter	Graphite rail from ISX
Divertor	Poloidal with graphite baffles

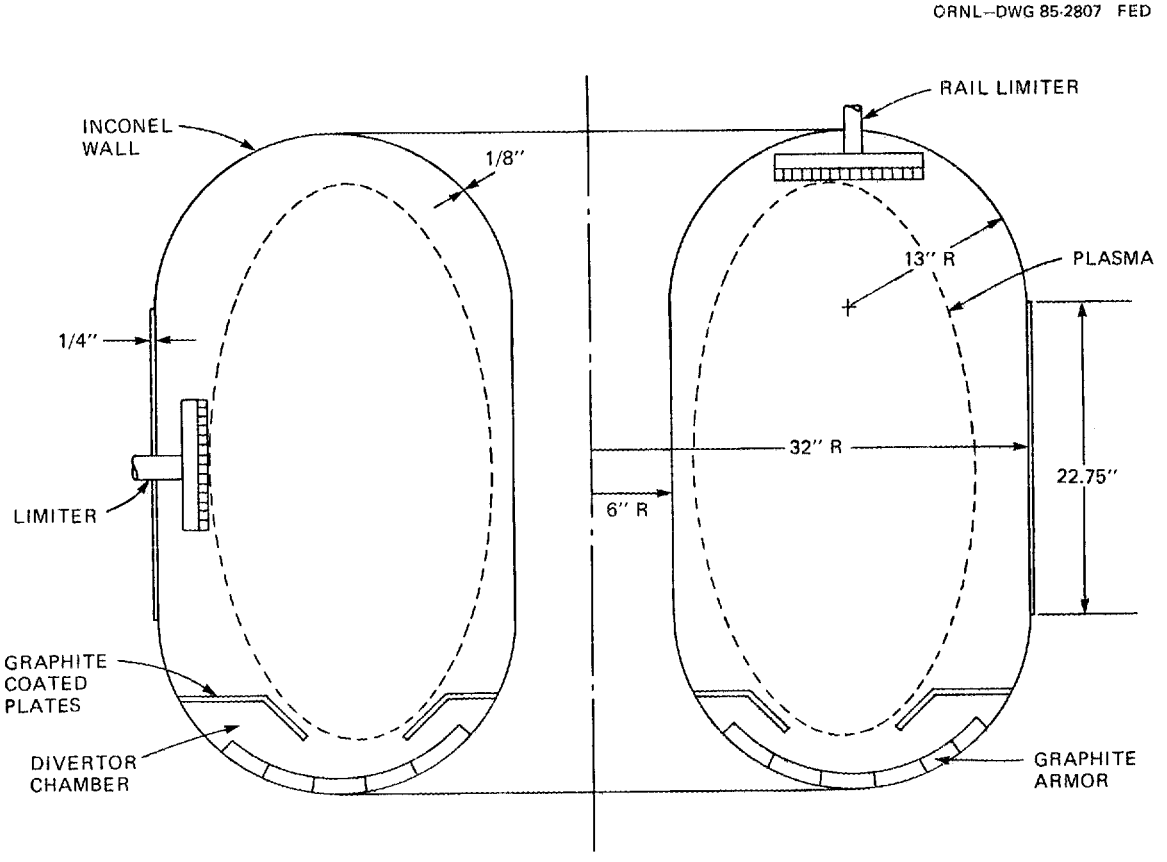

Fig. 3.4.1. STX vacuum vessel.

Because space on the inboard side is particularly valuable when trying to achieve a low aspect ratio, it was decided to use a thin wall vessel without bellows or ceramic breaks. To increase the toroidal resistance, the thickness was minimized and Inconel rather than stainless steel was selected because its resistivity is nearly 75% higher. For the baseline design, the vessel wall is 3 mm (0.125 in.) thick, except for the outside cylindrical wall, which is 6 mm (0.25 in.) thick. With these thicknesses and the dimensions in Table 3.4.1, the toroidal resistance is 0.23 mΩ. The vessel would be fabricated using spinnings for the upper and lower dome sections and rolled plate for the cylindrical walls.

3.4.1 Structural Analysis

An external pressure of 2 atm was applied uniformly to a finite-element model of the vessel, shown in Fig. 3.4.2, to simulate vacuum and plasma disruption pressure loading.

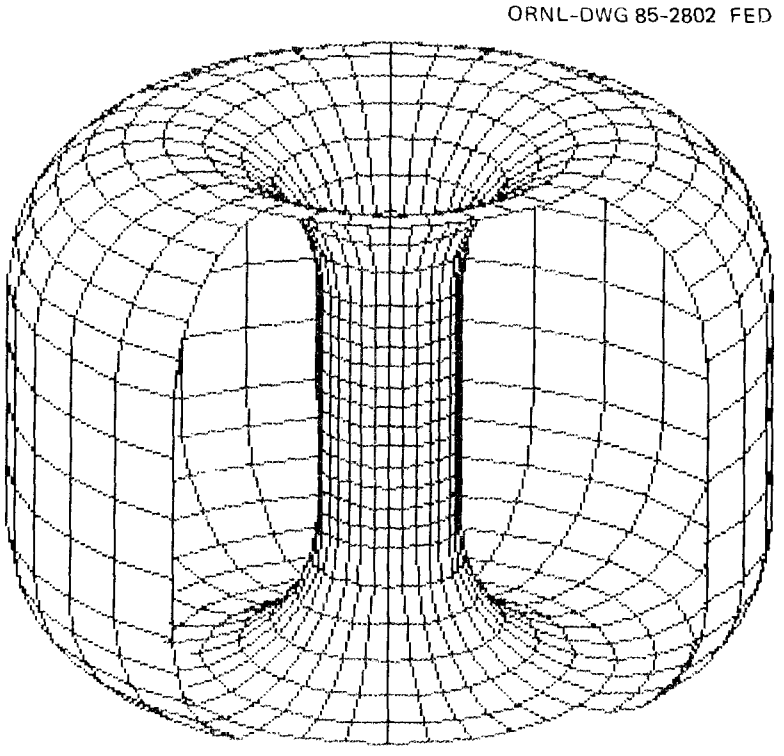

Fig. 3.4.2. Vacuum vessel finite element model.

The critical pressure for buckling was 240 psia, as shown in Fig. 3.4.3 (with the distortions greatly exaggerated). Using a factor of 4 for buckling, the design pressure limit would be 60 psia, which means a disruption pressure load equivalent to 45 psia steady state could be tolerated. A preliminary estimate of the disruption pressure loading was made under the assumptions that immediately after a disruption the plasma current is uniformly distributed in the vacuum wall and that the internal tangential magnetic fields are small. The peak radial pressure was 97 psi on the inner wall and 18 psi on the outer wall. These

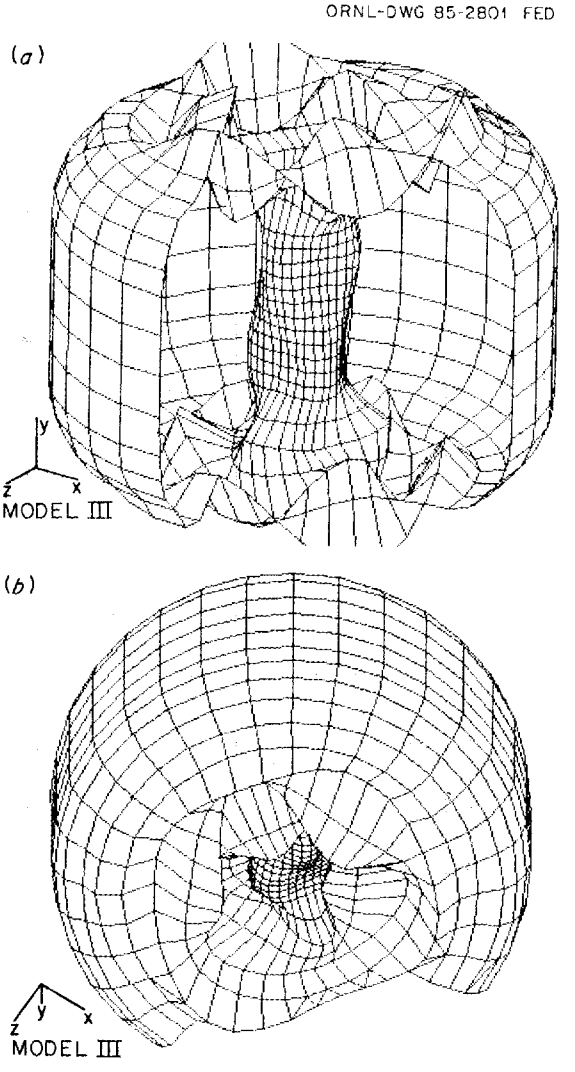

Fig. 3.4.3. Magnified displacements at the critical pressure.

pressures should be tolerable because the high inner pressure gives a tensile load that does not cause buckling, while on the outer cylinder the load is less than the buckling design limit of 45 psi. The assumption of uniform current distribution is conservative and gives higher peak pressures on both the inner and outer walls than will be generated.

At 30 psi, the stresses were low, with the highest Von Mises stress being 7,380 psi, compared to a design-allowable stress intensity of 34,000 psi for Inconel 625. A complete description of the structural analysis can be found in Appendix B.

3.4.2 Limiter

The primary limiter will be a rail installed in the top of the vacuum vessel, as shown in Fig. 3.4.1. It will be similar in design to the limiter used for the beryllium experiment on ISX-B. The tiles will be TiC-coated graphite and will include a thermocouple array as a plasma diagnostic. A rectangular port on the top of the vessel will be provided for the limiter. A limiter will also be used on the outboard side. Mechanical design and cooling requirements will be developed during the conceptual design phase.

3.4.3 Divertor

A divertor chamber will be formed in the lower section of the vessel with fixed baffle plates, as shown in Fig. 3.4.1. The plates will be graphite or graphite-coated for impurity control. The divertor chamber is plasma plugged during a pulse, and the whole vessel would be evacuated to base pressure between pulses. Mechanical design and cooling requirements will be developed during the conceptual design phase.

3.4.4 Neutral Beam Line Interface

The vacuum vessel will have two 30-cm-diam ports for the entrance and exit of the neutral beam. These ports will be designed for the beam to be tangent on a 40-cm radius, as shown in Fig. 3.4.4. The back port will be used as a beam dump with graphite armor tiles.

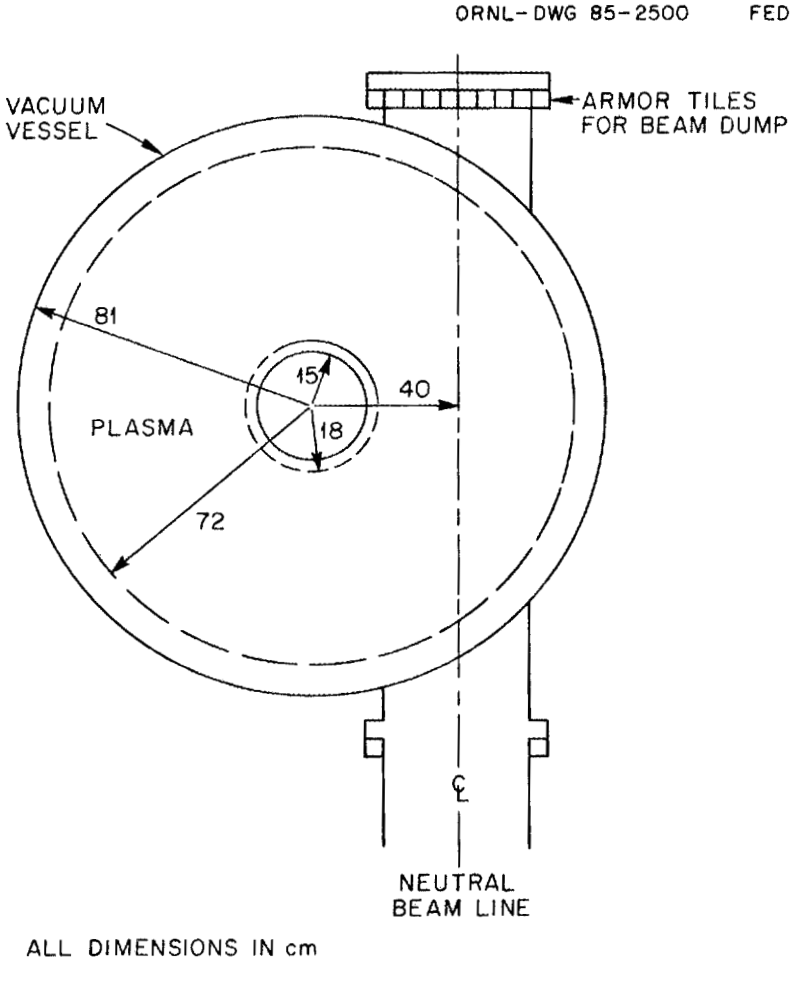

Fig. 3.4.4. Neutral beam line arrangement.

3.4.5 Diagnostic Ports

The diagnostic port configuration is still preliminary. However, there will probably be approximately twenty-four 2.75-in. ports, twelve on the top, twelve on the bottom; six 8-in. ports on centerline between magnets; and twelve 6-in. ports above and below the centerline on the outside radius. All diagnostic ports except for Thomson scattering are expected to have circular conflat flanges. In addition, two 10-in. circular ports on centerline will be provided for vacuum pumping.

3.4.6 Thermal Analysis

The basic vacuum vessel shell was analyzed for 2 MW of heat input in 0.5 s with a 3-min repetition rate. It was assumed that half the power went to the limiter and half was uniformly distributed over the inside surface. For this case the outside could be cooled by natural convection with a semi-steady-state temperature rise of 92°F. The inner radius could be cooled by flowing nitrogen gas or instrument air in a 0.1875-in. gap between the central solenoid and the vacuum vessel.

3.5 FACILITY SYSTEMS

3.5.1 Site

It is proposed that the STX device be located in the High Power Test Facility (HPTF) enclosure in place of the target chamber on the existing beam line assembly (see Fig. 3.5.1). The enclosure has a controlled environment and controlled access, and the work area is serviced by a 2-ton bridge crane.

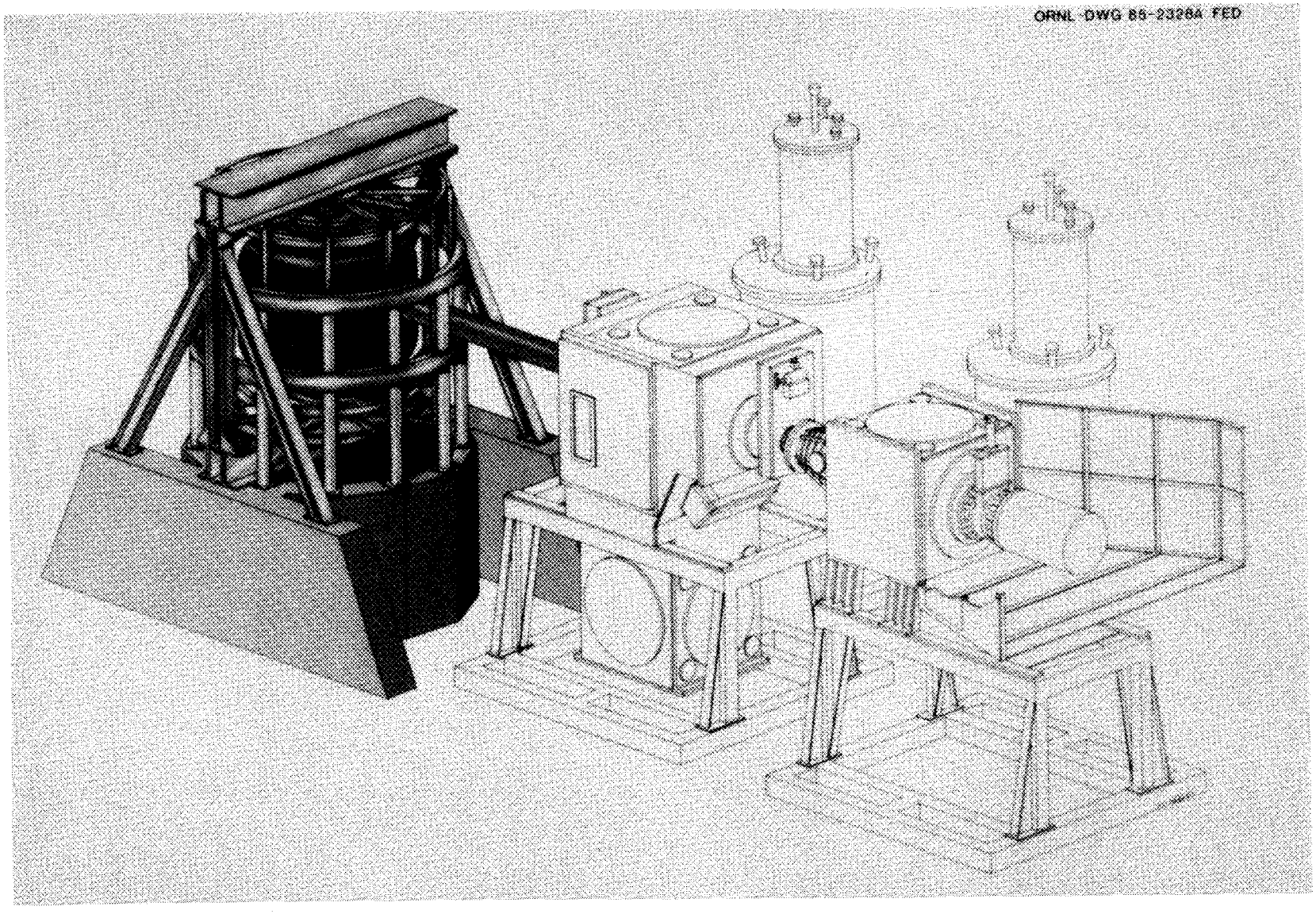

Fig. 3.5.1. The HPTF with STX replacing the target module.

An existing control and data acquisition area is large enough for the experimental needs of the device. An electrostatically shielded 12- by 16-ft room next to the HPTF contains data acquisition systems sensitive to rf interference.

3.5.2 Utilities

The utilities facilities include the following:

1. Cooling water. The building heat dissipation needs are met by a closed-loop demineralized water cooling system that dumps into a 40-MW water-to-water air cooling tower. An adequate supply (>1200 gpm) of high-pressure (225-psi) water exists at the site.

2. Electrical systems. The power requirements for the STX coil systems are covered in Sect. 3.3. All power and controls associated with HPTF neutral beam operation exist at the site and require no modification. Adequate 115-V, 208-V single-phase, 220-V, and 440-V power exists at the site for the STX peripheral systems.

3. Vacuum systems. An adequate pumping system, including safety interlock control, is available. There are two cryopumps, three turbomolecular pumps, and three Roots blowers. Minimum effort will be needed to recommission the vacuum system.

4. Cryogens. The building liquid nitrogen system services the HPTF area. Liquid lines from a phase separator feed the existing beam cryopumps. Liquid helium (LHe) needs will be met by transferring LHe from existing 1000-L dewars available in the building. Three liquefier-refrigerators are operating near the STX facility on other experiments—a Koch Model 1400, a Koch Model 1630, and a CTI-Cryogenics Model 1430. Commercial procurement of LHe for STX operation is expected to be minimal.

3.6 NEUTRAL BEAM HEATING

A single neutral beam injector, operated on the HPTF beam line, will be used to heat STX. The beam will be injected tangentially, as described in Sect. 3.4, because the device

is small. The 30-cm-diam source will be similar to those used on ISX-B and PDX and will operate at a beam energy of 40 keV (H^0), a source current of 100 A, and a pulse length of 300 ms. With a tangency radius of 0.4 m, the beam absorption length in the plasma is 119 cm. With a species mix of 40:30:30 in the neutrals, we have calculated the shinethrough loss for STX as follows:

n_e ($\times 10^{13}$ cm^3)	Beam power transmitted (%)
1.33	14.5
2.00	9.2
3.67	2.9
5.33	0.9

The neutral beam injectors used in ISX-B experiments can deliver high-power beams of 2-MW H^0 at 40 keV for 300-ms pulses. Such injectors can be modified to deliver beams at other energies by regapping the ion accelerator. If the ion source of the injector is gapped to produce 50-keV, 100-A hydrogen ion beams with a current ratio of 80%, 10%, and 10% respectively for H^+, H_2^+, and H_3^+, the power of neutral beams injected through a 30-cm-diam injector port into a plasma 4.5 m downstream will be about 2.4 MW. Here, we assume that the ion accelerator has a focal length of 4.5 m and delivers a beam with an e-fold divergence angle of 1°. By lowering the accelerator voltage, the injector can be operated to produce neutrals at lower energies, substantially decreasng the power of the neutral beam injected into the plasma. As shown in Fig. 3.6.1, the neutral power is 1.6 MW at 40 keV and 0.9 MW at 30 keV. With the 1.3° beam divergence angle of the existing source, the injected neutral power will be lower, with a value corresponding to 60% of that shown in the figure.

At the moment, most of injector components (e.g., ion source, gimbal, neutralizer, power supplies, electronics, cryopumps, and other necessary utilities) are available. Two components require improvements: the ion accelerator and the ion dump. A new

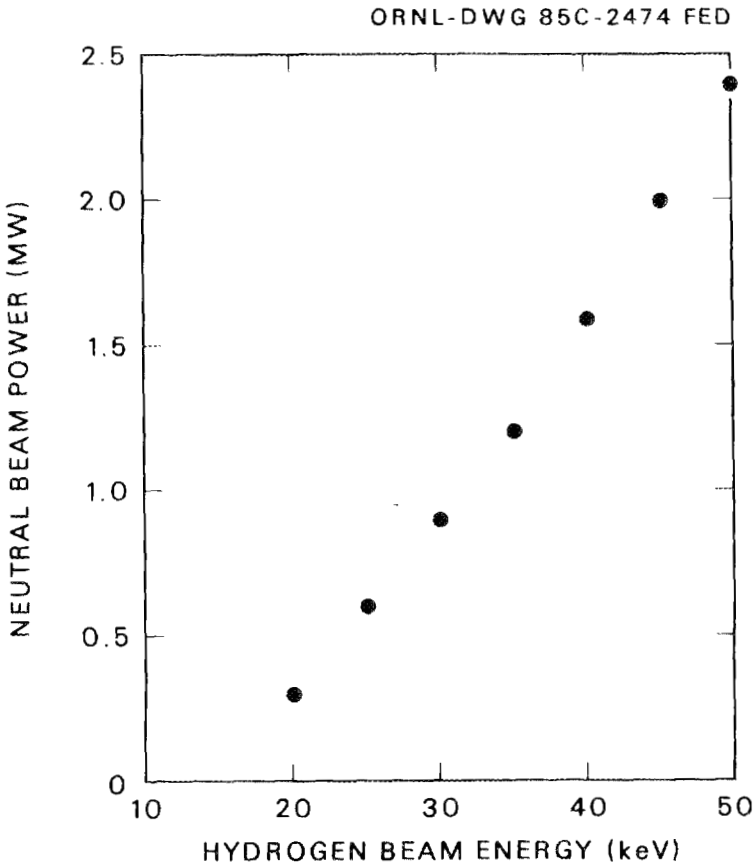

Fig. 3.6.1. Neutral beam power vs hydrogen beam energy.

accelerator is needed to improve the beamlet divergence angle (θe) from 1.3° to 1°, and the ion dump has a water leak problem and needs repair. Hence, the effort to prepare a functional neutral beam injector for STX will be minimal.

3.7 INSTRUMENTATION AND CONTROL

A schematic of the instrumentation and control (I&C) system proposed for STX is shown in Fig. 3.7.1. The system can be broken into three integrated primary components that together will provide operator-oriented machine control and monitoring. The first is the shot control system, which consists of CAMAC modules and feedback controllers to perform basic waveform generation and timing functions. The shot control system would

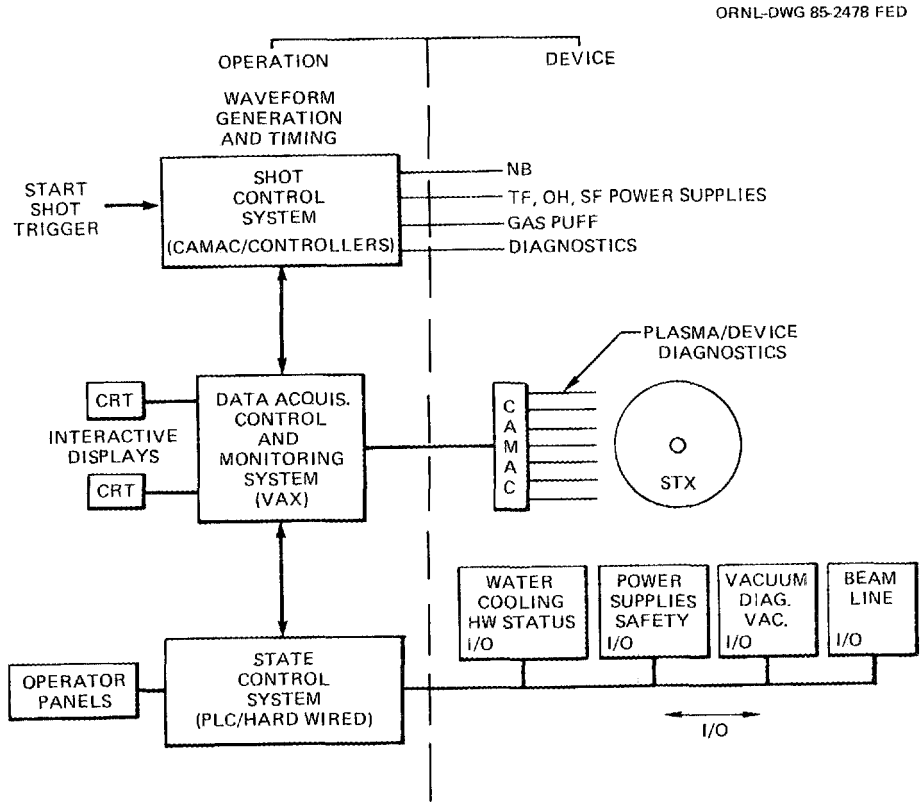

Fig. 3.7.1. STX I&C system block diagram.

control all time-critical functions such as neutral beam firing, power supply control, and gas puff operation. The second component is the data acquisition system, which performs the functions of data acquisition, shot control system programming, and state control system monitoring. The VAX-based data acquisition system would use ORNL-developed CAMAC and timing software (SAMS). The data acquisition system would be operated through interactive CRT displays. The third component of the system is the state control system, which will monitor, control, and interlock all devices that operate in the on/off state. The state control system would be based on hardwired interlocks for all safety and critical components and would use a programmable logic controller (PLC) for the remainder of the system. The state control system would be operated through panels for each of the various device subsystems.

The STX I&C system would use much of the experience gained in the ISX experiment at ORNL. It would incorporate a similar grounding scheme and employ many of the specialized controllers developed for use in the shot control system. In addition, it would incorporate existing controls and monitoring instrumentation from the HPTF for use in the beam line and vacuum systems of STX. Basic plasma diagnostics and device diagnostics would be provided in the STX I&C system.

3.8 ASSEMBLY PLAN

The basic device assembly plan is shown in Fig. 3.8.1. The lower external beam structure and intercoil structure would be installed first. The center TF coil cylinder and lower radial legs would be fabricated as one subassembly and installed with the lower TF coil support structure. The lower coil cradle assembly and coils S3, D1, D2, D3, lower K, S4, and R would also be installed at this time, as shown in Fig. 3.8.1(a).

The central OH solenoid would then be installed by sliding it down over the TF center column. The bottom water cooling lines would be connected next, and then the lower S2 coil would be installed. The next major step is lowering the vacuum vessel down over the OH solenoid, as shown in Fig. 3.8.1(b).

After installation of the vacuum vessel, the upper S2, S3, K, S4, and R coils would be lowered onto temporary supports, slightly lower than their final positions. This will give additional access to the TF coil joints on the center column. The TF coils would then be installed as shown in Fig. 3.8.1(c) by making bolted connections on the center column and at the lower outside corners. The remaining structure and coils are then assembled and the upper PF coils are raised and installed in the proper position, as shown in Fig. 3.8.1(d). The coils and vacuum vessel assembly would then be raised as a unit into position on the neutral beam line.

ORNL–DWG 85-2606 FED

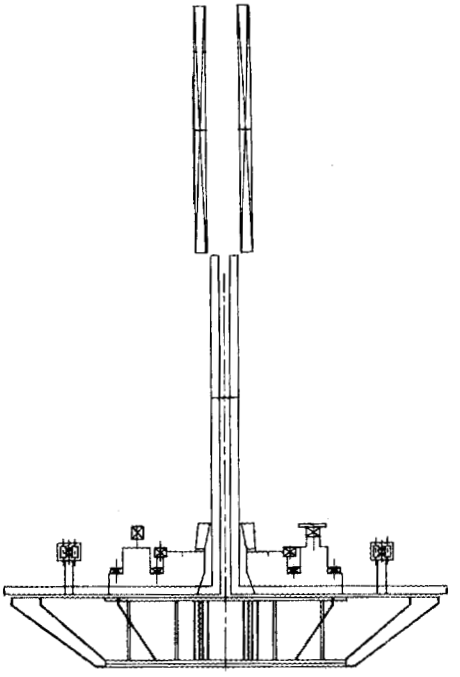

(*a*) CENTER TF AND LOWER SUBASSEMBLY

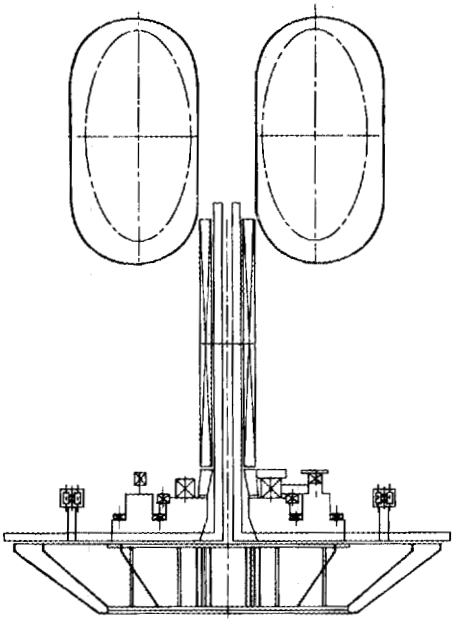

(*b*) VACUUM VESSEL INSTALLATION

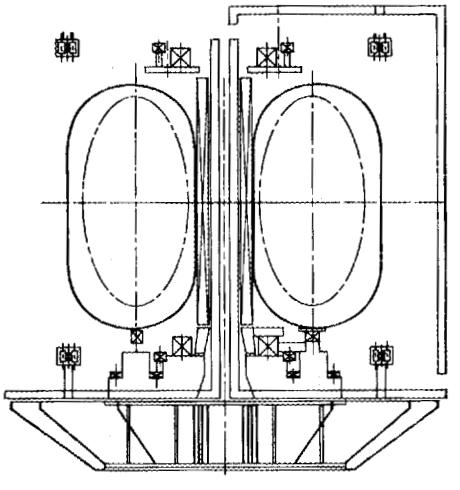

(*c*) TF COIL INSTALLATION

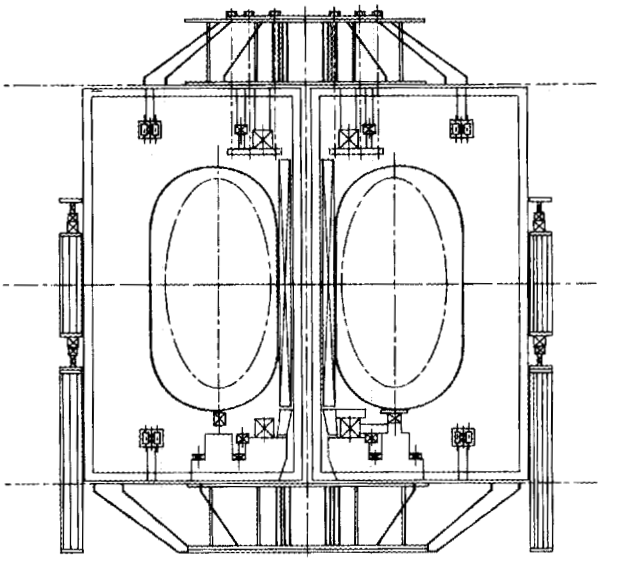

(*d*) COMPLETED MACHINE

Fig. 3.8.1. STX assembly sequence.

3.9 STX COST AND SCHEDULE PROJECTIONS

The costs and schedule discussed in this section have been derived from the design established in support of the physics objectives. While specific conceptual details were not available at this phase of design definition, the understanding of the device components and subsystems has been sufficient to allow calculation of design data and definition of fabrication and assembly processes.

Confirmation of a more realistic cost estimate and device schedule must wait until a conceptual design is completed. This level of design work will serve to reduce the uncertainties and provide a base of actual drawings and bills of materials for cost estimates.

3.9.1 Cost Projections

Cost calculations for most components relied on a base of design data that defined the materials, sizes, weights, and fabrication processes. Costs for the various elements were then established as follows.

- Material costs were calculated from design size and weight or specific hardware procurements of material identified.
- Labor hours required to fabricate the component parts were assigned to scheduled tasks with the magnitude based on the particular process step and the complexity of the component.
- Labor hours required to assemble the component or subsystem were determined by crew-size loading against schedule time lines and the assembly sequence defined for the reference device design.
- Engineering hours were developed by man-loading each specific design task for each Work Breakdown Structure (WBS) element.

- Contingency was defined by assigning a percentage to each participant and phase in each WBS element. This provided a distributed allocation weighted to reflect higher values for the more complex or high-risk items.

The results of these calculations are shown in Tables 3.9.1 and 3.9.2. The first table summarizes the cost projection by major item. It should be noted that escalation is not included now, since a specific schedule has not been identified for proceeding with the device project.

The second table provides a more detailed breakdown of cost by WBS element and participant. This table also includes a few selected percentage calculations, which are usually of interest for comparative purposes.

Table 3.9.1. Summary of STX cost projections

Item	Cost (in thousands of FY85 dollars)	
Engineering		
Design TI/II	780	
TIII	243	
Project management	181	
Total		1204
Procurement/fabrication		
Magnets	993	
Structure	753	
Power	561	
I&C	271	
Interfaces	23	
Total		2601
Assembly		986
Subtotal		4791
Escalation (not included at this time)		
Contingency		1176
Total		5967

Table 3.9.2. STX cost projections

WBS	Item	Cost (in thousands of FY85 dollars)						
		Engineering[a]			Procurement/ fabrication	Assembly	Contingency[b]	Total
		Design	TIII[c]	PM[d]				
1.3.1.1	OH	94	36	30	238	21	94	513
1.3.1.2	TF	50	10	5	217	41	76	399
1.3.1.3–6	P-coils	120	38	24	538	53	160	933
1.3.2.1	Vacuum vessel	64	13	8	181	14	66	346
1.3.2.2	Structure	115	44	35	487	192	209	1082
1.3.2.3	Device support	31	8	6	85	41	40	211
1.3.3	Power supplies	157	53	47	561	356	344	1518
1.3.4	I&C	104	31	21	271	227	158	812
1.3.5	Interface	45	10	5	23	41	29	153
Total		780	243	181	2601	986	1176	5967[e]

[a]Engineering is 33.6% of fabrication/assembly cost.
[b]Contingency is 24.5% of device base cost.
[c]TIII is 31.2% of design engineering cost.
[d]Project management is 17.7% of design plus title III cost, 5.0% of fabrication/assembly cost.
[e]Cost is not escalated.

3.9.2 Schedule

Schedule elements have been defined for each WBS item and are further subdivided into the design, procurement/fabrication, and device assembly tasks. The duration of each task is based on a detailed evaluation of engineering man-loads, assumptions on procurement or fabrication time, and assembly crew efforts.

The individual WBS items' schedules were not constrained in any way, and each is based on aggressive, success-oriented, and properly sequenced design, procurement/fabrication, and assembly. The total schedule was constructed by time-phasing each WBS item to an appropriate constraint. This approach allows for smoothing of resource peaks in engineering and assembly craft labor and for distributing funding requirements for a more optimum relationship to actual work needs.

The resulting overall duration of 30 months is a minimum-slack, critical-path schedule with the time-phasing of elements consistent with the device assembly logic. Figure 3.9.1 presents a summary-level schedule with the major activity time lines indicated. This figure

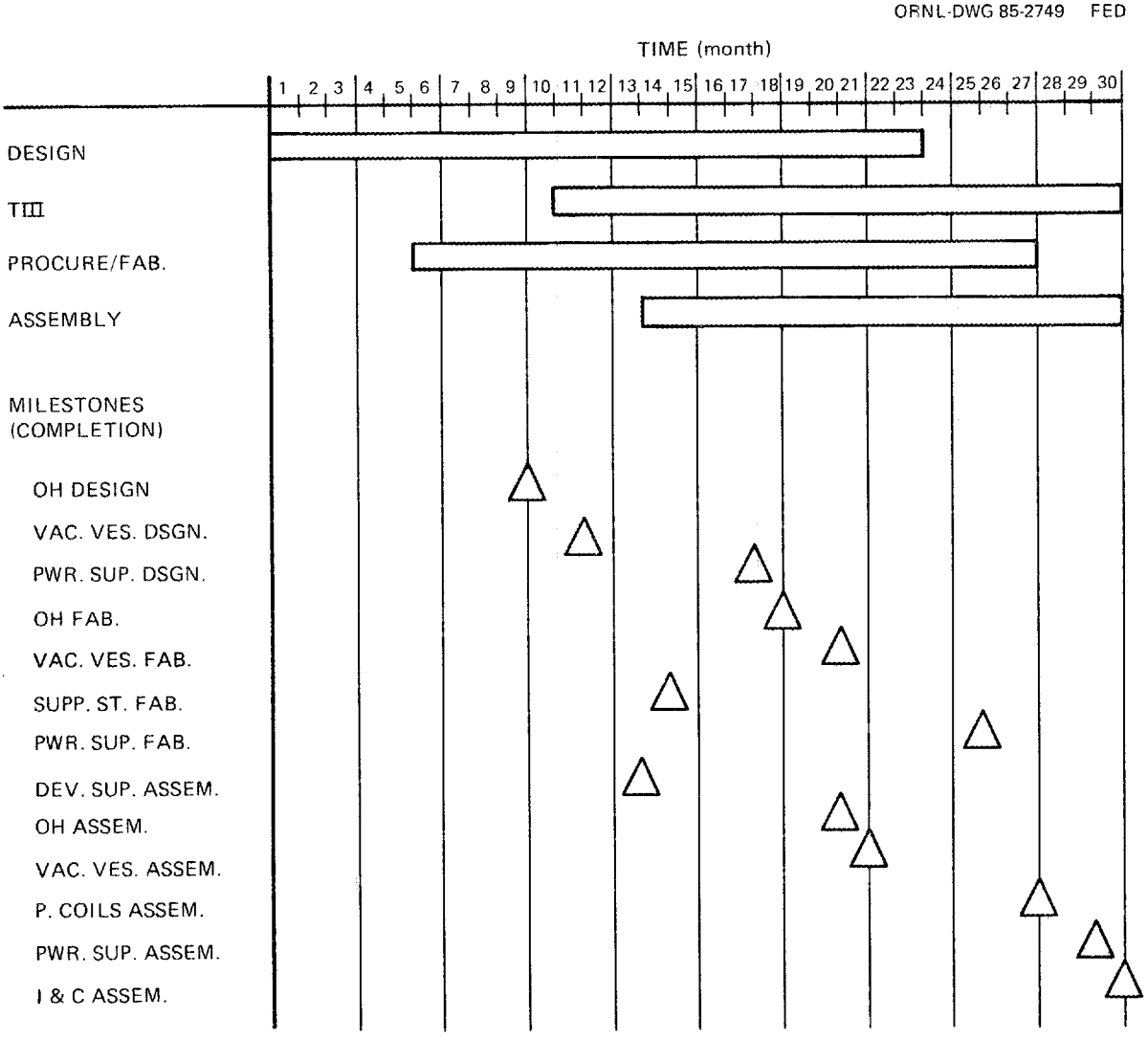

Fig. 3.9.1. STX planning schedule, showing major tasks and completion milestones.

also includes a list of milestones (completion of tasks) that are considered to be the more critical items. This provides some insight into the more detailed flow shown in Fig. 3.9.2. This figure indicates the timespans and relationships of design, procurement/fabrication, and assembly for each WBS element. The time phasing of the various component parts and the assembly sequence relationship are also incorporated in this figure.

Engineering and assembly craft crew sizes have been estimated from the detailed WBS cost and schedule worksheets and time-phased against those shown in Fig. 3.9.2. This results in the histograms shown in Fig. 3.9.3. The engineering manpower profile

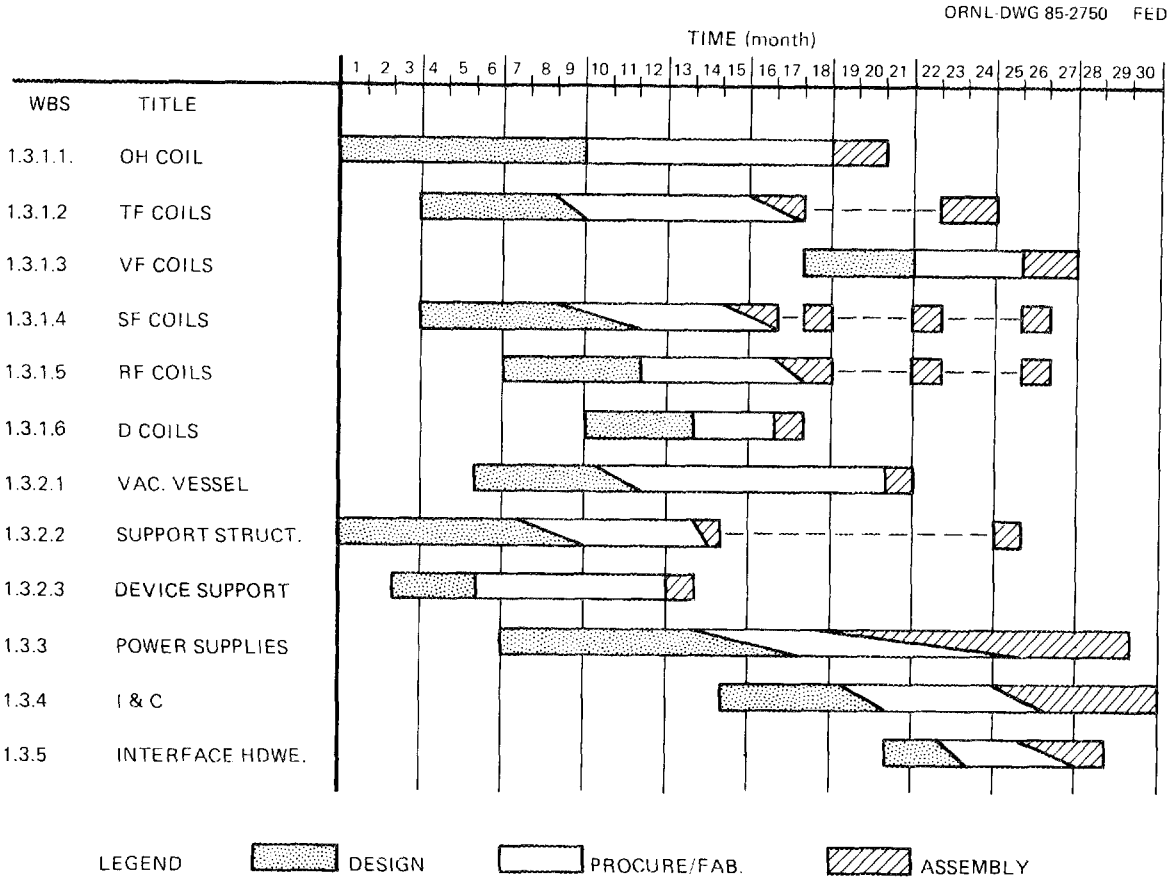

Fig. 3.9.2. Planning schedule showing work breakdown structure (WBS) and participants.

reflects a reasonable distribution of work with no significant peaks that would constrain resource assignments. The assembly crew profile indicates a substantial peak when the poloidal coils are installed. This could be adjusted over a time span of two to three months to flatten this peak, should staffing at this level or conflict in use of space around the device prove to be a problem.

3.9.3 Funding

A possible funding plan is shown in Table 3.9.3. This plan is based on completion of conceptual design in December 1985 and initiation of the project in January 1986. This schedule of events would result in completion in July 1988.

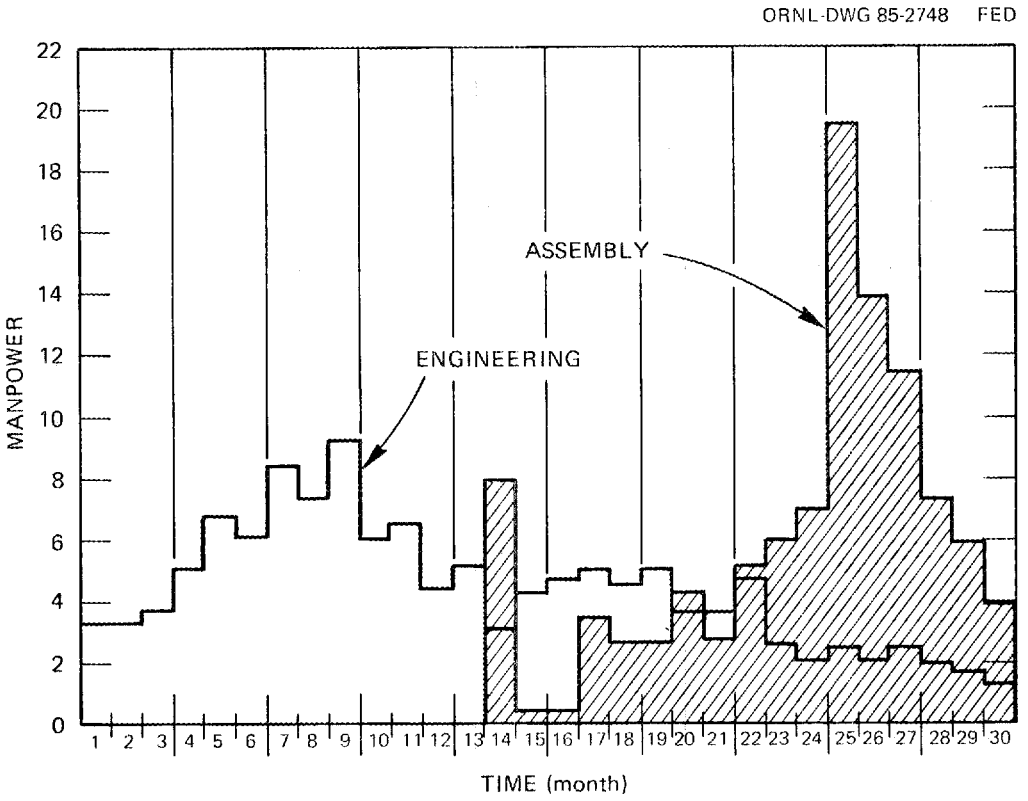

Fig. 3.9.3. STX work planning profile, showing engineering and assembly crew sizes.

Table 3.9.3. Possible funding plan

	Funding (in millions of dollars)							
	FY86		FY87		FY88		Total	
	BA	BO	BA	BO	BA	BO	BA	BO
Base	1.4	0.8	2.4	2.7	1.0	1.3	4.8	4.8
Contingency	0.2	0.2	0.5	0.5	0.5	0.5	1.2	1.2
Subtotal	1.6	1.0	2.9	3.2	1.5	1.8	6.0	6.0
Escalation (1.06/year)	0.1	0.1	0.4	0.4	0.3	0.3	0.8	0.8
Total	1.7	1.1	3.3	3.6	1.8	2.1	6.8	6.8

3.10 PROJECT MANAGEMENT

The STX project will be managed according to the standard implemented by Martin Marietta Energy Systems. The scientist/engineer/manager team methods used on other Fusion Energy Division projects will be used on STX. The management goal will be to ensure that the technical, cost, and schedule objectives of the STX project are met.

Appendix A

STRUCTURAL DESIGN

OVERALL CONCEPT

The preliminary design of the coil support structure uses the following approach. A beam structure across the top and bottom of the tokamak reacts the forces from the S2, S3, S4, K, R, and D coils and the vertical in-plane and all out-of-plane loads from the TF coils. Radial inward TF coil forces are reacted by wedging the TF coil noses at the core of the tokamak. Radial outward TF coil forces are reacted by rings above the top TF coil leg and under the bottom TF coil leg. The overall structural concept is shown in Fig. A.1. An elevation view is shown in Fig. A.2.

STRUCTURE DETAILS

The external beam structure is shown in Fig. A.3. It consists of a top beam, a bottom beam, columns, and diagonal braces. The beams are side-by-side W14 $\times$ 61 steel beams. The mating flanges must be welded together to take the TF coil out-of-plane forces. The columns and diagonal braces are W6 $\times$ 25 steel beams.

Radially projecting plates are welded to the top and bottom beams to form an inter-coil structure. This structure mates with a system of TF coil support rings on top of and below the TF coil legs. This structural system is shown in Fig. A.4.

The TF coils must be attached to the TF support rings to react loads in the out-of-plane direction as well as loads in the vertical in-plane direction. The TF coils mate with the TF support rings as shown in Fig. A.5.

ORNL–DWG 85-2618 FED

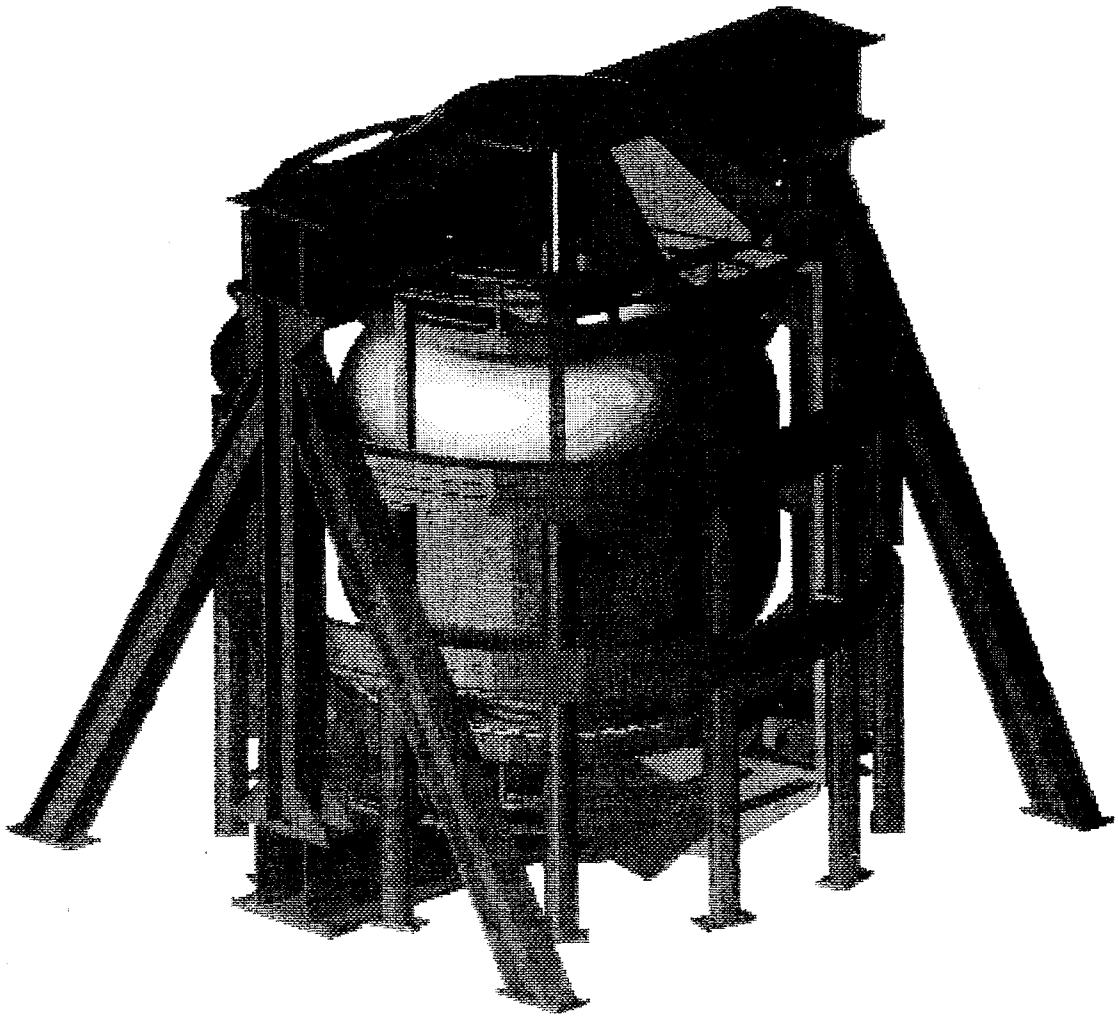

Fig. A.1. Artist's conception of STX.

A system of radially projecting plates mounted on a base plate forms a cradle support structure for the bottom S2, S3, and D coils. This cradle structure must be structurally attached to the bottom beam structure to transmit uplifting loads into the beam. The structure is shown in Fig. A.6. Bars placed over the coils and attached to the cradle by 0.5-in.-diam high-strength steel bolts restrain the coils to the cradle.

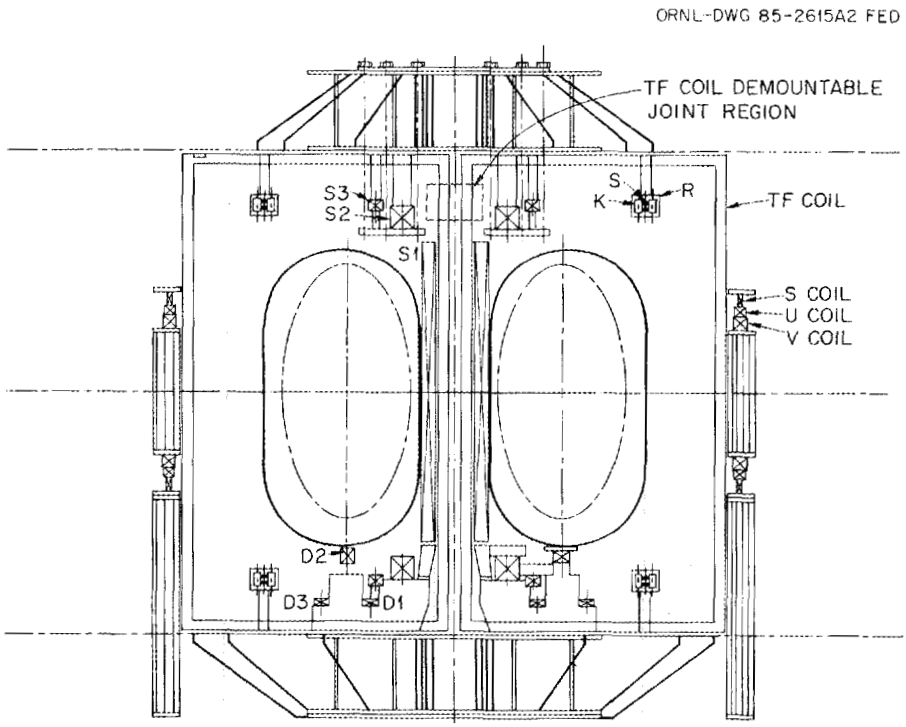

Fig. A.2. Elevation view of STX.

The support system for the K, R, D4, D5, and S4 coils consists of padded pedestal supports that are welded to the corresponding TF support ring immediately above or below these coils. A support ring composed of K, R, D4, D5, and S4 coils placed on top of (bottom) or on bottom of (top) the coil packs is bolted to the pad of the pedestals for support. This support system is shown in Fig. A.7.

The support system for the top S2 and S3 PF coils consists of an S2/S3 support ring, bar pedestals attached to the inner top TF support rings, and 1⅛-in.-diam tension rods that screw into the S2/S3 support ring, run through the top intercoil structure, and are bolted on top. The system is shown in Fig. A.8. Figure A.9 is a close-up view of the inner top TF support ring with the welded plate pedestals.

ORNL-DWG 85-2614 FED

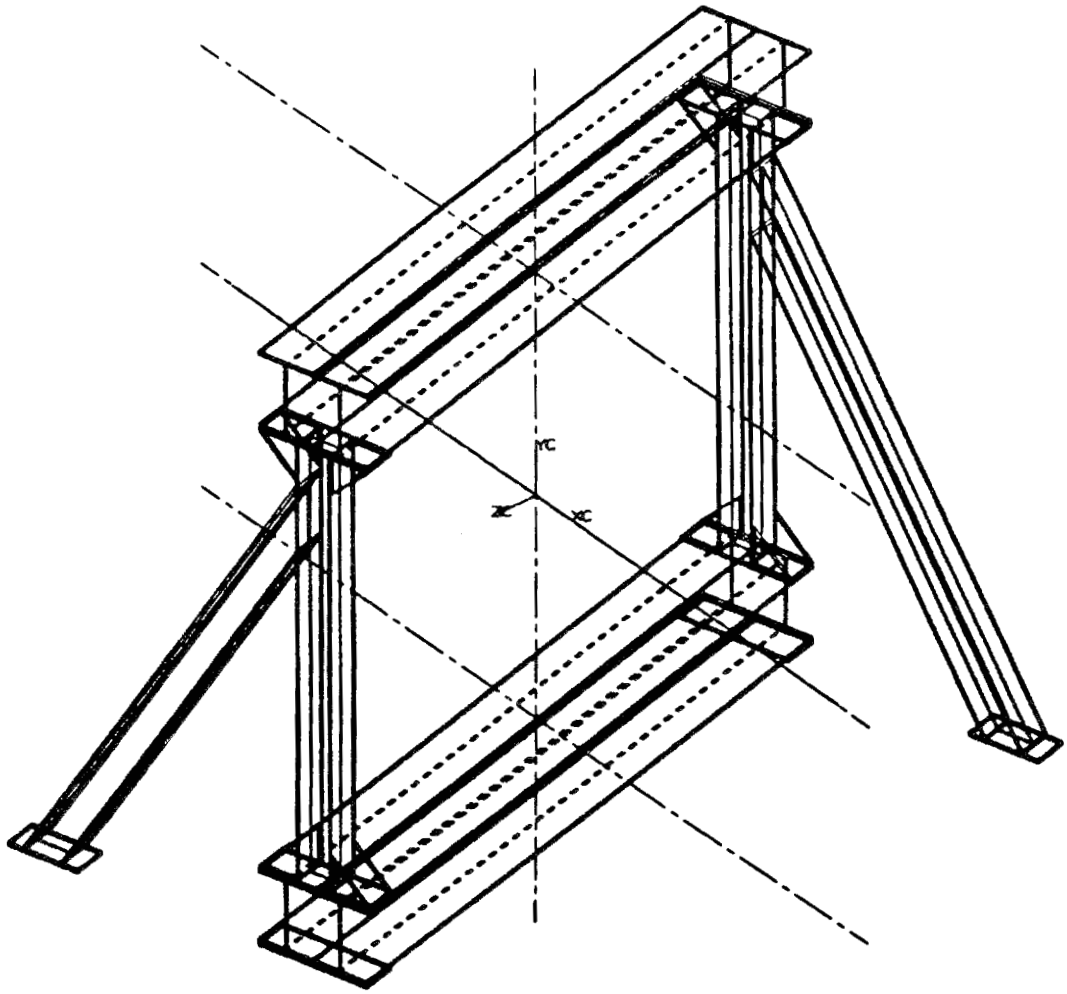

Fig. A.3. STX external beam structure.

The support system for the S5 and V coil system consists of 12 column pedestal supports (see Fig. A.10). There is an upper set and a lower set of columns. The columns are 4-in.-diam, extra-strong, stainless steel pipes. A structural tie between the bottom and upper column sets is required since the upper coil pack could have a net force upward for certain combinations of energized coils.

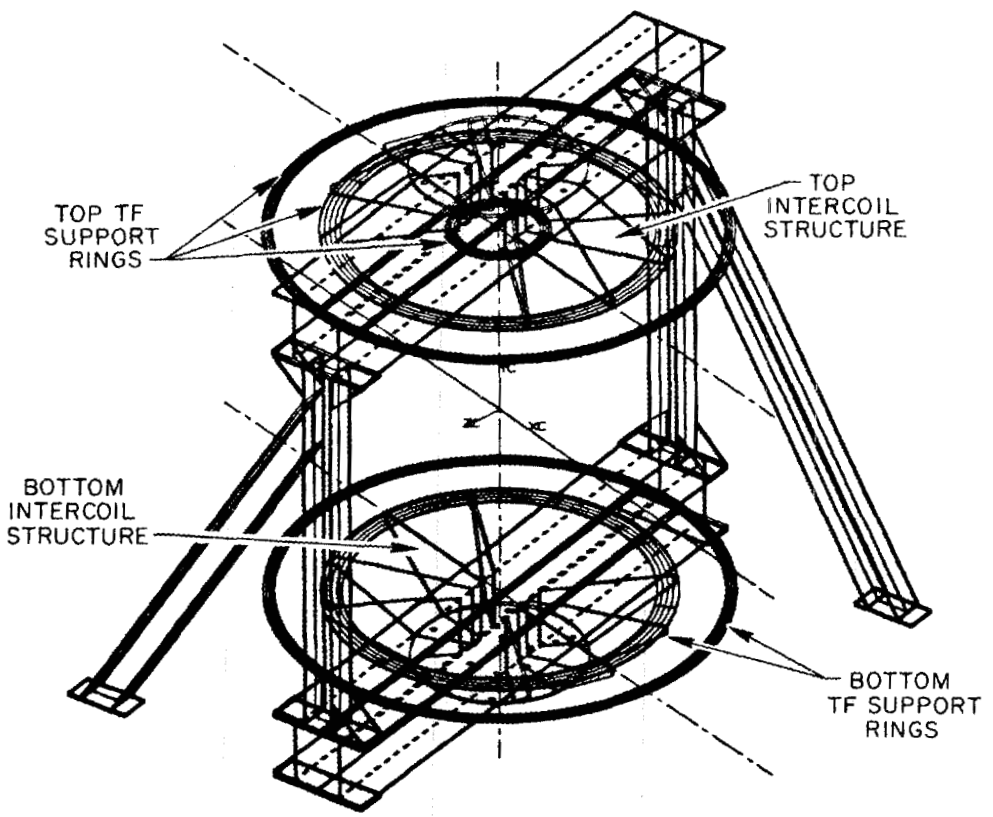

Fig. A.4. STX support structure.

FLOOR SUPPORT FRAME

Alignment of the STX midplane with the centerline of the High Power Test Facility required mounting the STX and its previously described support structure 1.73 m (5 ft 8 in.) above the existing floor level. Relative component locations are shown in Fig. A.11. A floor support structure, not yet determined, will be required to mount the STX assembly in this elevated location. This framework assembly will carry all resultant magnetic loads and all gravity loads down to floor level. The structure will allow maximum access to the bottom of the STX machine.

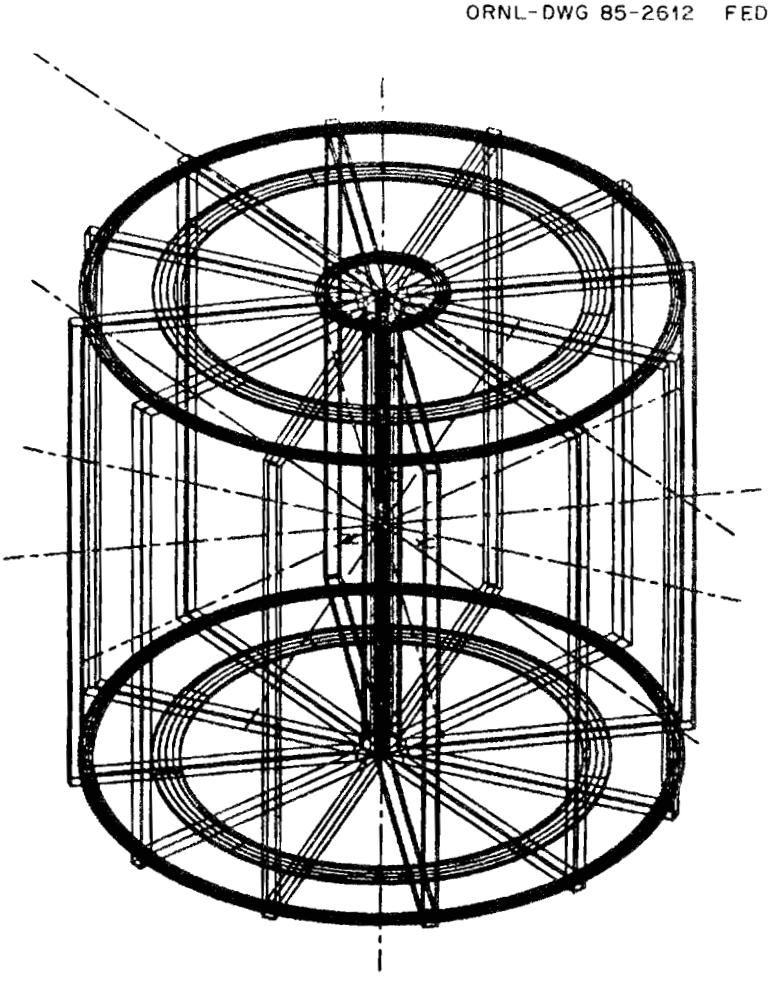

Fig. A.5. TF coil support structure.

ORNL-DWG 85-2611 FED

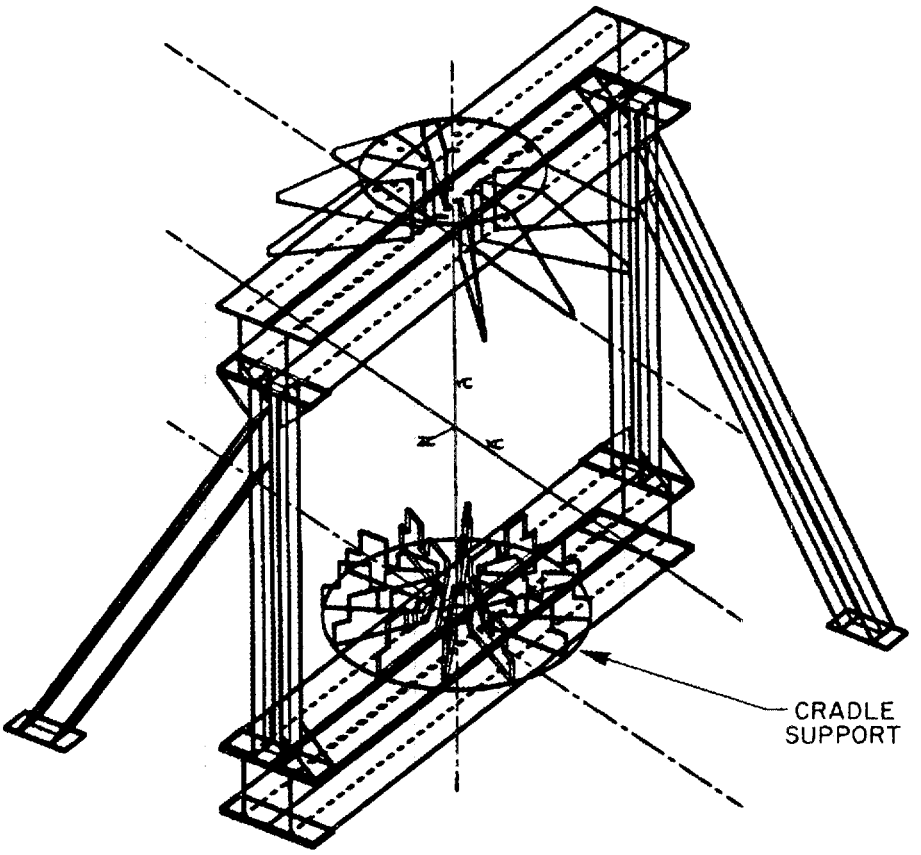

Fig. A.6. S2, S3, and D coil cradle support structure.

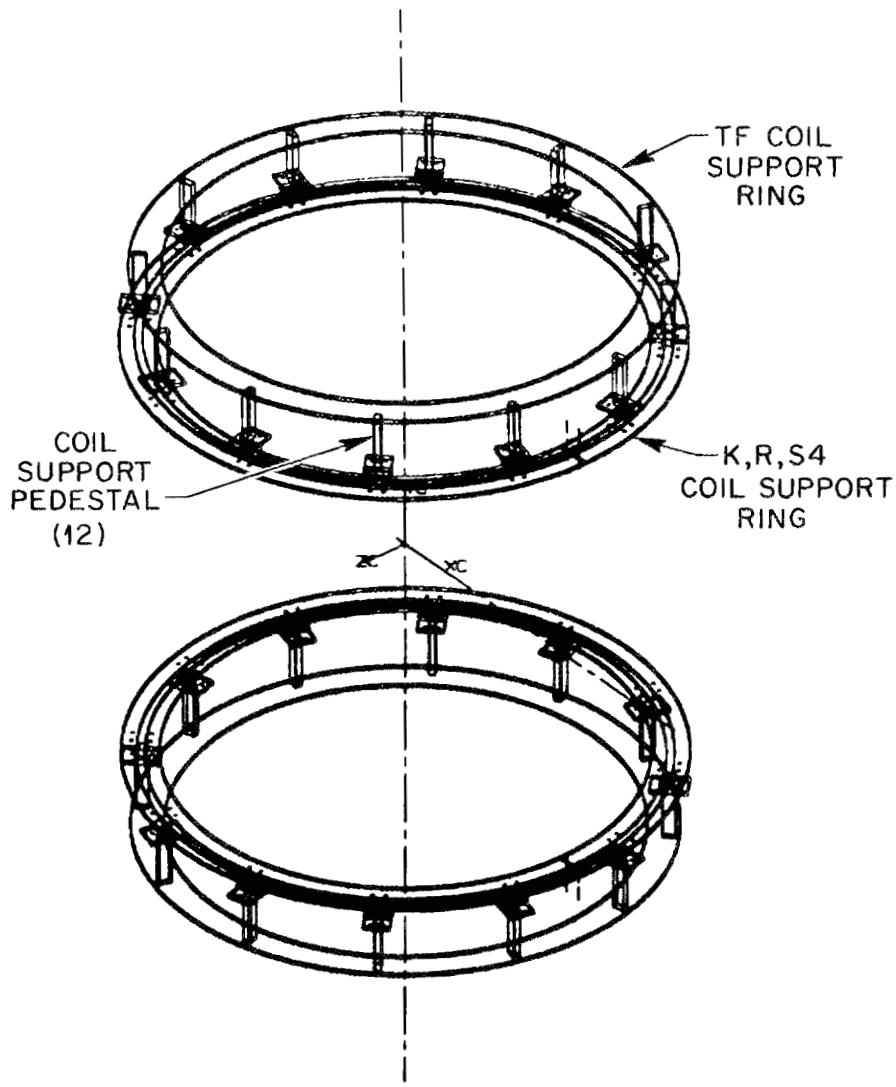

Fig. A.7. K, R, and S4 coil support structure.

ORNL-DWG 85-2609 FED

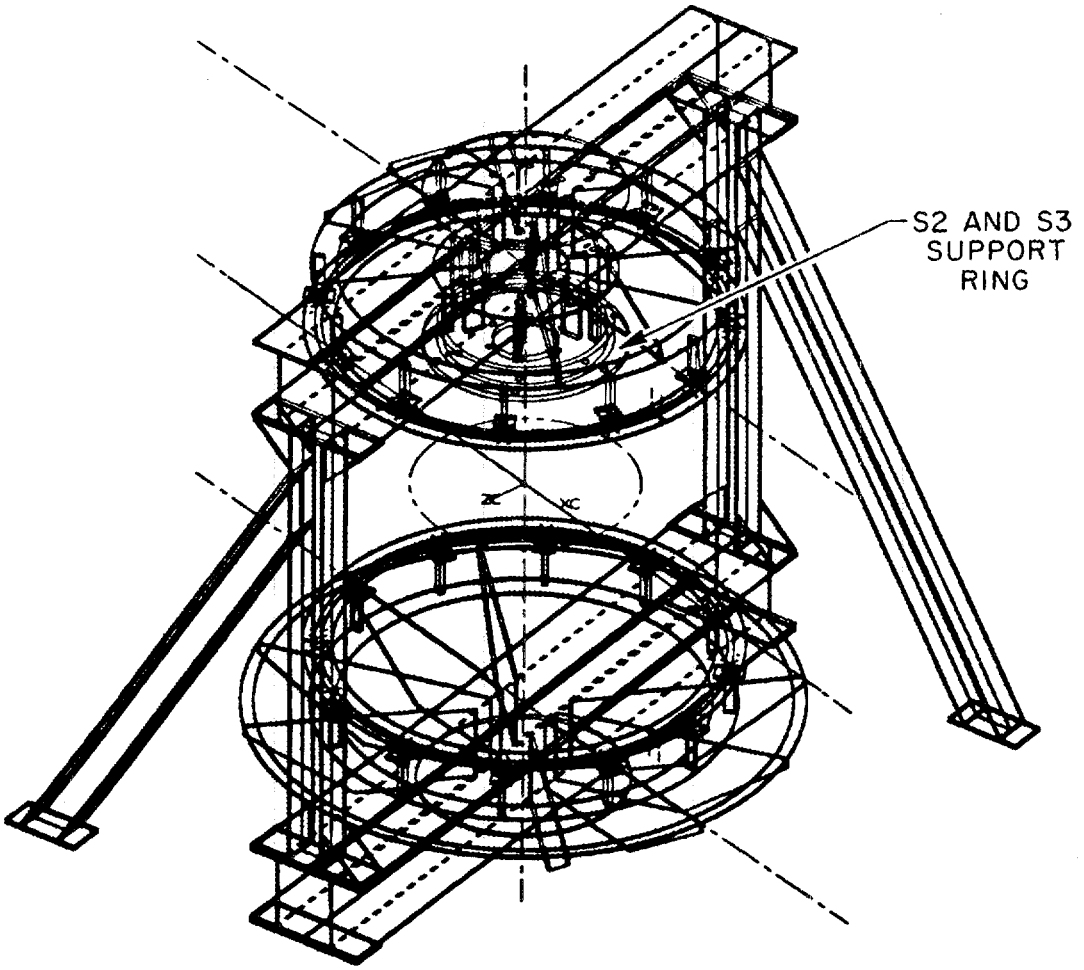

Fig. A.8. S2 and S3 coil support structure.

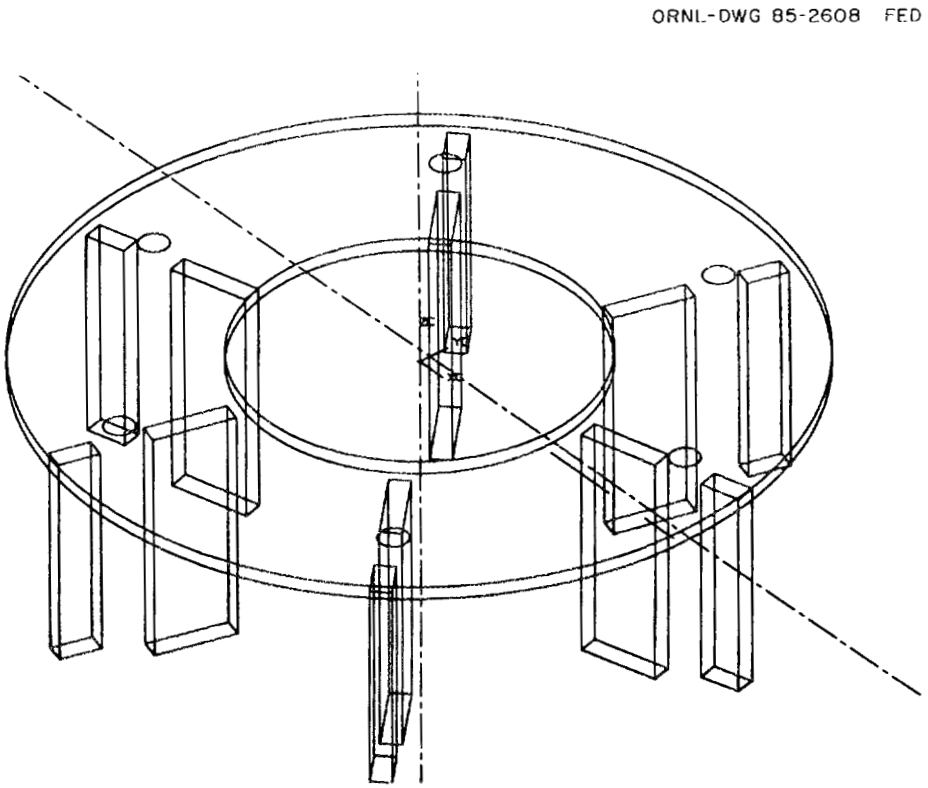

Fig. A.9. Top TF coil support ring with PF coil support pedestals.

ORNL-DWG 85-2607 FED

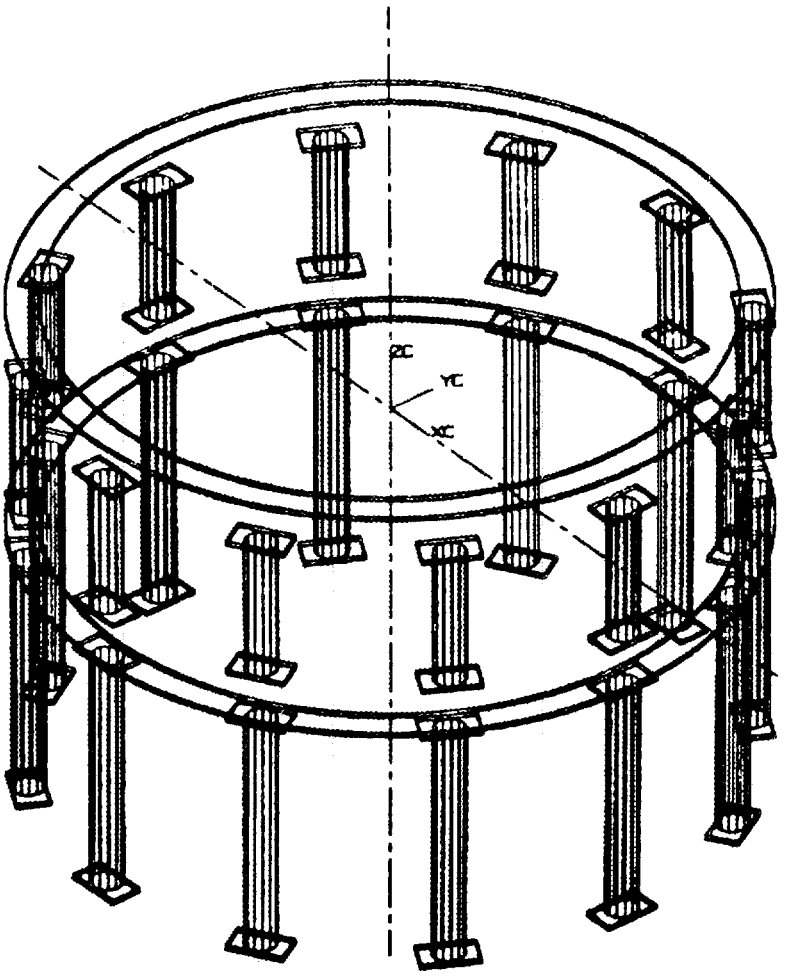

Fig. A.10. S5, U, and V coil support structure.

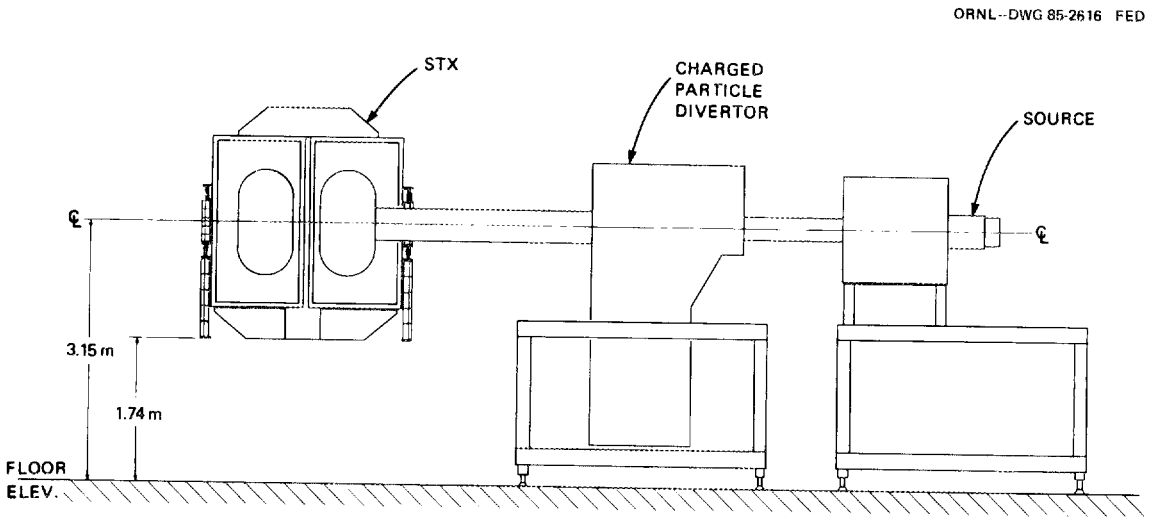

Fig. A.11. Component locations.

Appendix B

THERMAL ANALYSIS

The pulsed electrical heating and water cooling of the coils proposed for use in STX have been examined to determine whether the designs are acceptable given the high temperature rise in the copper and the need for many cycles of heating and cooling.

STATEMENT OF PROBLEM

All of the coils (OH, TF, and PF) are heated with short pulses lasting roughly 1 s. The OH and PF coils see a sawtooth current pulse that ramps the current from 0 to full at 0.25 s, from full to negative full at 0.75 s, and then to 0 at 1.0 s. The effective full-power time is 0.33 s. The TF coils see a square wave pulse that goes rapidly from 0 to full current, stays at full current for 1.0 s, and then goes rapidly to 0. The effective full-power time is 1.0 s. The OH coil current density is very high—in the neighborhood of 20 kA per square centimeter of copper. The coils are all internally cooled with flowing water. Current pulses will be repeated many times at a rate of one pulse every 3 min.

SUMMARY OF RESULTS

The first critical parameter is the peak copper temperature reached at the end of the electrical pulse. The temperature increase is proportional to the square of the current density and the effective full-power duration of the pulse. For the OH coils, the increase is 60°C (75°C for copper alloy) for a current density of 20 kA/cm^2 with a sawtooth wave form. For the worst case, that of the PF coils with a current density of 7.5 kA/cm^2 and a 1-s sawtooth pulse, the temperature rise is 12°C. The temperature rise in the central leg of the TF coil with the 1-s flattop pulse and a current density of 10 kA/cm^2 is approximately 60°C.

The second critical parameter is the time for the water to be transported from inlet to outlet. For the OH coil with 16 hydraulic passages, each approximately 16 m long and connected in parallel, a pressure drop of 50 psi gives a flow rate of 1 m/s and a transit time of 16 s. This allows 11 transit times before the next pulse and thus permits adequate cooldown before the next heating cycle. The S2 PF coil, which is 2 m long and has a pressure drop of 10 psi, will have a velocity of 1 m/s and a transit time of 2 s, clearly adequate for a cycle every 180 s.

HAND CALCULATIONS

Hand calculations were made for several aspects of the problem.

Temperature Rise in Copper

If the heat transfer from the copper to the water is neglected, the temperature rise in the copper due to the electrical heating pulse is

$$\frac{dT(t)}{dt} = \frac{q'''(t)}{\rho c_p} = \frac{J^2(t)\Omega(T(t))}{\rho c_p} ,$$

where T is the temperature (°C), t is time (s), q''' is the heat input (W/cm^3), J is the current density (A/cm^2), Ω is the resistivity (Ω·cm), ρ is the density (g/cm^3), and c_p is the specific heat [J/(g·°C)]. If we neglect the cooling effect of the water and assume that $\Omega(T(t)) \simeq \Omega$(room temperature), then the temperature rise of the copper during the electrical pulse is

$$\frac{dT(t)}{dt} = \frac{J_{max}^2 \Omega t_{eff}}{\rho c_p} = \frac{(2 \times 10^4 \text{ A/cm}^2)^2(1.8 \times 10^{-6} \text{ }\Omega\text{·cm})(0.33 \text{ s})}{(8.9 \text{ g/cm}^2)[0.4 \text{ J/(g·°C)}]}$$

$$= 67°C$$

(or 87°C for the copper alloy case). The transfer of heat into the water and the heat capacity of the water will reduce the temperature rise in the copper by the ratio of the enthalpy change of the copper to that of the copper plus water. The adjusted estimate for the copper temperature rise is 60°C (75°C for the copper alloy case).

Copper Time Constant

It is useful to estimate the time for relaxation in space of copper temperatures τ_{Cu},

$$\tau_{Cu} = \frac{\rho C_p (\delta_r)^2}{k} = \frac{8.9 \times 0.4 \times (0.5)^2}{3.9} = 0.23 \text{ s} ,$$

where δ_r is the radial thickness of the copper (cm) and k is the thermal conductivity of the copper (W/cm·°C). Since this is less than the pulse time and much less than the cooldown time, it is reasonable to assume that the copper has a uniform temperature along the radial axis. The temperature is allowed to vary along the z-axis, but the heat loss along this dimension is assumed to be very small compared to that through the copper/water film into the water because of the very small temperature gradient along the very long dimension (the z-axis).

Transport Across Copper/Water Film

The time constant for heat transport from copper into water across the film is approximately

$$\tau_{film} \simeq \frac{A_{Cu} \rho_{Cu} C_{p,Cu}}{2 R_w h_{film}} = \frac{1.0 \times 8.9 \times 1.0}{2 \times 0.4 \times 2.27} = 4.9 \text{ s} ,$$

where A_{Cu} is the cross-sectional area of the copper normal to the z-axis (cm^2), R_w is the

radius of the cooling water channel (cm), and h_{film} is the film heat transfer coefficient from copper to water ($W/cm^2 \cdot °C$). It can be seen that τ_{film} is much longer than τ_{Cu} and much shorter than the time for fluid to be transported from inlet to outlet, $\tau_{transport}$.

Coolant Transport Time

The time constant for transport of water from the inlet to the outlet is

$$\tau_{transport} = \text{length of coolant path/coolant velocity} .$$

If the OH solenoid is wound with 16 windings connected hydraulically in parallel, each path is roughly 1600 cm long. With a velocity of 1 m/s (attainable with a pressure drop of 100 psi), the value of $\tau_{transport}$ is

$$\frac{1600 \text{ cm}}{100 \text{ cm/s}} = 16 \text{ s} .$$

This is longer than τ_{Cu} and τ_{film}. The transport time gives a measure of the time allowed for $(T_{Cu} - T_{in})$, where T_{Cu} is the temperature of the copper and T_{in} is the inlet coolant temperature, to fall by a factor of e. Because the ratio of the heat capacity of copper to that of water is roughly 10:1, water will have to flow through the copper for $(10–20)\tau_{transport}$ to cool the copper and water to the starting temperature. The value calculated here, 16 s, allows 11 transport times between pulses, which is sufficient to allow cool-down to the inlet water temperature between pulses.

COMPUTER CALCULATION OF TEMPERATURE RISE

A computer code was used to calculate the temperature rise of the copper. The electrical resistivity and heat capacity of copper were represented as piecewise linear functions of the copper temperature; the actual values are presented in Table B.1. Table B.2 presents data for the current pulses used in the code, and Table B.3 presents results from the code, which are plotted in Figs. 3.1.9 and 3.1.10. All calculations were made for copper alloy with a thermal and electrical conductivity 80% that of pure copper.

Table B.1. Data for copper properties

```
The data for the various linearly interpolated functions is as follows.

Specific heat of copper or alloy, J/(kg K)
Cp Cu    =  (  0.00,  5.0,  40.0,  235.0,  350.8,  380.0,  415.0);
Temp, K  =  ( 000.0, 15.0,  30.0,  100.0,  200.0,  300.0,  500.0);

Electrical resistivity of pure copper, micro ohm cm.
omega    =  (  0.00,   0.30,   2.80,   3.54,   3.35,   5.50);
Temp, C  =  (-270.0, -200.0,  200.0,  300.0,  400.0,  500.0);
```

Table B.2. Data for current pulses

```
The following data is for current pulse shape in the OH and PF coils.
This is a 1 sec. saw toothed pulse.
g_of_t   =  (  0.00,   1.00,  -1.00,   0.00 )
time,sec =  (  0.00,   0.25,   0.75,   1.00 )
```

For this case, the electrical heating will increase by 1/0.8 and the temperature will be 1.25 times higher than that in pure copper. All of the time constants will remain unchanged to a good approximation.

Table B.3. Computer results for OH coil with sawtooth pulse

```
   20.00          { Water Volume, %
   70.00          { Cu Volume, %
    1.58          { Cell area, cm2
 1600.00          { Cu length, cm
  100.00          { Water pressure drop, psi
20000.00          { Cu current density, Amps/cm2
    0.80          { Cond eff./Cu
    0.05          { time step1, sec
    5.00          { time step2, sec
    1.00          { time to change time steps
  180.00          { recycle time
    1.00          { number of cycles
   20.00          { inlet temperature, C
  153.20          { Coolant vel, cm/sec.

 Temperatures for points in:
 w Cu   w Cu   w Cu   w Cu   w Cu   w Cu   w Cu   w Cu   w Cu    w Cu    w Cu
Time = 0 to 1.0 sec in steps of 0.1 sec.
20 20, 20 21, 20 30, 20 50, 20 59, 20 59, 20 59, 20 68, 20 89, 20  98, 20  97
20 20, 20 21, 20 30, 23 51, 26 60, 29 60, 31 61, 34 70, 38 92, 42 101, 46 101
20 20, 20 21, 20 30, 23 51, 27 60, 30 60, 33 61, 36 70, 41 92, 47 102, 52 102
20 20, 20 21, 20 30, 23 51, 27 60, 30 60, 33 61, 37 70, 42 92, 48 102, 54 102
20 20, 20 21, 20 30, 23 51, 27 60, 30 60, 33 61, 37 70, 42 92, 48 102, 54 102
20 20, 20 21, 20 30, 23 51, 27 60, 30 60, 33 61, 37 70, 42 92, 48 102, 54 102
20 20, 20 21, 20 30, 23 51, 27 60, 30 60, 33 61, 37 70, 42 92, 48 102, 54 102
20 20, 20 21, 20 30, 23 51, 27 60, 30 60, 33 61, 37 70, 42 92, 48 102, 54 102
20 20, 20 21, 20 30, 23 51, 27 60, 30 60, 33 61, 37 70, 42 92, 48 102, 54 102
20 20, 20 21, 20 30, 23 51, 27 60, 30 60, 33 61, 37 70, 42 92, 48 102, 54 102
20 20, 20 21, 20 30, 23 51, 27 60, 30 60, 33 61, 37 70, 42 92, 48 102, 54 102

Time = 6 to 56 sec. in steps of 5 sec.
20 46, 20 28, 20 22, 20 20, 20 20, 20 20, 20 20, 20 20, 20 20, 20 20, 20 20
43 63, 33 43, 27 33, 24 27, 22 23, 21 22, 20 21, 20 20, 20 20, 20 20, 20 20
59 74, 47 56, 37 43, 30 35, 26 29, 24 25, 22 23, 21 22, 20 21, 20 20, 20 20
69 80, 58 66, 47 53, 38 43, 32 36, 28 30, 25 27, 23 24, 22 22, 21 21, 20 21
75 84, 67 73, 56 62, 46 51, 39 43, 33 36, 29 31, 26 27, 24 25, 22 23, 21 22
79 87, 73 78, 64 69, 54 59, 46 50, 39 43, 33 37, 29 32, 26 28, 24 26, 23 24
82 88, 78 82, 70 74, 61 66, 53 57, 45 49, 39 42, 34 37, 30 32, 27 29, 25 26
83 89, 82 84, 75 78, 67 71, 59 63, 51 55, 45 48, 39 42, 34 37, 30 32, 27 29
84 90, 84 86, 79 81, 72 75, 65 68, 57 61, 50 54, 44 47, 39 42, 34 37, 31 33
85 90, 86 87, 82 84, 76 79, 70 73, 63 66, 56 59, 49 53, 44 47, 38 41, 34 37
85 91, 87 88, 84 85, 80 82, 74 77, 68 71, 61 64, 55 58, 49 52, 43 46, 38 41

Time = 61 to 136 sec in steps of 10 sec.
20 20, 20 20, 20 20, 20 20, 20 20, 20 20, 20 20, 20 20
20 20, 20 20, 20 20, 20 20, 20 20, 20 20, 20 20, 20 20
20 20, 20 20, 20 20, 20 20, 20 20, 20 20, 20 20, 20 20
20 20, 20 20, 20 20, 20 20, 20 20, 20 20, 20 20, 20 20
21 21, 20 20, 20 20, 20 20, 20 20, 20 20, 20 20, 20 20
22 22, 20 21, 20 20, 20 20, 20 20, 20 20, 20 20, 20 20
23 24, 21 22, 20 20, 20 20, 20 20, 20 20, 20 20, 20 20
25 26, 22 23, 21 21, 20 20, 20 20, 20 20, 20 20, 20 20
28 29, 24 25, 22 22, 21 21, 20 20, 20 20, 20 20, 20 20
31 33, 26 27, 23 24, 21 22, 20 20, 20 20, 20 20, 20 20
34 36, 28 30, 24 25, 22 23, 20 21, 20 20, 20 20, 20 20
```

Appendix C

FINITE ELEMENT ANALYSIS OF THREE VACUUM VESSEL MODELS

INTRODUCTION

A finite-element analysis was performed on three simple models of the STX vacuum vessel to determine element stresses due to static loads and elastic stability. The models varied in thickness from 0.0625 to 0.25 in. on the inner and outer cylindrical surfaces. This summary describes the finite-element models, their analysis, and results, which are compared to an analytic solution for a simpler geometry.

MODEL DESCRIPTION

A finite-element model with dimensions shown in Fig. C.1 was constructed using the analysis preprocessor program PATRAN-G on a VAX 11/780 computer. An external pressure of 2 atm was applied, and the model was constrained at four nodes to keep it from wandering during solution (Fig. C.2). Element thickness was assigned for three cases, as shown in Table C.1. An MSC/NASTRAN input deck was created from the PATRAN-G data base, and a rigid format-5 solution for statics and elastic buckling was employed.

STATICS SOLUTION

The Von Mises distortion stresses are plotted for the three model cases in Figs. C.3–C.5. For the baseline case of model III, the peak Von Mises stress was 7380 psi. Hoop

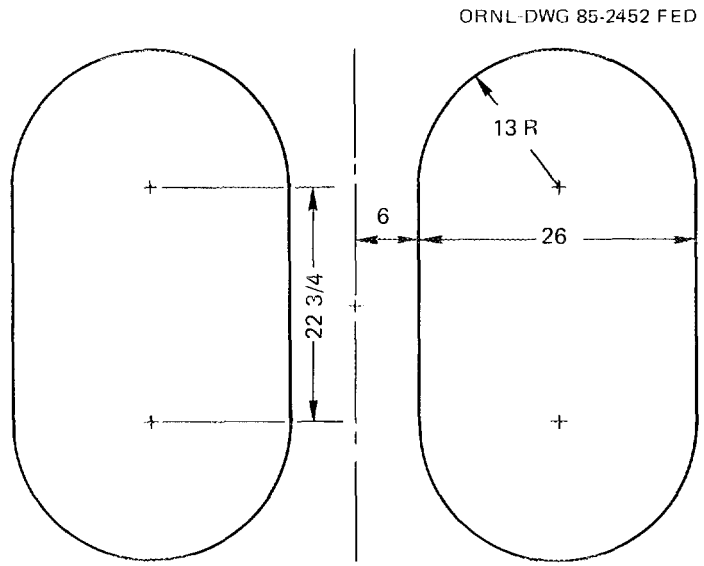

Fig. C.1. Vacuum vessel dimensions (all dimensions in inches).

stresses ranged from 1517 psi on models I and III to 3106 psi on model IV. Longitudal stresses varied from 7,280 psi compression in model I to −6,630 psi in model III and −13,055 psi in model IV. The statics solution produced low stresses for all cases.

EIGENVALUE SOLUTION

A buckling solution of the three models produced the factors for determining critical pressure shown in Table C.2. A deformed shape with a maximum deflection of 1 in. is shown for each case in Fig. C.6. Models I and IV failed in the outer cylindrical section, while model III, with a thicker inside column than model IV, buckled in the dome region.

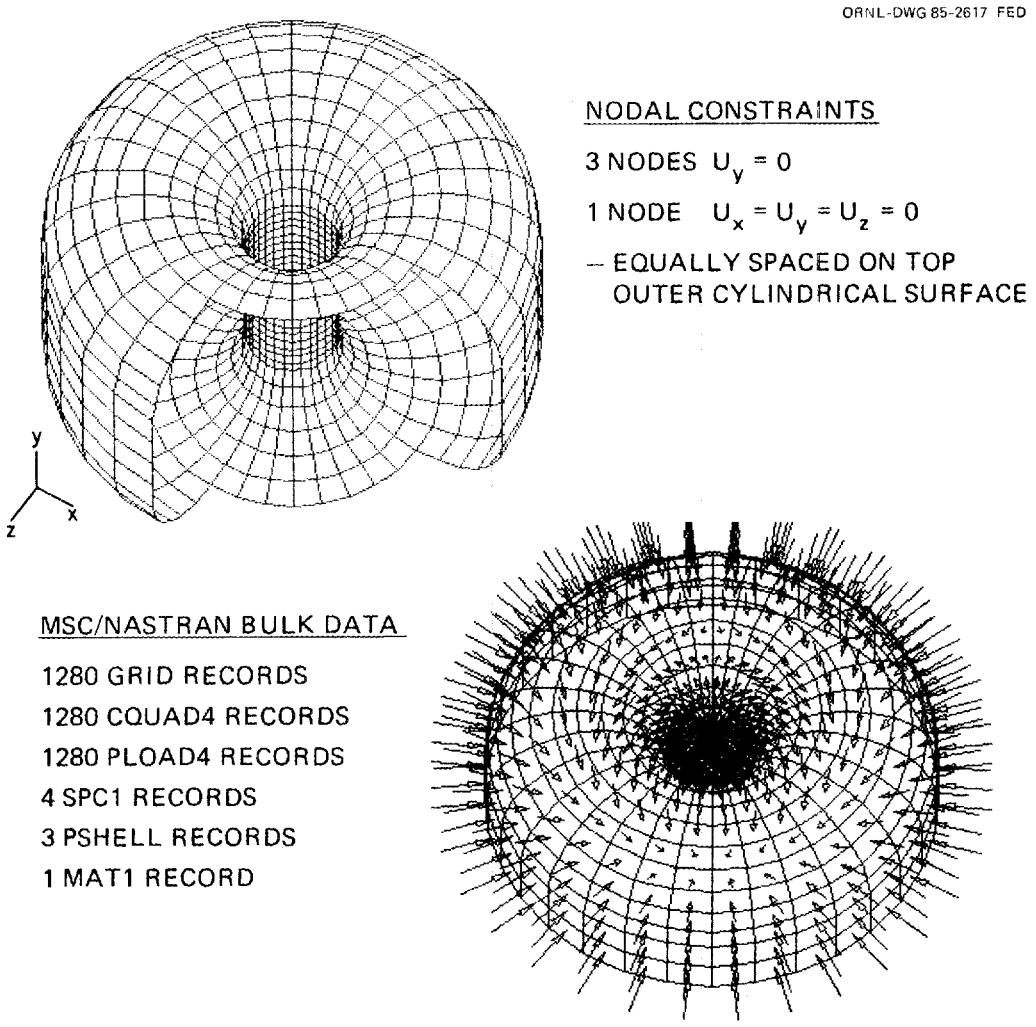

Fig. C.2. Finite element model.

Table C.1. Differences in models

Region	Element thickness		
	Model I	Model II	Model III
Outer cylindrical section	0.125	0.250	0.250
Inner cylindrical section	0.125	0.125	0.0625
Upper/lower dome	0.125	0.125	0.125

ORNL–DWG 85-2787 FED

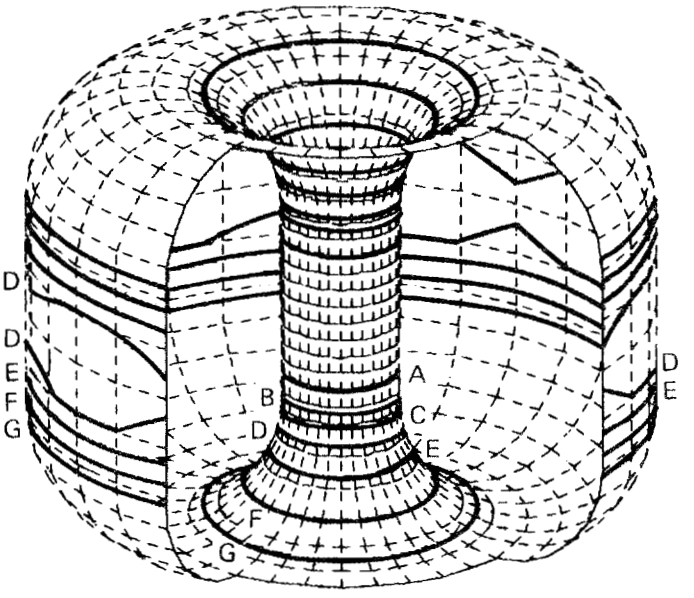

A = 4000
B = 3500
C = 3000
D = 2500

E = 2000
F = 1500
G = 1000

Fig. C.3. Model I Von Mises stress contours for 30 psi.

ORNL–DWG 85-2788 FED

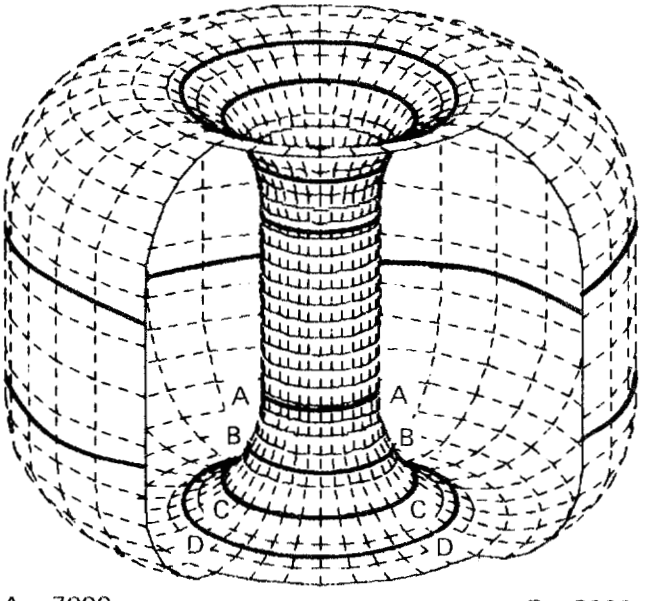

A = 7000
B = 6000
C = 5000
D = 4000

E = 3000
F = 2000
G = 1000

Fig. C.4. Model III Von Mises stress contours for 30 psi.

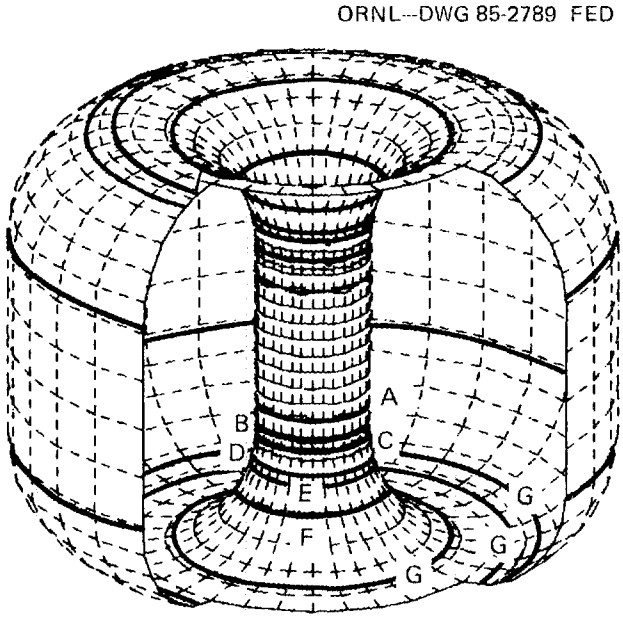

Fig. C.5. Model IV Von Mises stress contours for 30 psi.

Table C.2. Factors for determining critical pressure

Model	Eigenvalue	Critical pressure (psi) (Eigenvalue × 30)
I	1.279	38.4
III	8.001	240.0
IV	8.079	242.4

These results can be explained by the difference in distribution of normal and shear stresses between models III and IV. The small difference in critical pressure, however, suggests that the dome and cylindrical regions in both models had reached the elastic limit.

ANALYTIC COMPARISON

An expression for the critical external pressure on a cylinder with capped ends is plotted for two thickness-to-radius ratios in Figs. C.7 and C.8. For the length-to-radius ratio of the outer cylindrical surface of the vacuum vessel, the minimum critical pressure is 40 psi

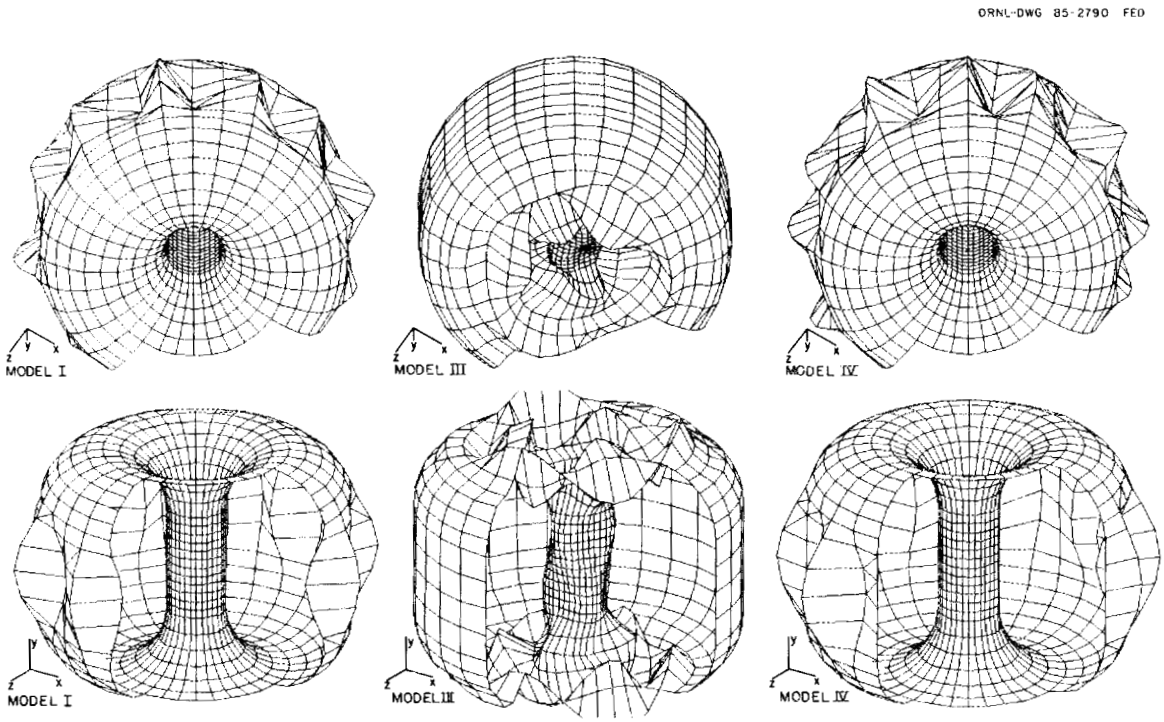

Fig. C.6. Deformed shapes for vacuum vessel models.

when $t = 0.125$ in. and 240 psi when $t = 0.250$ in. The number of lobes formed by buckling of the tube is 12 in both cases. These results agree closely with the finite-element analysis.

CONCLUSION

Models III and IV met the pressure requirement with a suitable factor of safety on buckling. Stress levels were acceptable in both cases. Selection of either design is supported by this analysis, but further study is needed to determine the effect of ports and supports on the structure.

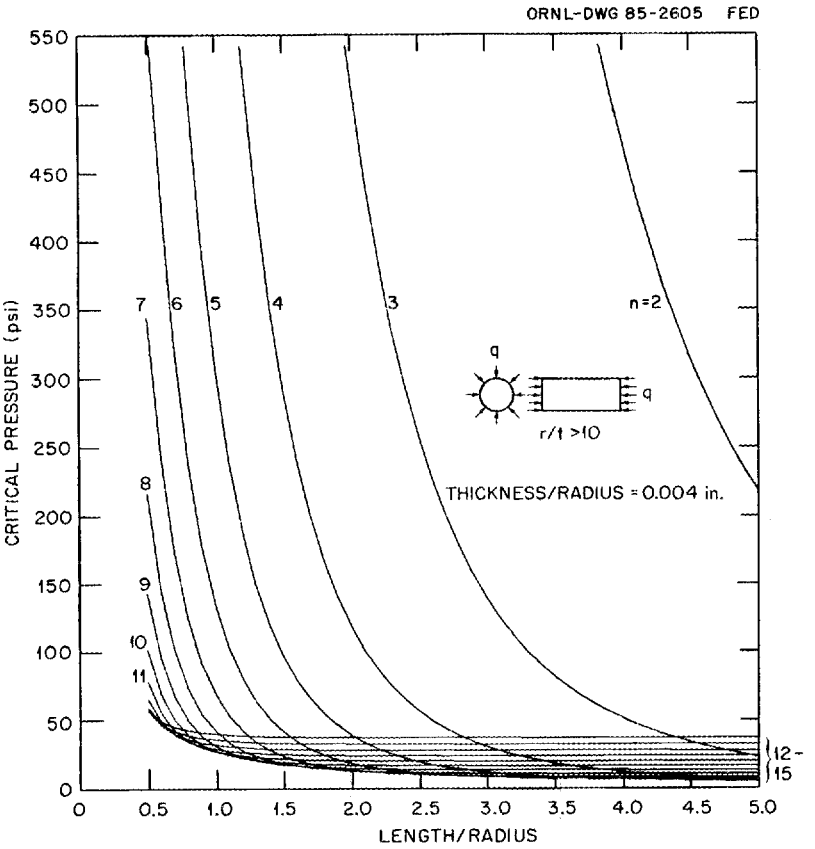

Fig. C.7. Analytic prediction of critical pressure (thickness/radius = 0.004).

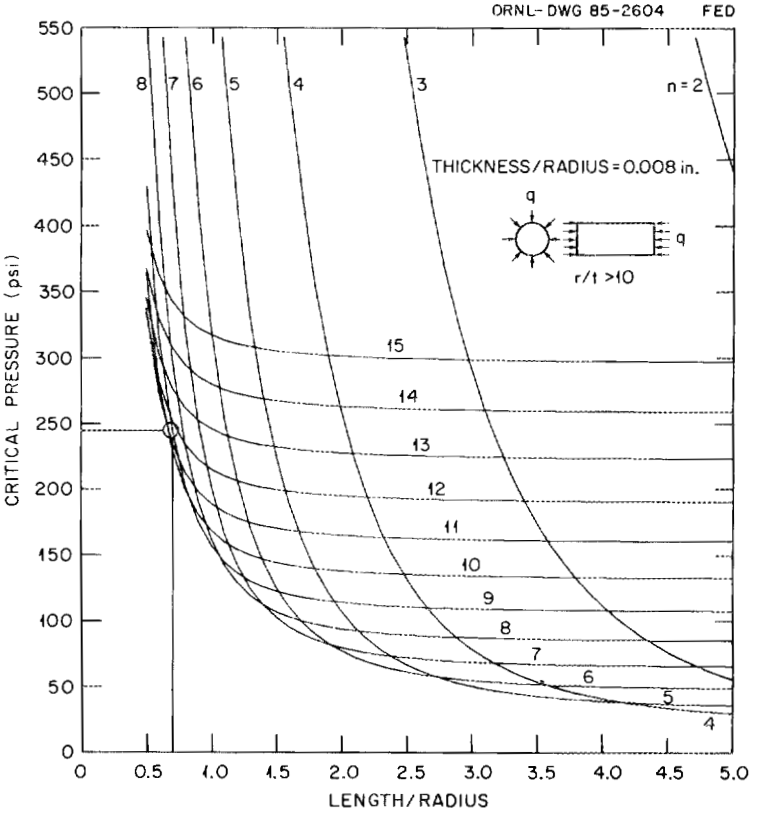

Fig. C.8. Analytic prediction of critical pressure (thickness/radius = 0.008).

Appendix D

FATIGUE ANALYSIS: DESIGN LIFE FOR STRESSING COPPER WINDINGS

INTRODUCTION

In this section, we determine the design life for stressing copper windings; we make this determination using two different sets of circumstances. First, we examine the copper windings from 0- to 20,000-psi tension, under nominal stress. Second, we examine the windings from 0- to 20,000-psi tension in the presence of the following theoretical strain concentration factors: (1) $K_T = 2.0$ and (2) $K_T = 4.0$. We examine three alloys: (1) fully annealed OFHC copper, (2) half-hard OFHC copper, and (3) CDA-182 copper.

Before we begin, however, we first obtain Goodman diagrams for each of the alloys (see Table D.1). Then we construct Manson curves for the alloys using the Manson equation:

$$\Delta\epsilon = \frac{3.5\,F_{TU}}{E} N_f^{-0.12} + D^{0.6} N_f^{-0.6} \quad , \tag{D.1}$$

where $D = \ln [100/(100 - \text{RA})]$, N_f is the number of cycles to failure for $R = 0$, $R = \sigma_{min}/\sigma_{max}$, $A = \sigma_A/\sigma_M$, $E\Delta\epsilon = 2\sigma_A$, and σ_A = stress amplitude (see Fig. D.1).

Table D.1. Properties of copper alloys

Alloy	F_{TU} (ksi)	RA 90	E 10^6	Neuber number	Static yield (ksi)
Annealed OFHC	32	91	17	0.005	10[a]
Half-hard OFHC	40	76	17	0.003	32[a]
CDA-182	58	65	17	0.002	52[a]

[a]0.005 strain offset.

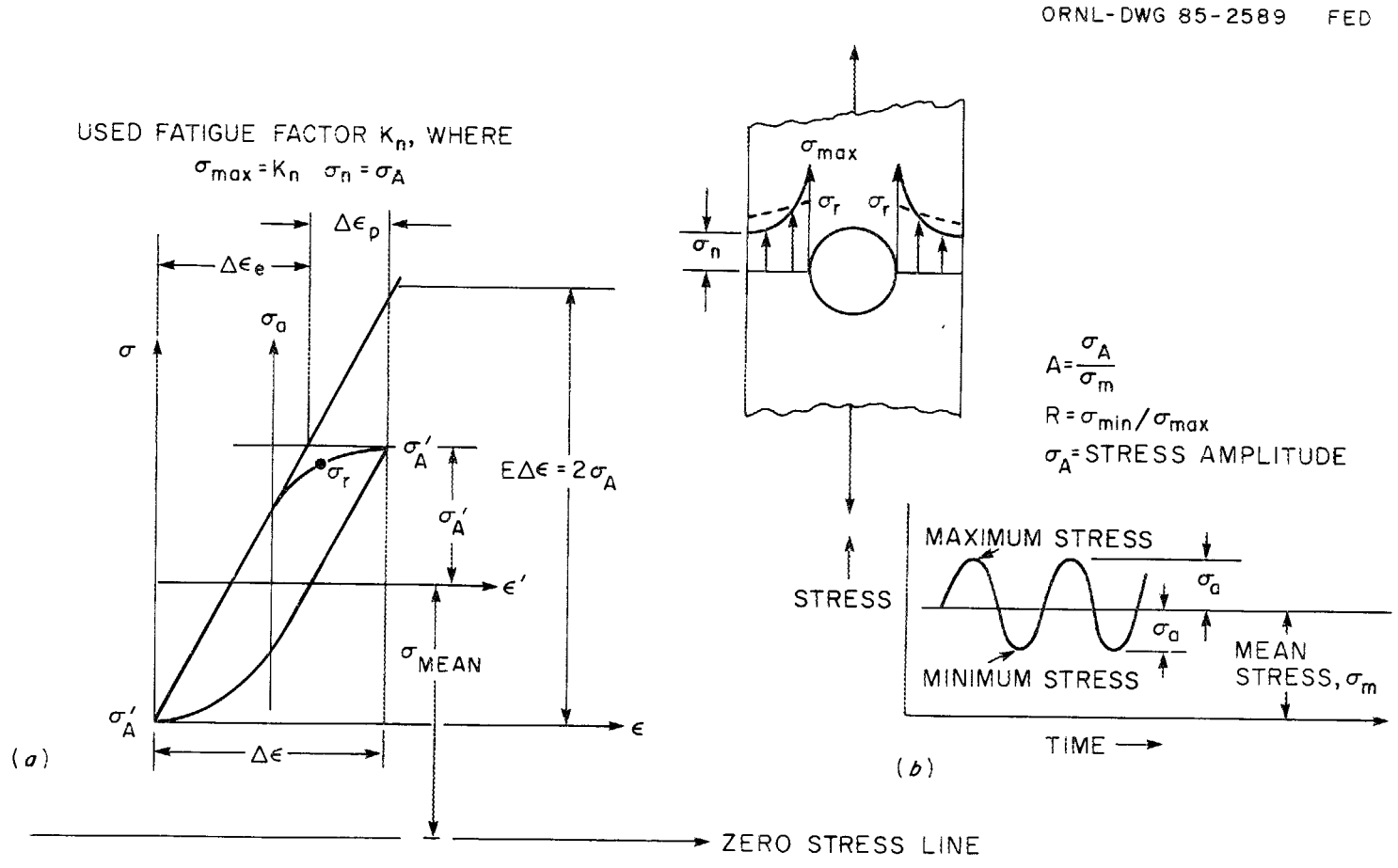

Fig. D.1. Stress calculation parameters.

As in Fig. D.1, $\sigma_A = E\Delta\epsilon/2$, or

$$\sigma_A = 1.75\, F_{TU} N_f^{-0.12} + \frac{E D^{0.6} N_f^{-0.6}}{2} \quad . \tag{D.2}$$

We then plot Eq. (D.2) for the three alloys in Fig. D.2. Some stress-controlled data are also plotted in Fig. D.2.

STRESS ANALYSIS

Since the design objective for the copper windings and joints will be to ensure safe operation for a certain required number of stress cycles (with the machine current pulsed, and each pulse representing one stress cycle), the goal is to determine the number of stress

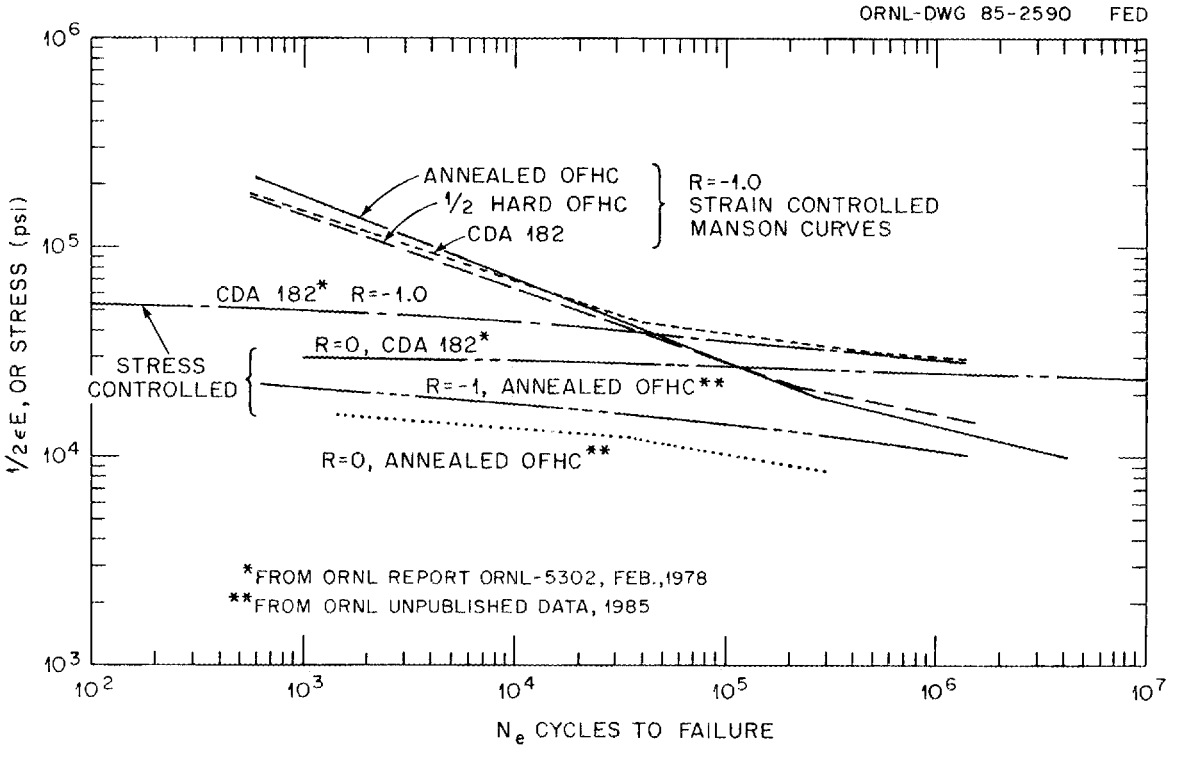

Fig. D.2. σ_A for annealed OFHC copper, half-hard OFHC copper, and CDA 182.

cycles (pulses) required to produce fatigue failure. General or gross yielding will not be considered failure.

Analysis of Fully Annealed OFHC Copper

From 0- to 20,000-psi tension in windings, we observe the following behavior in fully annealed OFHC copper. Consider Fig. D.3 and notice how the initial stress cycle will cause gross yielding of the annealed copper. In fact, the first half of a stress cycle will cause a plastic strain of more than 0.06 in. per inch, but no failure will take place. Notice in Fig. D.3, however, how the copper will strain harden, and after 10^4 cycles the stress-strain curve will stabilize.

Figure D.4 illustrates that at 20,000 psi the strain would only be 0.005 after 10^4 cycles, as compared with 0.06 on the virgin soft material. To apply strain concentration factors, K_n, we must know what the strain range (Fig. D.3) will be in this 0- to 20,000-psi (engineering stress) stress range. If we look at Fig. D.2 [(for annealed OFHC) for $R = 0$

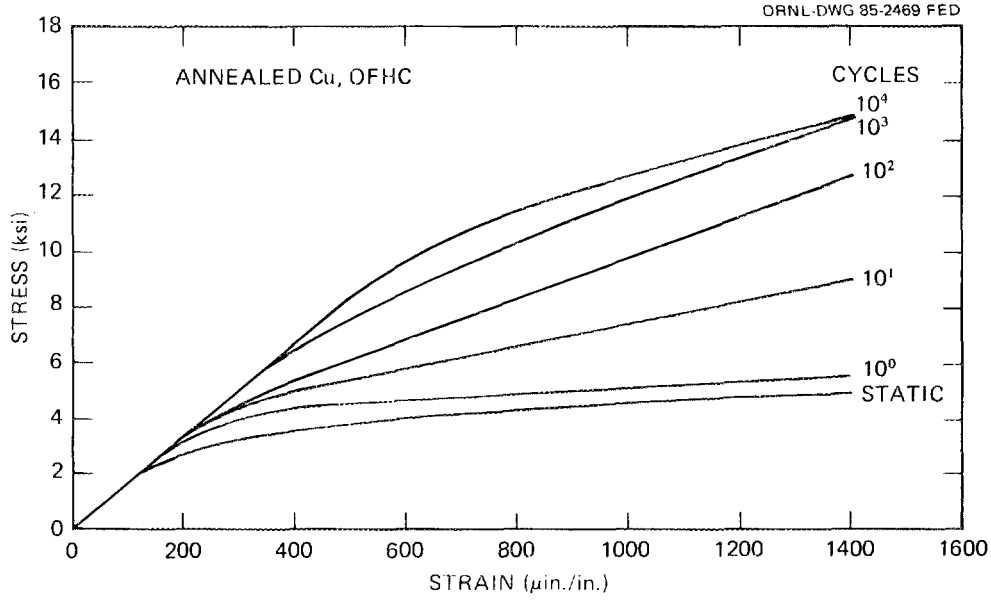

Fig. D.3. Stress vs strain for annealed OFHC copper.

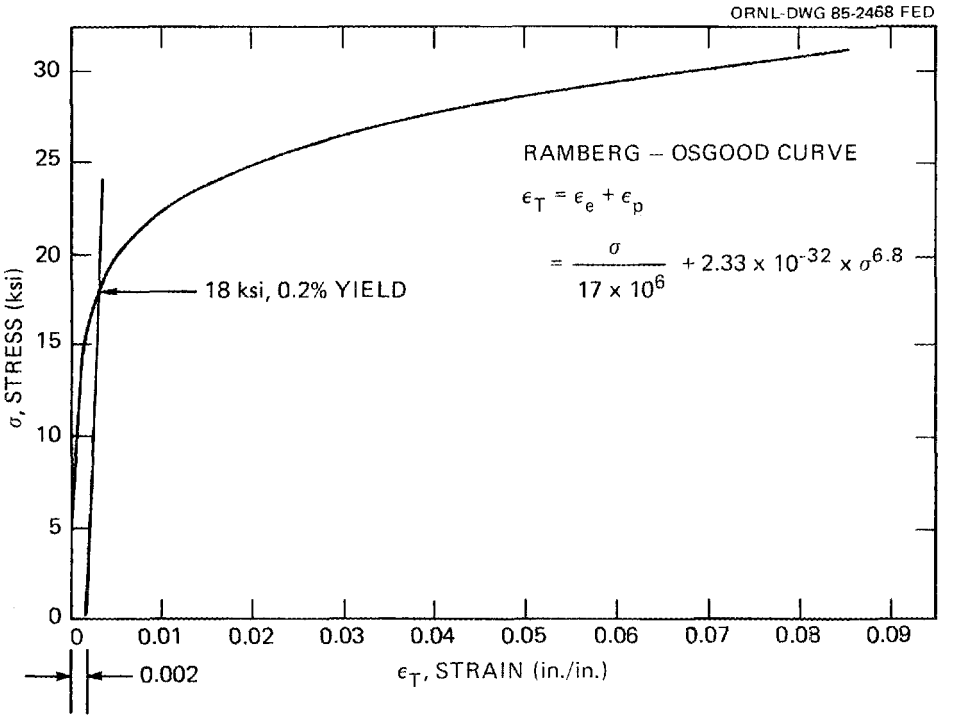

Fig. D.4. Ramberg-Osgood curve.

and σ_A = 10,000 psi], the fatigue cycles to failure would be 110,000 cycles. The Manson curve for $R = -1.0$ gives an equivalent σ_A (see Fig. D.1) of 27,500 psi for 110,000 cycles. We put these values on a Goodman diagram, as shown in Fig. D.5. For a mean stress of 10,000 psi, the Goodman diagram gives a σ_A stress of 19,000 psi. Now we show the cyclic stress diagram (similar to Fig. D.1) in Fig. D.6(a). The strain range is 0.00224 per stress cycle. The design life is 110,000/10 or 11,000 cycles (a safety factor of 10 on life is about 1.5 on stress).

Stress Concentration Factor of $K_t = 2$

If we use stress-controlled fatigue data, generally we do not know what K_n factor to use, since K_n will vary with N_f. However, if strain-controlled data are used, K_n is constant with N_f [see Fig. D.7]. We will assume the following notch geometry:

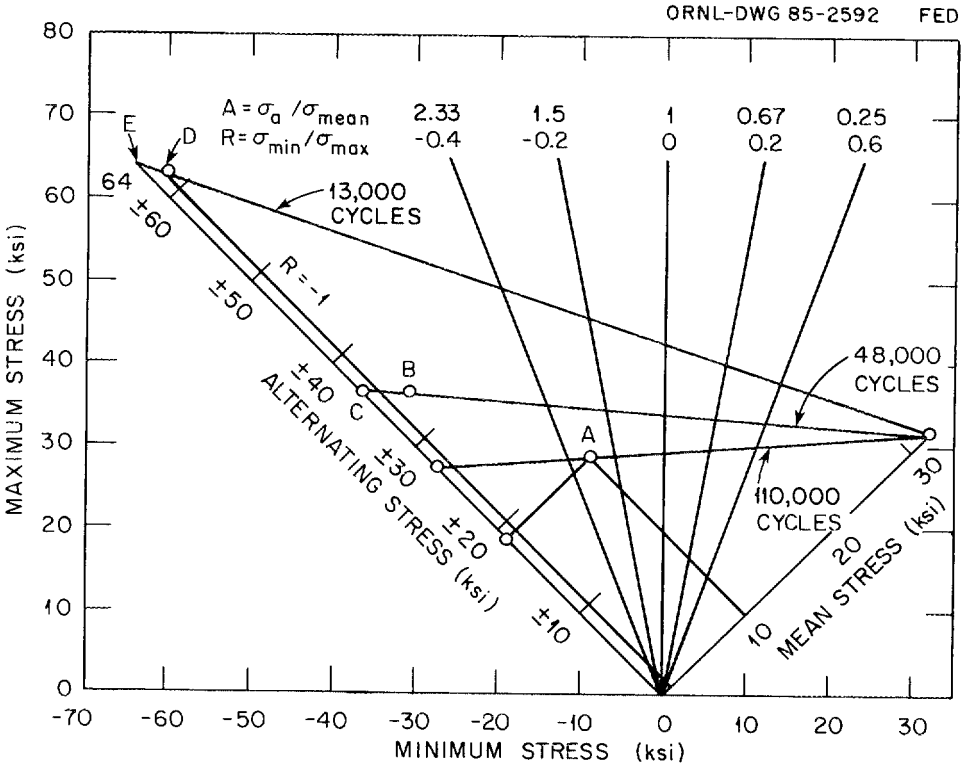

Fig. D.5. Goodman diagram.

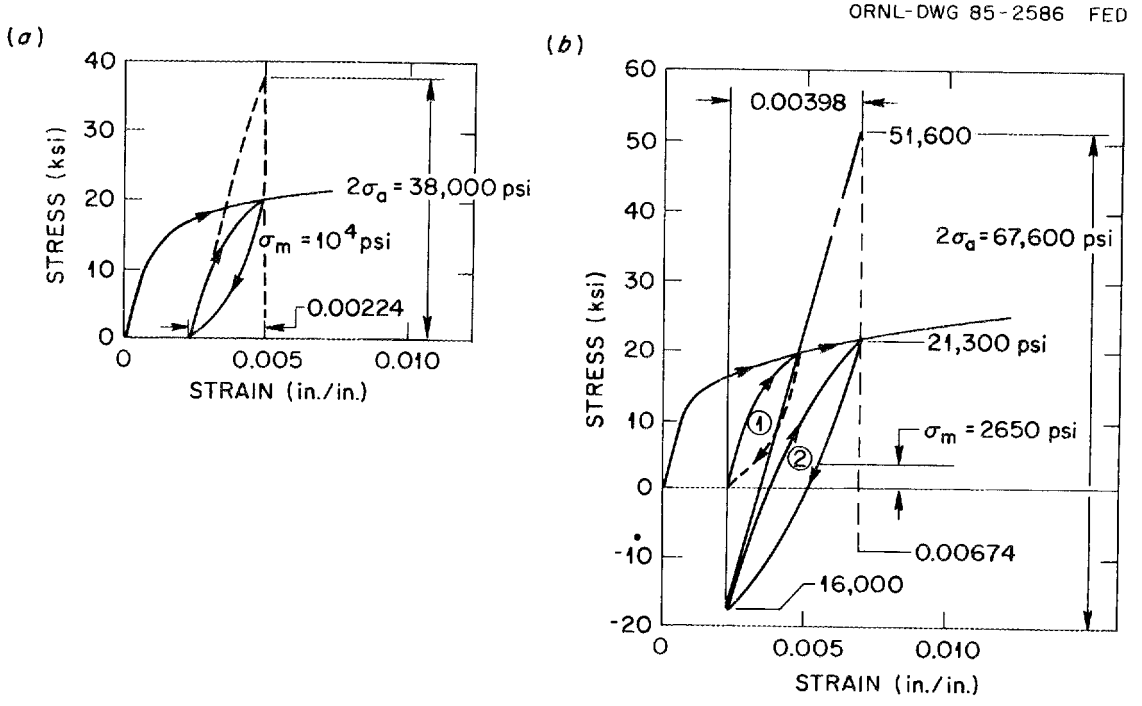

Fig. D.6. Cyclic stress diagrams.

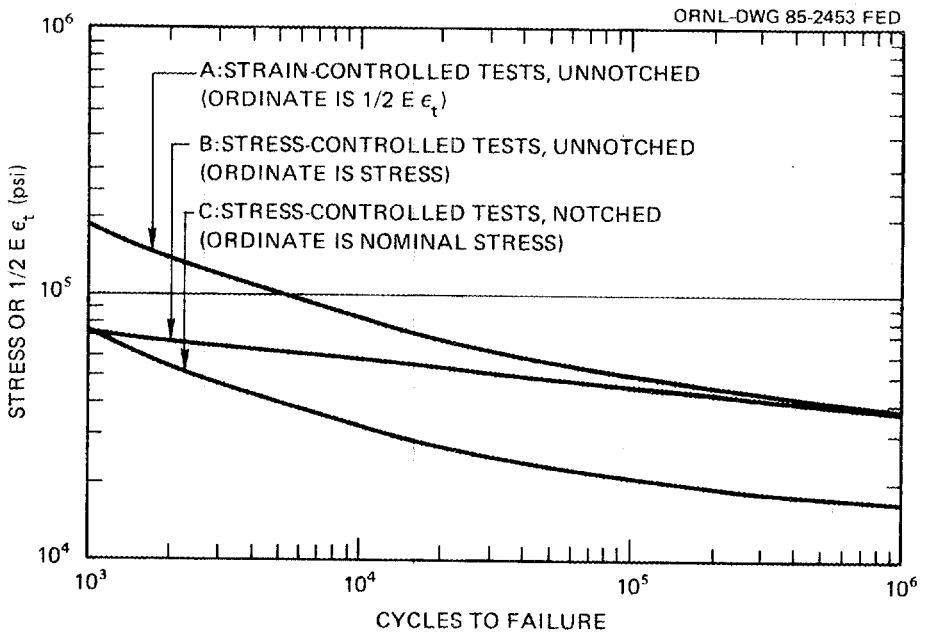

Fig. D.7. Cycles to failure.

$$K_n = 1 + \frac{K_t - 1}{1 + \frac{\pi}{\pi - \omega}} \sqrt{\frac{e}{r}} \ ,$$

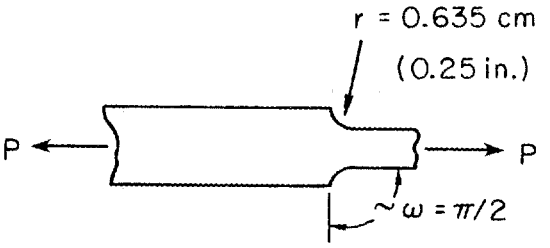

where ω = flank angle of notch, e is the Neuber factor listed in Table D.1, and K_n becomes

$$K_n = 1 + \frac{1}{1 + 2\left(\frac{0.005}{0.25}\right)^{1/2}} = 1.78 \ .$$

The stress σ_A becomes

$$\sigma_A = 1.78\,(19{,}000) = 33{,}800 \text{ psi} \ .$$

The cyclic stress-strain curve takes the shape shown in Fig. D.6(b). The main body of the conductor is being cycled around loop 1 [Fig. D.6(b)], while because of strain concentration, the highest strained point is being cycled around loop 2 to give a strain range of 0.00398. However, the highest strained point is forced into compression by a strain of 0.00398–0.00224 [or 0.00174 in compression, which gives −16,000 psi (see Fig. D.4)].

Thus, we get $\sigma_A = 33{,}800$, $\sigma_m = 2{,}650$, and placing these on the Goodman diagram (Fig. D.5, point B), we get point C (36,700 psi, $R = -1$ line), which gives a life of 48,000 cycles. The design life then is 4800 cycles (48,000 cycles when read on Manson curve in Fig. D.2 for $\sigma_A = 36{,}700$ psi).

Strain concentration of $K_t = 4$

We solve for the strain concentration in the following manner:

$$K_n = 1 + \frac{3}{1 + 2\left(\frac{0.005}{0.25}\right)^{1/2}} = 3.34 \ ,$$

$\sigma_A = 3.34\ (19{,}000) = 63{,}400$ psi.

Figure D.8 illustrates the stress-strain cycle. As shown, $\sigma_A = 63{,}400$ and $\sigma_m = 875$ psi. We put these values on the Goodman diagram to give point E of 64,000 psi on the $R = -1$ line. We look up the life on Fig. D.2 to give 13,000 cycles. The design life is 1300 cycles.

Half-Hard OFHC Copper

We have no low-cycle data for half-hard copper; therefore, we assume a stress-strain curve (after 10^4 cycles) as halfway between annealed OFHC copper and CDA-182.

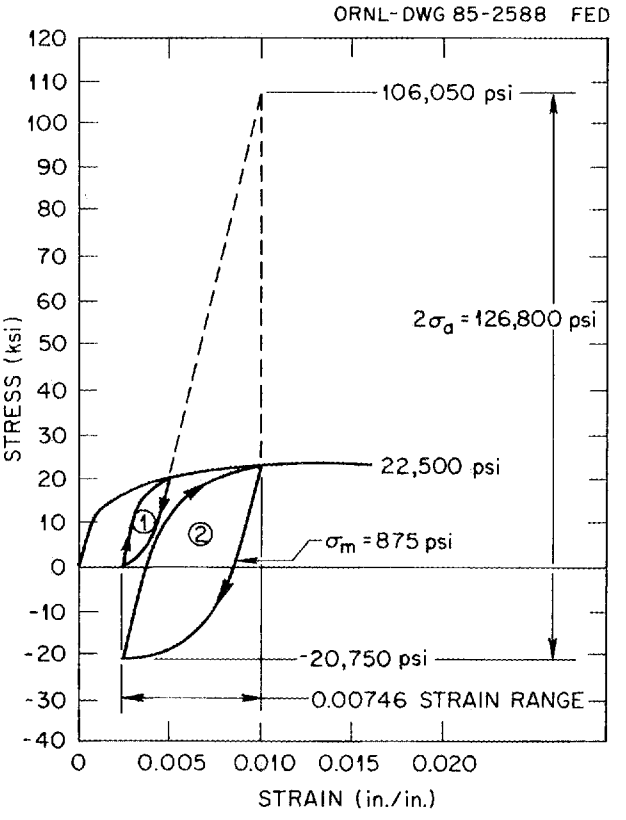

Fig. D.8. Stress-strain cycle.

For an engineering stress of 20,000 psi, we estimate an $R = 0$ stress curve (Fig D.2) for half-hard copper about 20% higher than that for OFHC annealed copper. This gives a life of 350,000 cycles for $\sigma_A = 10{,}000$ psi and an equivalent Manson $R = -1$ stress of 20,000 psi. We put this $R = -1$ stress on a Goodman diagram (curve AC of Fig. D.9). For a mean stress of 10,000 psi, we obtain an elastic stress amplitude of $\sigma_A = 15{,}000$ psi (Fig. D.9). The cyclic stress-strain loop (loop 1) is shown in Fig. D.10. For $K_t = 2$, we obtain

$$K_n = 1 + \frac{1}{1 + 2\left(\frac{0.003}{0.25}\right)^{1/2}} = 1.82 \ ,$$

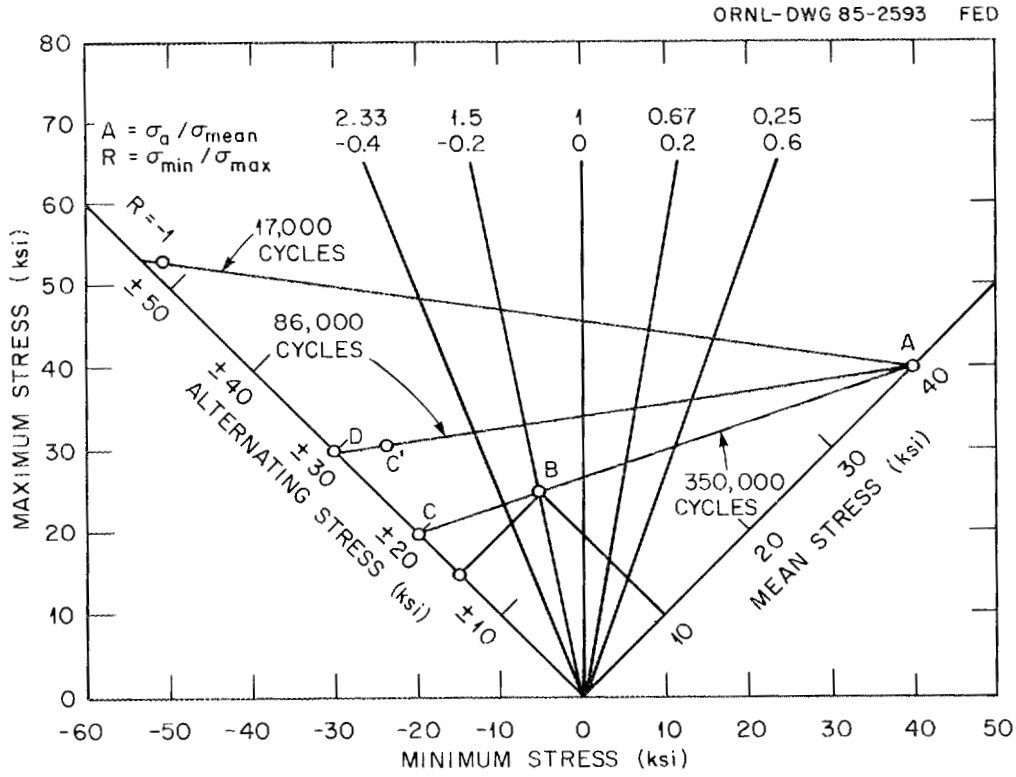

Fig. D.9. Goodman diagram.

σ_A = 1.82(15,000) = 27,300 psi, strain range = $2\sigma_A/E$ = 0.00321, σ_m = 2600 psi. The cyclic stress-strain loop, labeled 2, is shown in Fig. D.10 for these stresses. Loop 1 illustrates the cyclic stress-strain of the overall conductor without strain concentration. We put σ_A and σ_m on the Goodman diagram (Fig. D.9) and determine the line AD. Then we read 30 ksi, which gives 86,000 cycles of life on Fig. D.2. The design life is 8600 cycles.

In the same manner, we determine the design life for K_t = 4, half-hard OFHC copper:

$$K_n = 1 + \frac{3}{1 + 2\left(\frac{0.003}{0.25}\right)^{1/2}} = 3.46 \ ,$$

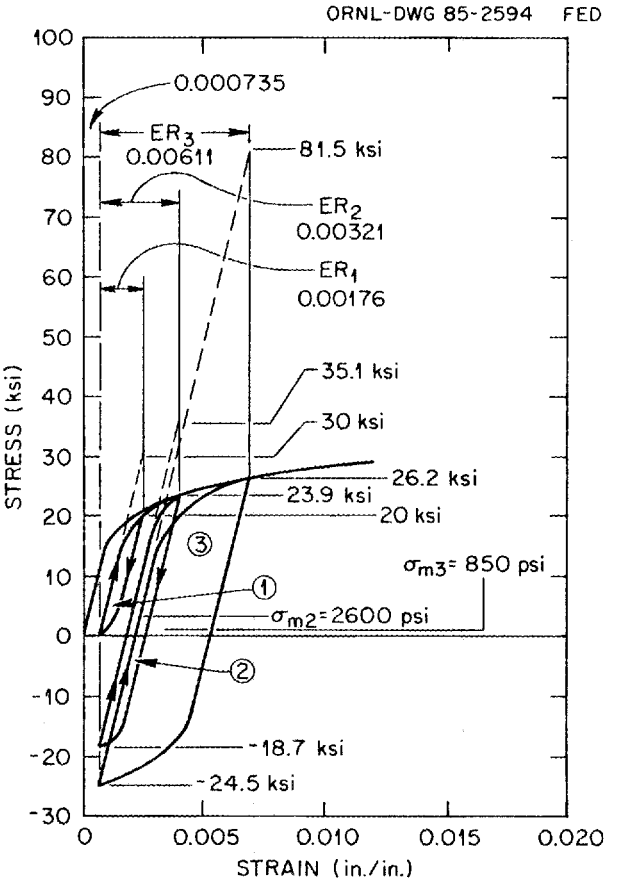

Fig. D.10. Cyclic stress-strain.

with σ_A = 3.46(15,000) = 51,900 psi. We lay out the cyclic stress-strain on loop 3 in Fig. D.10. The mean stress, σ_m, is found to be 850 psi. Then, we lay this out on the Goodman diagram of Fig. D.9, and find the life as before from Fig. D.2, which is 17,000 cycles. This gives a design life of 1700 cycles.

Analysis of CDA-182

We examine CDA-182 from 0 to 20,000 psi. We examine Fig. D.2, for R = 0. The life of CDA-182 would exceed 10^7 cycles. For K_t = 2, we get

$$K_n = 1 + \frac{1}{1 + 2\left(\frac{0.002}{0.25}\right)^{1/2}} = 1.85 ,$$

with $\sigma_A = 10^4 \times (1.85) = 18{,}500$ psi. The $R = 0$ curve for CDA-182 indicates a life greater than 10^7 cycles. For $K_t = 4.0$, we get

$$K_n = 1 + \frac{3}{1 + 2\left(\frac{0.002}{0.25}\right)^{1/2}} = 3.54 ,$$

with $\sigma_A = 10^4(3.54) = 35{,}400$ psi. Figure D.2 indicates low life, but it is not known if yield will take place. The maximum stress will be 70,800 psi. Table D.1 shows that the 0.5% offset yield strength will be 51,000 psi, and CDA is strain-softening (an example of which is shown for steel in Fig. D.11). We need a stress-strain curve for CDA-182 after about 50,000 stress cycles. A good estimate for a strain-softened curve is a stress-strain curve 50% higher than the 10^4-cycle curve for annealed copper (Fig. D.4), as shown in Fig. D.12. Using this curve, it can be seen that considerable yielding would occur in CDA-182 at an elastically calculated stress of 70,800 psi.

We start at zero stress on the stress-strain curve in Fig. D.12. As seen, σ_A is 35,400 psi and σ_m is 2350 psi. We put this on a Goodman diagram (Fig. D.13) and determine a stress of 39,000 psi on the $R = -1$ axis. Figure D.2 indicates a life of 100,000 cycles for this stress. Thus, the design life is 10,000 cycles. We notice that if the static stress-strain curve (shown in Fig. D.12) had been used for CDA-182, the mean stress would have been 9,500 psi instead of 2,350 psi, and the predicted life would have been only 35,000 cycles instead of 100,000. Hence, it is very important to obtain strain-softening effects. Table D.2 is a summary of our findings.

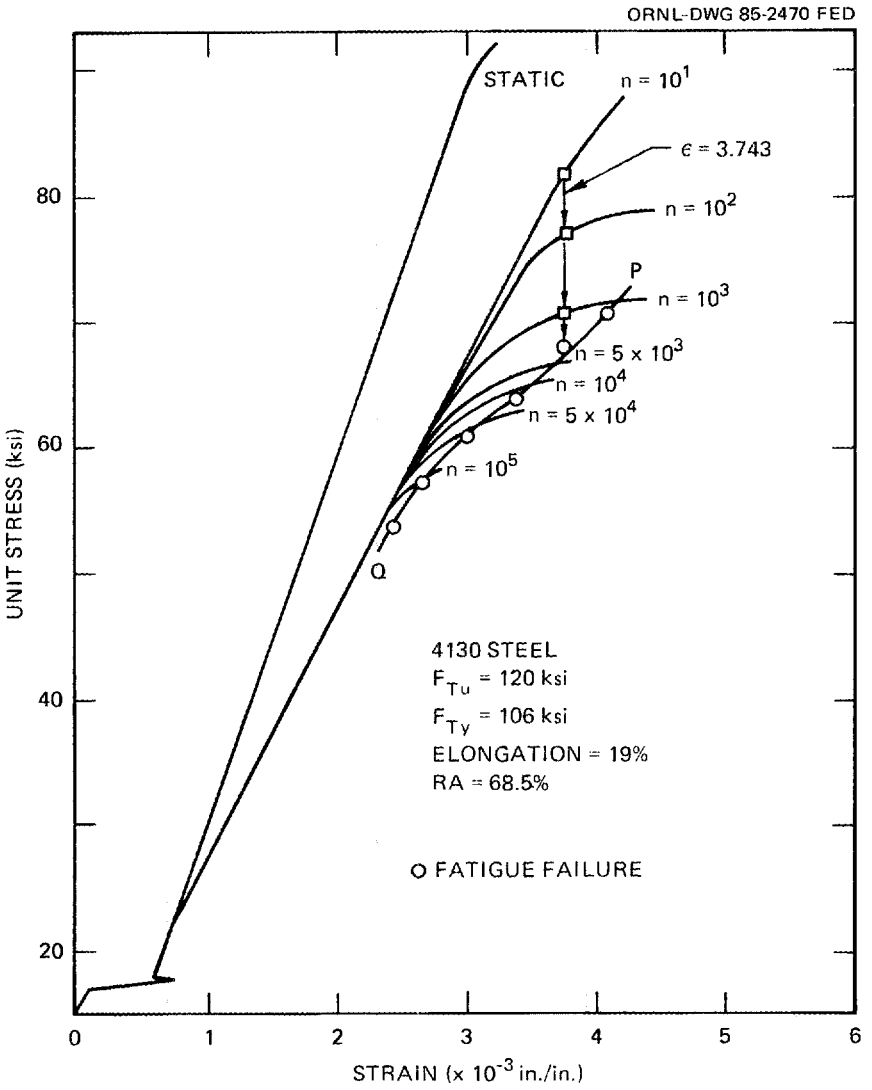

Fig. D.11. Stress-strain curves for steel.

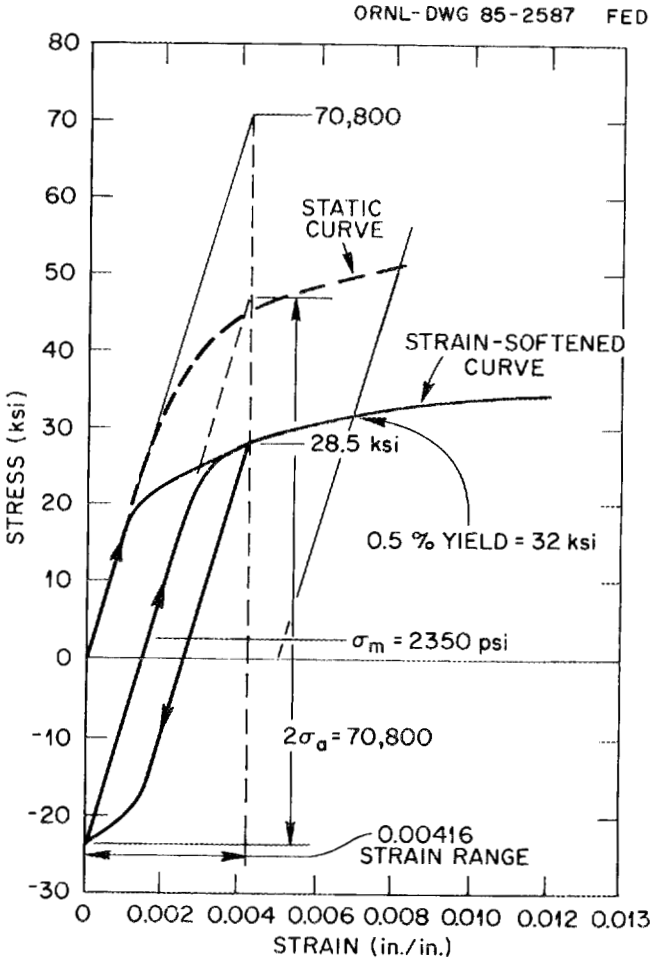

Fig. D.12. Stress-strain curves for annealed copper.

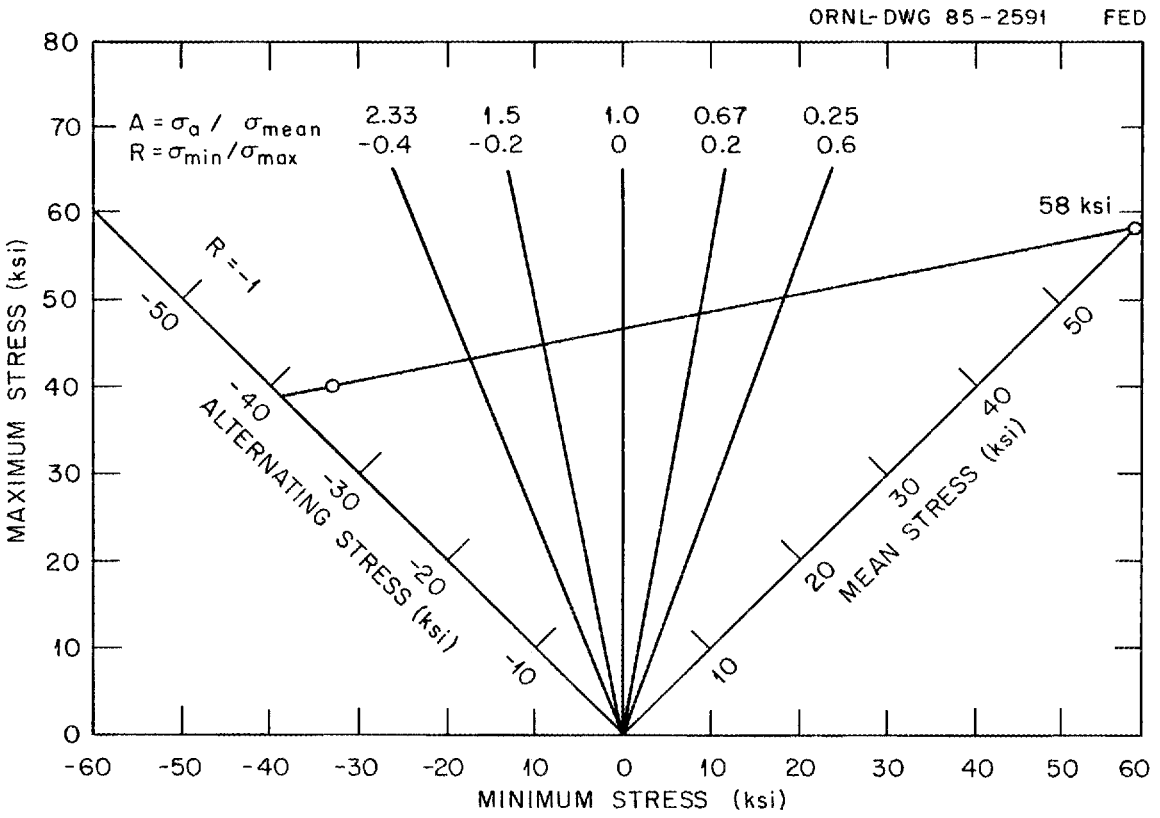

Fig. D.13. Goodman diagram.

Table D.2. Summary of life cycles for copper

Stress condition of conductor	Fatigue design life, cycles		
	Fully annealed OFHC copper	Half-hard OFHC copper	CDA-182 copper alloy
0- to 20,000-psi nominal stress in conductor	11,000	35,000	10^7
0- to 20,000-psi nominal stress in conductor with $K_t = 2$	4,800	8,600	10^7
0- to 20,000-psi nominal stress in conductor with $K_t = 4$	1,300	1,700	10,000

ORNL/TM-9786
Dist. Category UC-20

INTERNAL DISTRIBUTION

1. S. E. Attenberger
2. L. R. Baylor
3. S. K. Borowski
4. R. L. Brown
5. B. A. Carreras
6. L. A. Charlton
7. K. K. Chipley
8. G. R. Dalton
9. R. H. Fowler
10. W. R. Hamilton
11. R. E. Hill
12. S. P. Hirshman
13. J. T. Hogan
14. J. A. Holmes
15. W. A. Houlberg
16. S. S. Kalsi
17–21. E. A. Lazarus
22. V. D. Lee
23. P. S. Litherland
24. D. C. Lousteau
25. J. N. Luton
26. J. A. Mayhall
27. T. J. McManamy
28. G. H. Neilson
29. Y-K. M. Peng
30. J. A. Rome
31. M. J. Saltmarsh
32. D. J. Strickler
33. P. B. Thompson
34. C. C. Tsai
35. W. L. Wright
36. J. Sheffield
37–38. Laboratory Records Department
39. Laboratory Records, ORNL-RC
40. Document Reference Section
41. Central Research Library
42. Fusion Energy Division Library
43–44. Fusion Energy Division Publications Office
45. ORNL Patent Office

EXTERNAL DISTRIBUTION

46. Office of the Assistant Manager for Energy Research and Development, Department of Energy, Oak Ridge Operations Office, P. O. Box E, Oak Ridge, TN 37831
47. J. D. Callen, Department of Nuclear Engineering, University of Wisconsin, Madison, WI 53706
48. R. W. Conn, Department of Chemical, Nuclear, and Thermal Engineering, University of California, Los Angeles, CA 90024
49. S. O. Dean, Director, Fusion Energy Development, Science Applications International Corporation, Gaithersburg, MD 20760
50. H. K. Forsen, Bechtel Group, Inc., Research Engineering, P. O. Box 3965, San Francisco, CA 94205
51. J. R. Gilleland, GA Technologies, Inc., Fusion and Advanced Technology, P.O. Box 81608, San Diego, CA 92138
52. R. W. Gould, Department of Applied Physics, California Institute of Technology, Pasadena, CA 91125
53. R. A. Gross, Plasma Research Library, Columbia University, New York, NY 10027
54. D. M. Meade, Princeton Plasma Physics Laboratory, P.O. Box 451, Princeton, NJ 08544

55. W. M. Stacey, School of Mechanical Engineering, Georgia Institute of Technology, Atlanta, GA 30332
56. D. Steiner, Nuclear Engineering Department, NES Building, Tibbetts Avenue, Rensselaer Polytechnic Institute, Troy, NY 12181
57. R. Varma, Physical Research Laboratory, Navrangpura, Ahmedabad 380009, India
58. Bibliothek, Max-Planck Institut fur Plasmaphysik, D-8046 Garching, Federal Republic of Germany
59. Bibliothek, Institut fur Plasmaphysik, KFA, Postfach 1913, D-5170 Julich, Federal Republic of Germany
60. Bibliotheque, Centre des Recherches en Physique des Plasmas, 21 Avenue des Bains, 1007 Lausanne, Switzerland
61. Bibliotheque, Service du Confinement des Plasmas, CEA, B.P. No. 6, 92 Fontenay-aux-Roses (Seine), France
62. Documentation S.I.G.N., Departement de la Physique du Plasma et de la Fusion Controlee, Centre d'Etudes Nucleaires, B.P. 85, Centre du Tri, 38081 Cedex, Grenoble, France
63. Library, Culham Laboratory, UKAEA, Abingdon, Oxfordshire, OX14 3DB, England
64. Library, FOM-Instituut voor Plasma-Fysica, Rijnhuizen, Edisonbaan 14, 3439 MN Nieuwegein, The Netherlands
65. Library, Institute of Plasma Physics, Nagoya University, Nagoya 464, Japan
66. Library, International Centre for Theoretical Physics, Trieste, Italy
67. Library, Laboratorio Gas Ionizatti, CP 56, I-00044 Frascati, Rome, Italy
68. Library, Plasma Physics Laboratory, Kyoto University, Gokasho, Uji, Kyoto, Japan
69. Plasma Research Laboratory, Australian National University, P.O. Box 4, Canberra, A.C.T. 2000, Australia
70. Thermonuclear Library, Japan Atomic Energy Research Institute, Tokai-mura, Ibaraki Prefecture, Japan
71. G. A. Eliseev, I. V. Kurchatov Institute of Atomic Energy, P. O. Box 3402, 123182 Moscow, U.S.S.R.
72. V. A. Glukhikh, Scientific-Research Institute of Electro-Physical Apparatus, 188631 Leningrad, U.S.S.R.
73. I. Shpigel, Institute of General Physics, U.S.S.R. Academy of Sciences, Ulitsa Vavilova 38, Moscow, U.S.S.R.
74. D. D. Ryutov, Institute of Nuclear Physics, Siberian Branch of the Academy of Sciences of the U.S.S.R., Sovetskaya St. 5, 630090 Novosibirsk, U.S.S.R.
75. V. T. Tolok, Kharkov Physical-Technical Institute, Academical St. 1, 310108 Kharkov, U.S.S.R.
76. Library, Institute of Physics, Academia Sinica, Beijing, Peoples Republic of China
77. R. A. Blanken, Office of Fusion Energy, Office of Energy Research, ER-55, Germantown, U.S. Department of Energy, Washington, DC 20545
78. K. Bol, Princeton Plasma Physics Laboratory, P.O. Box 451, Princeton, NJ 08544
79. R. A. E. Bolton, IREQ Hydro-Quebec Research Institute, 1800 Montee Ste.-Julie, Varennes, P.Q. JOL 2P0, Canada
80. R. L. Freeman, GA Technologies, Inc., P.O. Box 81608, San Diego, CA 92138
81. K. W. Gentle, RLM 11.222, Institute for Fusion Studies, University of Texas, Austin, TX 78712
82. R. J. Goldston, Princeton Plasma Physics Laboratory, P.O. Box 451, Princeton, NJ 08544
83. J. C. Hosea, Princeton Plasma Physics Laboratory, P.O. Box 451, Princeton, NJ 08544
84. S. W. Luke, Office of Fusion Energy, Office of Energy Research, ER-55, Germantown, U.S. Department of Energy, Washington, DC 20545

85. E. Oktay, Office of Fusion Energy, Office of Energy Research, ER-55, Germantown, U.S. Department of Energy, Washington, DC 20545
86. D. Overskei, GA Technologies, Inc., P.O. Box 81608, San Diego, CA 92138
87. R. R. Parker, Plasma Fusion Center, 167 Albany Street, Cambridge, MA 02139
88. W. L. Sadowski, Office of Fusion Energy, Office of Energy Research, ER-55, Germantown, U.S. Department of Energy, Washington, DC 20545
89. J. W. Willis, Office of Fusion Energy, Office of Energy Research, ER-55, Germantown, U.S. Department of Energy, Washington, DC 20545
90. A. P. Navarro, Division de Fusion, Junta de Energia Nuclear, Avenida Complutense 22, Madrid (3), Spain
91. Laboratory for Plasma and Fusion Studies, Department of Nuclear Engineering, Seoul National University, Shinrim-dong, Gwanak-ku, Seoul 151, Korea
92. T. C. Hender, Culham Laboratory, Abingdon, Oxfordshire OX14 3DB, England
93–200. Given distribution according to TIC-4500, Magnetic Fusion Energy (Distribution Category UC-20)